Design and Validation of an Advanced PEMFC Model for Optimal Control of Fuel Cell Powered Hybrid Vehicles

Massimo Sicilia

UNIVERSITY OF SALERNO



DEPARTMENT OF INDUSTRIAL ENGINEERING

Ph.D. Course in Innovative Engineering
Technologies for Industrial Sustainability
XXXVIII Cycle

DESIGN AND VALIDATION OF AN ADVANCED MODEL OF A PEMFC STACK FOR OPTIMAL CONTROL OF FUEL CELL POWERED HYBRID VEHICLES

Supervisor
Prof. Cesare Pianese
Prof. Pierpaolo Polverino

Ph.D. student
Massimo Sicilia

Scientific Referees
Prof. Vincenzo Liso
Prof. Vincenzo Mulone

Ph.D. Course Coordinator
Prof. Diego Barletta

List of publications

Journal articles

1. Maggini, M.; Ubertini, S.; Bartolucci, L.; Cordiner, S.; Mulone, V.; Pianese, C.; Polverino, P.; Sicilia, M.; Facci, A.L. "Design of a Zero-Emission Metal Hydride-based Refueling Station for H2-powered L6e Light-Duty Hybrid Vehicles", *International Journal of Hydrogen Energy* 262: 156691, 2026, DOI: 10.1016/j.ijhydene.2026.156691.

2. Sicilia, M., Cervone, D., Polverino, P., and Pianese, C., "Comparing Different Electrical Architectures for a Parallel PEMFC-Battery Hybrid Electric Lightweight Vehicle," *SAE Int. J. Adv. & Curr. Prac. in Mobility* 8(1):408-427, 2026, DOI: 10.4271/2025-24-0110.

3. Sicilia, M.; Cervone, D.; Polverino, P.; Pianese, C. Adaptive Equivalent Consumption Minimization Strategies for Plug-In Hybrid Electric Vehicles: A Review. *Energies* **2025**, *18*, 5475, DOI: 10.3390/en18205475.

4. Sicilia, M.; Cervone, D.; Polverino, P.; Pianese, C. Advancements on Lumped Modelling of Membrane Water Content for Real-Time Prognostics and Control of PEMFC. *Energies* **2024**, *17*, 4841, DOI: 10.3390/en17194841.

5. Cervone, D., Sicilia, M., Romano, M., Polverino, P. et al., "Modelling of a Hybrid Quadricycle (L6e vehicle) Equipped with Hydrogen Fueled ICE Range Extender and Performance Analysis on Stochastic Drive Cycles Generated from RDE Profile," *SAE Int. J. Adv. & Curr. Prac. in Mobility* 6(4):2087-2101, 2024, DOI: 10.4271/2023-24-0149.

Proceedings

1. Cervone, D., Sicilia, M., Polverino, P., and Pianese, C., "Effects of the Battery Pack Temperature on the Energy Management Strategy and Fuel Consumption of a Series Hybrid Quadricycle," SAE Technical Paper 2025-24-0101, 2025, DOI: 10.4271/2025-24-0101.

2. Sicilia, M., Cervone, D., Polverino, P., and Pianese, C., "Model-Based Algorithm for Water Management Diagnosis and Control of PEMFC Systems for Motive Applications," SAE Technical Paper 2024-37-0004, 2024, DOI: 10.4271/2024-37-0004.

3. Cervone, D., Sicilia, M., Pandolfi, A., Polverino, P. et al., "Machine Learning Based Design of Optimal Energy Management Strategy for Hydrogen-Fueled Hybrid Vehicle Powertrain," SAE Technical Paper 2024-24-0001, 2024, DOI: 10.4271/2024-24-0001.

Oral contributions

1. Sicilia, M.; Cervone, D.; Polverino, P.; Pianese, C. "Experimental Validation of a PEMFC Lumped Dynamic Model for On-board, Diagnostic, Prognostic, and Control Applications", European Fuel Cells and Hydrogen, Piero Lunghi Conference 2025 – EFCH2 2025, Capri (NA), Italy, 2025.

2. Sicilia, M.; Cervone, D.; Polverino, P.; Pianese, C. "Comparing Different Electrical Architectures for a Parallel PEMFC-Battery Hybrid Electric Lightweight Vehicle", 17th International Conference on Engines & Vehicles for Sustainable Transport – ICE2025, Capri (NA), Italy, 2025.

3. Sicilia, M.; Cervone, D.; Polverino, P.; Pianese, C. "Model-Based Algorithm for Water Management Diagnosis and Control of PEMFC Systems for Motive Applications", CO2 Reduction for Transportation Systems, Torino (TO), Italy, 2024.

Other

1. Sicilia, M.; Cervone, D.; Polverino, P.; Pianese, C. "Experimental validation of a PEMFC lumped dynamic model for on-board, diagnostic, prognostic and control applications", in: European Fuel Cells and Hydrogen Piero Lunghi Conference, Capri (NA), Italy, 2025, pp. 271-273. (extended abstract, accepted for publication on International Journal of Hydrogen Energy)

2. Maggini, M.; Ubertini, S.; Bartolucci, L.; Cordiner, S.; Mulone, V.; Pianese, C.; Polverino, P.; Sicilia, M.; Facci, A.L. "Design of a Zero-Emission Metal Hydride-based Refueling Station for H2-powered L6e Light-Duty Hybrid Vehicles", in: European Fuel Cells and Hydrogen Piero Lunghi Conference, Capri (NA), Italy, 2025, pp. 152-154 (extended abstract).

Table of Contents

Table of contents **I**

List of figures **V**

List of tables **XI**

Sommario **XIII**

Abstract **XV**

Introduction **XVII**
Environmental challenges of the transport sector XVII
Motivations and objectives XXI
Contributions XXII

I Hydrogen for sustainable mobility **1**
I.1 Advantages and issues of hydrogen utilisation 1
I.1.1 Physical properties 2
I.1.2 Production technologies 3
I.2 Fuel cells technology 4
I.2.1 Classification of fuel cells 6
I.2.2 Proton Exchange Membrane Fuel Cells 7
I.3 Hybrid vehicles generalities 12
I.3.1 Classification of hybrid vehicles 13
I.3.2 Control strategies overview 16
I.4 Conclusions 22

II Membrane advanced lumped model for dynamic simulation **23**
II.1 Description of the problem 23

II.1.1 Swelling effect 24
II.1.2 Electro-osmotic drag 24
II.1.3 Convection 25
II.1.4 Diffusion 26
II.1.5 The complete well-posed PDE problem 27
II.2 Numerical resolution of the PDE problem 28
II.2.1 Steady-state solution 28
II.2.2 Transient solution 34
II.3 Analytical resolution of the linearised PDE problem 36
II.3.1 Main assumptions and problem normalisation 36
II.3.2 Steady-state solution 38
II.3.3 Transient solution 41
II.3.4 Comparison with the numerical solution 46
II.4 Application of the integral method 48
II.4.1 Integral solution identification 48
II.4.2 Validation of the proposed integral solution 52
II.4.3 Net water molar fluxes integration 56
II.4.4 Integral solution implementation algorithm 58
II.5 Conclusions 59

III PEMFC lumped model for on-board monitoring and control purposes 61
III.1 Model description and main assumptions 61
III.1.1 Mass balances 63
III.1.2 Gas mixture properties 67
III.1.3 Supply and discharge manifold flows 69
III.1.4 Transport mechanisms 70
III.1.5 Water evaporation and condensation modelling 73
III.1.6 Polarisation curve and electrical performance 74
III.1.7 Dynamic energy balance 77
III.2 Lumped dynamic model for polymeric membrane 78
III.2.1 Characterisation of operative conditions 78
III.2.2 Water membrane content identification 79
III.2.3 Net water flows exchange 80
III.3 Experimental validation and dynamic testing 81
III.3.1 Experimental data acquisition 81
III.3.2 Steady-state validation 88
III.3.3 Dynamic validation and analyses 92
III.3.4 Computational performance 96
III.4 Conclusions 96

IV Hydrogen-fuelled hybrid vehicle modelling and simulation 97

IV.1 Electrical vehicle modelling approach 97
IV.1.1 Road load identification 98
IV.1.2 In-wheel motor modelling approach 101
IV.1.3 DC/DC converter behavioural model 102
IV.1.4 Battery quasi-static model 104
IV.1.5 EV range assessment and validation 106
IV.2 Hydrogen-fuelled range extender hybridisation 108
IV.2.1 Tank sizing 110
IV.2.2 PEMFC stack modelling 111
IV.2.3 Control strategies description 115
IV.3 Simulation results and discussion 118
IV.3.1 T3 architecture 118
IV.3.2 T3-bis architecture 120
IV.3.3 T4 architecture 123
IV.3.4 Macro parameters comparison 126
IV.4 Conclusions 129

Conclusions **131**

References **133**

List of Acronyms **141**

List of Symbols **143**

Acknowledgements **151**

List of Figures

1 Global average temperature anomaly compared to 1861-1890 pre-industrial period with 95% confidence interval, adapted from ref. (Ritchie, Rosado, and Roser 2023). XVIII
2 Annual CO_2 emissions from 1850 to 2023 in billion tons shared between countries, international shipping, and aviation, adapted from ref. (Ritchie, Rosado, and Roser 2023). XVIII
3 Total greenhouse gas emissions expressed as equivalent CO_2 tons divided by sectors, from 1990 to 2021, adapted from ref. (Ritchie, Rosado, and Roser 2020). XIX
4 CO_2 emissions due to transport sector in 2018 divided by vehicle type, adapted from ref. (Ritchie 2020). XX

I.1 Reversible open circuit voltage produced by hydrogen-oxygen ROR. 5
I.2 Comparison between fuel cell ideal efficiency and Carnot theorem with 20°C heat sink temperature. 6
I.3 PEMFC single cell schematic, with electrodes, membrane, and gases flows highlighted. 8
I.4 Schematic representation of PEM electrolyte structure and main protons transport mechanisms. 10
I.5 Fuel cells hybrid vehicle electrical layouts, adapted from ref. (Sorlei et al. 2021): (a) T1; (b) T2; (c) T3; (d) T4. 15
I.6 Multilevel control architecture schematization for HEVs. . . . 17

II.1 Dimensionless Γ function for diffusion coefficient characterisation with respect to water membrane content λ. 27
II.2 Grid stencil considered for steady-state numerical resolution. . 28
II.3 Grid convergence analysis results: average water membrane content (left axis, blue); computational time (right axis, red). . 31

II.4 Water membrane content steady state solution with respect to normalised dry thickness, with Table II.1 as dataset. 31
II.5 Water molar fluxes steady state solution with respect to normalised dry thickness, with Table II.1 as dataset. 32
II.6 Membrane average conductivity as function of boundary conditions, with Table II.2 as dataset. 33
II.7 Membrane average net water molar flux as function of boundary conditions, with Table II.2 as dataset. 33
II.8 Water membrane content transient solution with respect to normalised dry thickness, with Table II.1 as dataset. 35
II.9 Average water membrane content transient solution evolving in time, with Table II.1 as dataset. 35
II.10 Average water molar fluxes transient solution evolving in time, with Table II.1 as dataset. 36
II.11 Normalised steady-state water membrane content calculated from linearised water problem, as function of Peclet number. . 38
II.12 Normalised average steady-state water membrane content calculated from linearised water problem, as function of Peclet number. 39
II.13 Comparison between numerical (solid line) and analytical (dashed line) steady state solutions, with Table II.1 as dataset. 40
II.14 Comparison between average numerical (solid line) and analytical (dashed line) steady state solutions varying Peclet number, with Table II.1 as dataset. 41
II.15 Representation of the first five spatial eigenfunctions, together with envelope curves, for $Pe = 5$. 42
II.16 Representation of time constants for different modes as function of Peclet number. 42
II.17 Representation of integration constants for different modes as function of Peclet number, considering a pure diffusive initial condition. 43
II.18 Normalised unsteady water membrane content calculated from linearised water problem, as function of Peclet number, space, and time. 44
II.19 Normalised water membrane content calculated from linearised water problem, as function of Peclet number, space, and time. . 45
II.20 Normalised average water membrane content calculated from linearised water problem, as function of Peclet number. 46
II.21 Comparison between numerical (solid line) and analytical (dashed line) solutions, with Table II.1. 47

II.22 Comparison between average numerical (solid line) and analytical (dashed line) solutions over time, with Table II.1 as dataset. 47
II.23 Dimensionless characteristic time constant as function of Peclet number. 50
II.24 Comparison between analytical (solid lines) and integral (dashed lines) solutions as function of Peclet number, space, and time. 51
II.25 Comparison between analytical (solid lines) and integral (dashed lines) average solutions as function of time, varying Peclet. . . 51
II.26 Error map between average analytical and integral solutions, as function of Peclet number and dimensionless time. 52
II.27 Comparison between numeric (solid lines), analytic (dashed lines), and integral (dotted lines) water membrane content distributions at different time instants, with Table II.1 as dataset. . 53
II.28 Comparison between average numeric (solid lines), analytic (dashed lines), and integral (dotted lines) water membrane content distributions, with Table II.1 as dataset. 53
II.29 Mean percent error between average numerical and integral transient solutions as function of current density and temperature with negative pressure gradient, with Table II.3 as dataset. 55
II.30 Mean percent error between average numerical and integral transient solutions as function of current density and temperature with positive pressure gradient, with Table II.3 as dataset. 55
II.31 Mean percent error between average numerical and integral transient solutions as function of boundary conditions, with Table II.3 as dataset. 56

III.1 PEMFC model schematic, with main volumes and gas flows . 62
III.2 H-100 PEM fuel cell stack, by Horizon Technologies. 82
III.3 H-100 voltage-current curve (blue line) and power-current curve (red line), adapted from ref. (Horizon Technologies 2023a). . . 83
III.4 H-100 single cell polarization curve. 83
III.5 PEMFC test bench at the Energy and Propulsion Systems Laboratory, University of Salerno. 84
III.6 Schematic of the PEMFC test rig facility. 85
III.7 Actual controlled current profile over time. 85
III.8 Comparison between raw (blue line) and filtered (red line) experimental data, with exponential filters. 86
III.9 Comparison between raw (blue line) and reconstructed (red line) measured temperature, with model-based filter. 87

III.10 Collection of steady-state data after filtering and integral average processes as function of current, acquired at the test bench. 89
III.11 Model steady-state validation with respect to experimental data. 90
III.12 Single cell voltage analysis for every term of polarization curve: total (blue); Nernst potential (red); activation losses (yellow); Ohmic losses (purple); concentration losses (green); offset losses (cyan). 90
III.13 Water content values varying current for membrane (black, circle), anode (red, square), and cathode (blue, triangle). . . . 91
III.14 Water saturation values varying current for anode (left) and cathode (right) in the different sub-volumes: GFC (blue); GDL-a (red); GDL-b (yellow); GDL-c (purple); CL (green). . 91
III.15 Voltage dynamic validation with respect to experimental data. 92
III.16 Temperature dynamic validation with respect to experimental data. 93
III.17 Single cell dynamic voltage analysis for every term of polarization curve: total (blue); Nernst potential (red); activation losses (yellow); Ohmic losses (purple); concentration losses (green); offset losses (cyan). 94
III.18 Water content values in time for membrane (black), anode (red), and cathode (blue). 95
III.19 Water saturation profiles in time for anode (left) and cathode (right) in the different sub-volumes: GFC (blue); GDL-a (red); GDL-b (yellow); GDL-c (purple); CL (green). 95

IV.1 Tritone vehicle, by OPV Mobility. 98
IV.2 Electrical powertrain scheme, with main components highlighted. 99
IV.3 Model schematisation of the original pure EV vehicle. 99
IV.4 Longitudinal vehicle dynamics model scheme, with main forces highlighted. 99
IV.5 Road load power requirement as function of speed, from -10% to 10% road slope. 100
IV.6 EMG efficiency contour map in both traction and generation quadrants. 102
IV.7 Equivalent circuit model of the DC/DC converter. 103
IV.8 DC/DC converter efficiency as function of transmitted power in discharging mode (solid line) and charging mode (dashed line), at 48 V. 104
IV.9 Battery cell equivalent circuital model scheme. 105

IV.10 Battery stack equivalent open-circuit voltage (left) and internal resistance (right) as function of battery SoC (Cervone, Sicilia, Romano, et al. 2023). 105
IV.11 Battery efficiency contour map as function of battery SoC and C-rate. 106
IV.12 WMTC-L6 standard drive cycle for model range assessment. . 107
IV.13 Pure EV configuration model range validation, on WMTC-L6 drive cycle. 107
IV.14 T3 architecture for the proposed electric vehicle hydrogen hybridisation. 108
IV.15 T3-bis architecture for the proposed electric vehicle hydrogen hybridisation. 109
IV.16 T4 architecture for the proposed electric vehicle hydrogen hybridisation. 110
IV.17 H-3000 modelled fuel consumption with respect to electrical power. 113
IV.18 H-3000 modelled efficiency, referred to PEMFC only (dashed line) and at system level (solid line), with respect to stack current. 114
IV.19 DC/DC converter efficiency as function of transmitted power in discharging mode (solid line) and charging mode (dashed line), at 48 V. 114
IV.20 Example of ON-OFF Rule-Based control strategy application on battery SoC. 116
IV.21 Simulation results for battery State-of-Charge over mileage, T3 architecture. 118
IV.22 Battery efficiency contour map (left) and efficiency distributions (right), with working points highlighted with respect to operating mode: hybrid (blue); charging (red); regenerative braking (green). T3 architecture. 119
IV.23 PEMFC stack efficiency profile (left) and efficiency distributions (right), with working points highlighted with respect to operating mode: hybrid (blue); charging (red). T3 architecture. 119
IV.24 Energy share results during simulation, T3 architecture: hydrogen chemical energy (blue); battery residual energy (red); conversion losses (yellow); auxiliary absorption (purple); load (green). 120
IV.25 Simulation results for battery State-of-Charge over mileage, T3-bis architecture. 121

IV.26 Battery efficiency contour map (left) and efficiency distributions (right), with working points highlighted with respect to operating mode: hybrid (blue); charging (red); regenerative braking (green). T3-bis architecture. 121
IV.27 PEMFC stack efficiency profile (left) and efficiency distributions (right), with working points highlighted with respect to operating mode: hybrid (blue); charging (red). T3-bis architecture. 122
IV.28 Energy share results during simulation, T3-bis architecture: hydrogen chemical energy (blue); battery residual energy (red); conversion losses (yellow); auxiliary absorption (purple); load (green). 122
IV.29 Simulation results for battery State-of-Charge over mileage, T4 architecture: RB (blue); PI-RB (red); PMP (yellow); A-ECMS (purple). 123
IV.30 Battery efficiency contour map (left) and efficiency distributions (right), with working points highlighted with respect to control strategies and operating mode: hybrid (blue); charging (red); regenerative braking (green). T4 architecture. 124
IV.31 PEMFC stack efficiency profile (left) and efficiency distributions (right), with working points highlighted with respect to control strategies operating mode: hybrid (blue); charging (red). T4 architecture. 125
IV.32 Energy share results during simulation for every control strategy, T4 architecture: hydrogen chemical energy (blue); battery residual energy (red); conversion losses (yellow); auxiliary absorption (purple); load (green). 125
IV.33 Average fuel consumption results for every simulation. 126
IV.34 Average equivalent fuel consumption results for every simulation. 127
IV.35 Average Powertrain Efficiency Index results for every simulation. 128
IV.36 Instantaneous PEI for every architecture (solid lines) and every control strategies (different markers) as function of power split. 129

List of Tables

1 Regulated pollutant emissions for light-duty passenger vehicles, EURO-6, tested on World Motorcycle Test Cycle (WMTC) drive cycle, adapted from ref. (Mulholland et al. 2022). XX

I.1 Hydrogen physical properties, adapted from ref. (Keçebaş and Kayfeci 2019). 2
I.2 Hydrogen physical properties, adapted from ref. (Keçebaş and Kayfeci 2019). 2
I.3 Classification of widely used fuel cell technologies, based on electrolyte material, adapted from ref. (Sharaf and Orhan 2014). 7
I.4 Functional classification of hybrid vehicles based on degree of hybridization. 14
I.5 Functional classification of A-ECMS for HEVs. 21

II.1 Operative conditions and membrane physical features dataset for the steady-state solution numerical convergence analysis . . 30
II.2 Operative conditions and membrane physical features dataset for the steady-state solution numerical literature validation. . . 32
II.3 Membrane physical features and operative conditions dataset for the integral solution parametric analysis. 54

III.1 Model comparison with literature works. 63
III.2 H-100 datasheet, by Horizon Technologies. 83
III.3 Model steady-state validation statistical analysis. 88
III.4 Voltage model dynamic validation statistical analysis. 93
III.5 Temperature model dynamic validation statistical analysis. . . 94

IV.1 Tritone data sheet, adapted from manufacturer data (OPV Smart Urban Mobility 2023). 98

IV.2 H-3000 PEMFC stack data sheet, adapted from manufacturer data (Horizon Technologies 2023b). 111
IV.3 Configuration matrix of the control strategies with respect to powertrain layout. 115

Sommario

L'urgente necessità di ridurre le emissioni di gas serra e mitigare la dipendenza dai combustibili fossili ha accelerato la ricerca nel campo della mobilità sostenibile. I veicoli elettrici a batteria (BEV) stanno guadagnando quote di mercato, ma la loro adozione è ancora limitata dalla disponibilità di infrastrutture, vincoli di peso e limitata autonomia. Per tale motivo, la transizione verso una totale elettrificazione dei trasporti è ancora lontana, e l'uso di veicoli ibridi è attualmente considerato un'alternativa percorribile per il perseguimento dell'obiettivo di decarbonizzazione del settore. In alternativa ai soluzioni convenzionali, l'idrogeno è emerso come vettore energetico versatile, grazie alla possibilità di produrre direttamente energia elettrica sfruttando celle a combustibile a membrana a scambio protonico (PEMFC), impiegate sia come sistema primario di propulsione che come range extender. Nel contesto illustrato, questa tesi di dottorato propone un approccio di modellizzazione integrato per sviluppare architetture ibride alimentate a idrogeno, combinando la modellizzazione ad alta fedeltà dei componenti con la simulazione del veicolo a livello di sistema per ottenere un'elevata efficienza e un'autonomia estesa.

L'attività di ricerca presentata segue una metodologia multiscala, partendo dallo sviluppo di un modello dinamico a parametri concentrati di uno stack PEMFC per applicazioni in tempo reale. Il modello considera il trasporto di gas, le reazioni elettrochimiche e la gestione dell'acqua all'interno della cella, bilanciando la semplicità computazionale con l'accuratezza fisica. È stato sviluppato e integrato un sottomodello analitico dedicato al comportamento della membrana, derivato dall'equazione di bilancio dell'acqua all'interno della membrana: questa formulazione consente di modellare i fenomeni fisici essenziali che avvengono all'interno della membrana sia in condizioni stazionarie che transitorie, permettendo di determinare rapidamente la resistenza ohmica della membrana. La gestione dell'acqua e del calore è rappresentata con modelli specifici, bilanciando precisione ed accuratezza. Il modello è stato validato con dati sperimentali provenienti da uno stack commerciale a catodo aperto, dimostrando una buona accuratezza sia in condizioni stazionarie che transitorie, con errori medi inferiori al 5% e un tempo di calcolo ridotto, più di 50 volte più veloce del tempo reale. Il modello è adatto per l'integrazione in sistemi di

monitoraggio e controllo a bordo del veicolo, consentendo il rilevamento dei guasti e l'estensione della durata di vita degli stack PEMFC.

Proseguendo lungo la scala fisica fenomenologica, il quadro modellistico è esteso a livello di sistema per studiare l'integrazione dello stack PEMFC in un'architettura ibrida. Il caso studio si focalizza su un quadriciclo leggero ibridizzato con una PEMFC che lavora come range extender. Questa configurazione è progettata, modellata dal punto di vista dei flussi energetici e infine simulata durante un ciclo di omologazione standard per la determinata classe di veicolo, in conformità con le normative vigenti. Trattandosi di powertrain ibrido, sono state implementate diverse strategie di gestione dell'energia che vanno dal controllo euristico, basato su regole empiriche, ad algoritmi di controllo ottimo, come il principio minimo di Pontryagin (Pontryagin's Minimum Principle – PMP) e la strategia di minimizzazione del consumo equivalente (Equivalent Consumption Minimisation Strategy – ECMS). I risultati della simulazione evidenziano che range extender basati su PEMFC sono in grado di estendere in modo significativo l'autonomia del veicolo, in particolare quando vengono applicate strategie di controllo ottimali che migliorano il consumo di combustibile fino ad un massimo del 7%.

L'integrazione di approcci multi-scala, passando da attività di model-based design al model-based control, rappresenta il contributo innovativo di questo lavoro allo stato dell'arte, fornendo un set completo di strumenti per lo sviluppo di soluzioni efficienti e affidabili basate sull'idrogeno nel settore dei trasporti. Il modello PEMFC proposto può essere implementato come digital twin del sistema reale per la diagnosi a bordo, mentre la sua integrazione nel modello di veicolo ibrido fornisce una base di simulazione affidabile per l'ottimizzazione delle strategie controllo di alto livello. Nel loro insieme, queste attività supportano lo sviluppo di soluzioni basate sull'idrogeno efficienti e tecnologicamente vantaggiose, aprendo la strada a future ricerche sulla dinamica dei sottosistemi e sulle strategie correttive per migliorare l'affidabilità nelle applicazioni reali.

Abstract

The urgent need to reduce greenhouse gas emissions and mitigate dependence on fossil fuels has accelerated research into sustainable mobility. Battery electric vehicles (BEVs) are gaining market share, but their adoption is still limited by infrastructure availability and mileage constraints. Hence, the transition towards full electrification is still far, and deployment of hybrid powertrains is currently a worldwide recognise alternative towards the decarbonisation of mobility sector. Alternative to conventional solutions, hydrogen has emerged as a versatile energy carrier, particularly used in electrochemical conversion systems such as Proton Exchange Membrane Fuel Cells (PEMFCs), used either as first mover or range extender within hybrid architectures. In such framework, this doctoral thesis proposes an integrated modelling approach to develop hydrogen-fuelled hybrid architectures, combining high-fidelity component modelling with system-level vehicle simulation to achieve high efficiency and extended range.

The research follows a multi-scale methodology, starting from the development of a dynamic lumped model of a PEMFC stack designed for real-time applications. The model accounts for gas transport, electrochemical reactions, and water management within the cell, balancing computational simplicity with physical accuracy. A dedicated analytical sub-model for membrane behaviour, derived from the membrane physical water balance, is developed and integrated: this formulation allows to capture the essential physics happening inside the membrane both in steady-state and transient conditions, allowing to determine the membrane ohmic resistance. The water and thermal managements are accounted with specific accurate models with balanced precision. The model is validated against experimental data from a commercial open-cathode stack, demonstrating good agreement in both steady-state and transient conditions, with average errors below 5%, and low computing time, more than 50 times faster than real time. The model is suitable for integration into on-board monitoring and control systems applications, enabling fault detection and lifetime extension of PEMFC stacks.

Leveraging component-level accuracy, the modelling framework is scaled up to system level to investigate the integration of PEMFC stack into a hydrogen-

fuelled hybrid powertrain. The case study addresses a lightweight hybrid electric vehicle equipped with a hydrogen-fuelled PEMFC stack operating as range extender. This configuration is modelled and tested under standard homologation cycle, following current regulations. Several energy management strategies are implemented, ranging from heuristic rule-based control to optimal algorithms, such as Pontryagin's Minimum Principle (PMP) and Equivalent Consumption Minimisation Strategy (ECMS). Simulation results highlight that PEMFC-based range extenders are feasible to significantly improve vehicle range, particularly when optimal control strategies are applied, also improving fuel consumption up to 7%.

The integration of these models designed at different scales advances the state of knowledge by providing a comprehensive toolset for the development of efficient and reliable hydrogen-based solutions. The PEMFC model acts as a digital twin for on-board diagnosis, while its integration into the hybrid vehicle model provides a reliable simulation ground for high-level optimal control design. Collectively, these activities support the development of efficient and technologically advantageous hydrogen-based solutions, paving the way for future research on system dynamics and corrective strategies to improve reliability in real-world applications.

Introduction

In the field of energy sustainable production in the motive sector, the recent regulations and policy directives pose a great challenge for the reduction of pollutant emissions. The Proton Exchange Membrane Fuel Cell (PEMFC) technology is taking a major contribution role, thanks to research development and public investment on hydrogen technologies: the use of hydrogen as energy carrier is a promising solution to fulfil the latest policy makers pollutant regulations, fuelling hybrid electric vehicles with green hydrogen leading to zero well-to-wheel emissions. In this chapter, the environmental contextualisation of the transport sector is provided, to properly defined the framework and objectives of this doctoral dissertation.

Environmental challenges of the transport sector

During the last years, climate change effects are becoming more evident, frequent, and aggressive: there is a general increase in the average energy of the atmosphere, which is not able to deliver out the excess amount, with more frequent and stronger extreme weather events. The main evidence of climate change is the increasing global average temperature anomaly, shown in Figure 1: the temperature anomaly is referred to the pre-industrial period from 1861 to 1890 with red solid line, while the 95% confidence lower and upper boundaries are shown with black dashed and dotted lines, respectively.

Analysing the average global temperature, two main distinct trends can be identified. The first trend is a random year variation with zero average, from 1850 to 1925, in which the temperature variation can be associated to environmental changes. The second, and most evident, trend is shown from 1925-1950 until today: the temperature anomaly increases year after year, reaching the last value of around 1.5°C. The temperature rose quickly in only 40 years.

Scientific boards agree on the causal relation between average temperature increase and CO_2 due to the Greenhouse Gas (GHG) effect: the stationary temperature is correlated to the atmosphere absorption of the solar heat radiation

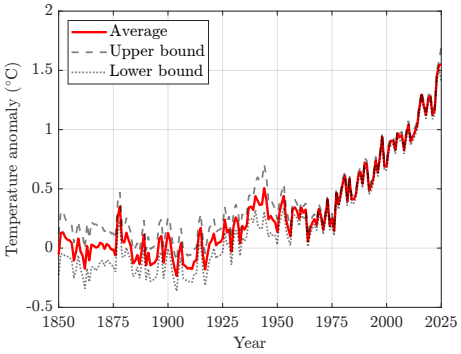


Figure 1 *Global average temperature anomaly compared to 1861-1890 pre-industrial period with 95% confidence interval, adapted from ref. (Ritchie, Rosado, and Roser 2023).*

reflected by the planet surface as infrared radiation, influenced by the carbon dioxide concentration (Kweku et al. 2018). If the equilibrium between GHG production and absorption shifts, the atmosphere concentration changes: as a consequence, the average global surface temperature changes as well. In Figure 2, the annual carbon dioxide production is reported in the same time span of Fig. 1, from 1850 to last years: the main countries and political unions are collectively shown, together with the production share of international aviation and shipping.

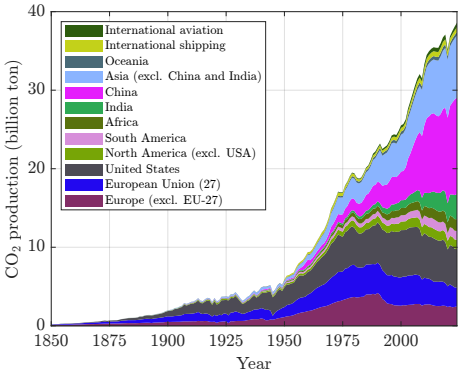


Figure 2 *Annual CO_2 emissions from 1850 to 2023 in billion tons shared between countries, international shipping, and aviation, adapted from ref. (Ritchie, Rosado, and Roser 2023).*

Comparing the CO_2 production to the temperature anomaly trends, it can be noted that the temperature anomaly steadily increases few years later any increase in the global carbon dioxide emission production. While older regions,

such as North America and Europe, are trying to reduce the GHG emissions with regulations, increasing economic growth in Asia pushes further away the produced emissions peak.

GHG emissions are caused by several sectors in different proportions, as shown in Figure 3: the main pollutant sectors are highlighted, with emissions expressed as equivalent carbon dioxide emissions.

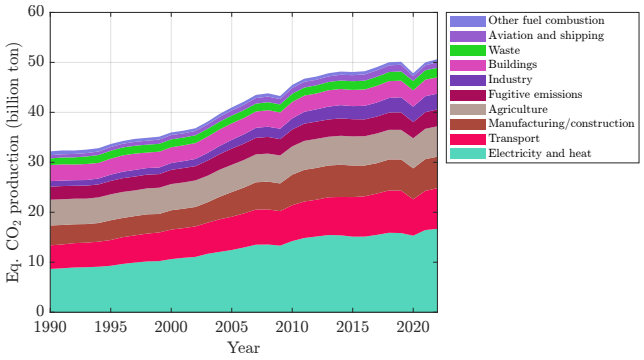


Figure 3 *Total greenhouse gas emissions expressed as equivalent CO_2 tons divided by sectors, from 1990 to 2021, adapted from ref. (Ritchie, Rosado, and Roser 2020).*

Starting from 1995, the transport sector is the second most pollutant sector after electricity and heat production, with almost 8 billion tons of equivalent carbon dioxide corresponding to 16% of total emissions in 2021.

Focusing on the transport sector only, in 2018 a total of roughly 8 billion tons of carbon dioxide have been produced globally. An insight of production share is shown in Figure 4, with every bar corresponding to a precise percent share based on vehicle typology.

It can be noted that passengers vehicles are responsible for 45.1% of total transport emissions, corresponding to roughly 3.6 billion tons: considering the total carbon dioxide amount of roughly 50 billion tons in 2018, the passenger vehicles alone covers 7.2% of global CO_2 emissions.

Policy makers are dealing with climate change and global warming with several laws and regulations for every strategic energy sector, establishing precise emissions limits and promoting renewable solutions. For transport sector in European Union, the actual emissions limits imposed by EURO-6 regulation to light-duty vehicles are shown in Table 1: these limits have been adopted since 2014 and, soon, EURO-6 will be replaced by EURO-7 regulations, with even stricter pollutants limits.

Hybrid vehicles come in hand to rapidly address this situation, in particular as a short- and mid-term solution. The benefit of using this technology, however, is closely linked to the way in which the electricity used to recharge the batteries

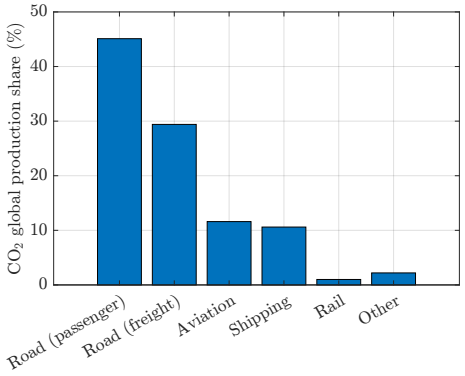


Figure 4 *CO_2 emissions due to transport sector in 2018 divided by vehicle type, adapted from ref. (Ritchie 2020).*

Table 1 *Regulated pollutant emissions for light-duty passenger vehicles, EURO-6, tested on World Motorcycle Test Cycle (WMTC) drive cycle, adapted from ref. (Mulholland et al. 2022).*

Pollutant	**Gasoline**	**Diesel**	**Units**
NO_x	60	80	mg/km
PN	6×10^{11}	6×10^{11}	#/km
PM	4.5	4.5	mg/km
THC	100	90	mg/km
CO	1	0.5	mg/km

is produced: the issue of lifecycle emissions from electric and rechargeable hybrid vehicles is debated and the results of analyses vary depending on the energy mix and the amount of energy produced from renewable sources (Axsen and Kurani 2013). In addition, the market share of hybrid and electric vehicles struggles to rise due to infrastructure limitations and high market costs, along with a general distrust in these technologies (R. Peng et al. 2024).

Motivations and objectives

It is clear that policymakers and car manufacturers need to make more efforts to achieve decarbonisation objectives. Hydrogen-fuelled vehicles are a promising and immediate, medium-, and long-term solution to address pollutant emissions reduction of this sector, allowing also new technologies to be implemented. The development of proper mathematical models to design and simulate powertrain components comes in hand to speed up optimisation and wide adoption of low-pollutant hybrid architectures: studying these systems allows to establish the physical mathematical equations that describe them and build sub-models, which must then be identified and validated using experimental data.

Among the various alternatives, hydrogen has emerged as a promising energy carrier thanks to its potential for clean and efficient energy conversion. PEMFC technology is one of the most attractive hydrogen-based one to be deployed for both stationery and mobility applications. However, its widespread adoption is currently hindered by durability, reliability and availability challenges. In this context, developing real-time models as digital twin for diagnostic purposes is essential to ensure safe operation, extend lifetime and support advanced control strategies.

On the other hand, the transport sector is exploring different approaches to integrate hydrogen with PEMFC-based powertrains. Comparative studies and simulations are a useful tool to design and evaluate the energy consumption, efficiency and environmental impact of these solutions, and to provide insight into their potential role in sustainable mobility. Although significant progress has been made in modelling components and simulating vehicles, there is still a gap in integrated approaches that connect advanced diagnostic tools for PEMFCs with system-level analyses of hydrogen-powered powertrains.

Taking advantage of this background, the work presented in this dissertation has two main objectives. Firstly, it aims to develop a lumped real-time model for PEMFC monitoring and diagnosis applications, demonstrating its applicability in monitoring and control scenarios. Secondly, it aims to design and simulate hybrid powertrains powered with PEMFC stack, focusing on performance, efficiency and energy consumption, in order to optimise vehicle management on

high-level. By addressing both component- and system-level factors, this thesis aims to provide modelling and simulation tools, from model-based design to model-based control, to support academic research and industrial applications, contributing to the advancement of hydrogen technologies for reliable, efficient, and sustainable mobility.

Contributions

To pursue the discussed objectives, this thesis is structured as follows:

- After the introduction, the current status of hydrogen implementation for sustainable mobility is given, from production to technology, together with hints on hybrid vehicles.
- An analytical dynamic model based on the water balance at the Polymer Electrolyte Membrane (PEM), the key component of every PEMFC, is developed and tested in different conditions, in order to assess and evaluate the membrane dynamic behaviour.
- A PEMFC dynamic lumped model based on mass balances, membrane dynamics, thermodynamics, and polarisation performance is presented, with the main purpose of on-board monitoring, model-based control, and diagnosis.
- The modelling design framework of a PEMFC hybrid electric vehicle is presented, from the analysis of the component to the identification of the best hybrid layout and control strategy, based on user needs and electrical complexity.

The contextual foundation is essential to frame the subsequent modelling activities within the broader perspective of hydrogen's role in decarbonization strategies. The PEMFC model, integrated with the membrane analytical dynamic one, represents a significant contribution in this field, balancing computational simplicity with physical accuracy and making it suitable for on-board applications, such as monitoring, diagnosis, prognosis, and control. By capturing the essential dynamics of PEMFC behaviour, it provides a tool that can be integrated into real-time vehicle management systems, thereby advancing both theoretical understanding and practical implementation. Finally, the work extends its scope to the modelling and simulation of a pure electric vehicle equipped with a hydrogen-fuelled range extender. This contribution encompasses the design and identification of the hybrid powertrain as well as the definition and evaluation of control strategies aimed at optimizing energy efficiency. The simulations demonstrate the feasibility and advantages of hydrogen-based hybridisation under different operating conditions.

The two proposed modelling approaches differ substantially in their purpose. The PEMFC model serves as a digital twin of a real PEMFC system in order to perform model-based monitoring and diagnostic analysis. The hybrid vehicle model, on the other hand, is designed for the investigation of powertrain layouts efficiency. Taken together, these contributions advance the state of knowledge in three interconnected domains: hydrogen technology assessment, PEMFC modelling for fast and reliable simulations, and hybrid vehicle powertrain design and optimization. The integration of these elements provides a complete framework that supports the development of efficient, sustainable, and technologically viable hydrogen-based mobility solutions.

Chapter I
Hydrogen for sustainable mobility

In this chapter, a brief review on hydrogen utilisation in the transport sector is given. Hydrogen is a useful energy carrier that can fuel zero emissions devices, i.e., fuel cells, to produce electricity with no pollutants at all; if the hydrogen production process involves energy coming from renewable sources, the entire process from production to usage can be assumed as pollutant-free. The recent developments of fuel cells powered with pure hydrogen foster the usage of these electrochemical devices within the automotive sector, thanks to high energy density and scaling-up versatility. Hybridisation is another key aspect of sustainable mobility: combining the advantages of green systems together with energy buffers, i.e., battery systems, allows to optimise vehicles powertrain, consuming minimum amounts of hydrogen fuel while achieving zero pollutant emissions.

I.1 Advantages and issues of hydrogen utilisation

Hydrogen is the most diffused chemical element in nature, being 75% of the entire universe mass. Its usage as energy carrier is strongly promoted by the high energy content it is able to carry, equal to almost three times the energy contained in standard fossil fuels; however, it has the lowest mole weight among all the nature elements, causing issues from extremely low density to atomic leakage. Hydrogen shows great potential in different energy sectors, from stationary energy production to traction power systems, with general high efficiencies with respect to traditional systems and cleaner operations (Osman et al. 2022).

I.1.1 Physical properties

At standard and ambient conditions, hydrogen is an odourless, colourless gas; in free space it tends to expand extremely fast because of weak intermolecular forces. The main physical properties of hydrogen are collected in Table I.1.

Table I.1 *Hydrogen physical properties, adapted from ref. (Keçebaş and Kayfeci 2019).*

Description	**Value**	**Units**
Standard density	0.082	kg m^{-3}
Atomic weight	1.008	u
Boiling point	20	K
Critical point	33	K
Freezing point	13	K
Molecular weight	2	g $mole^{-1}$

The low density is one of the main issues in hydrogen usage: to obtain a sufficient hydrogen volume, high compression systems or critical coolers are needed. However, when compared to widely used fossil fuels, hydrogen shows the greatest energy carrying capability: the main chemical properties are highlighted in Table I.2.

Table I.2 *Hydrogen physical properties, adapted from ref. (Keçebaş and Kayfeci 2019).*

Property	**Hydrogen**	**Methane**	**Diesel**	**Gasoline**	**Units**
Lower Heating Value	119.9	50.0	42.5	44.5	MJ kg^{-1}
Minimum Ignition Energy	0.017	0.30	–	0.29	MJ
Auto Ignition Temperature	585	540-630	180-320	260-460	°C
Combustible Range	4-75	5-15	0.6-5.5	1.3-7.1	%

As it can be seen, the hydrogen lower heating value is the highest among the traditional fuels, with the lowest minimum ignition energy and the widest combustible range: these features make hydrogen a convenient fuel for internal combustion engines that can run on ultra-lean mixtures. However, the wide

combustible range poses, on the other hand, flammability safety risks that have to be addressed; these safety risks can be critical also in low temperature energy production systems and refuelling stations, due to hydrogen leak through most of cavities (Hu et al. 2024).

I.1.2 Production technologies

One of the key problems with hydrogen usage is fuel availability: as it stands, there is negligible molecular hydrogen availability around the world, since hydrogen atoms are mostly present in chemical bounds with other substances (i.e., water, methane, organic compounds, etc.). The need of hydrogen production explains why hydrogen is commonly considered as an energy carrier, instead of a pure energy source. There are a variety of ways to produce hydrogen, using different energy sources and extracting hydrogen from various chemical compounds (Dash, Chakraborty, and Elangovan 2023). Based on production technology, hydrogen is classified with several colours:

Blue Conventional hydrogen production processes involving fossil fuels, reducing CO_2 emissions implementing carbon capture techniques (Sazali 2020). The average carbon intensity is in the range 1-4 kilogram of equivalent CO_2 emitted per kilogram of hydrogen produced, with an efficiency ranging from 60% to 70% (Bauer et al. 2022).

Purple Water electrolysis fed with electrical energy produced with nuclear plants (Pinsky et al. 2020). The average carbon intensity is in the range 0.5-1.5 kilogram of equivalent CO_2 emitted per kilogram of hydrogen produced, with an efficiency ranging from 60% to 80% (Incer-Valverde et al. 2023).

Turquoise Methane pyrolysis, thermally splitting the hydrocarbon in black carbon and hydrogen (Amin, Croiset, and Epling 2011). The average carbon intensity is in the range 1-3 kilogram of equivalent CO_2 emitted per kilogram of hydrogen produced, with an efficiency ranging from 45% to 55% (Riley et al. 2021).

Grey Steam methane reforming with no carbon capture (Kannah et al. 2021). The average carbon intensity is in the range 9-12 kilogram of equivalent CO_2 emitted per kilogram of hydrogen produced, with an efficiency ranging from 65% to 75% (Saha et al. 2024).

Green Water electrolysis fed with electrical energy produced from renewable sources (Oliveira, Beswick, and Yan 2021). The average carbon intensity is in the range 0.5-2.5 kilogram of equivalent CO_2 emitted per kilogram

of hydrogen produced, with an efficiency ranging from 60% to 80% (Bhandari, Trudewind, and Zapp 2014).

White Extraction of natural hydrogen from underground reservoirs (Aimikhe and Eyankware 2023). The average carbon intensity is lower than 0.5 kilogram equivalent CO_2 emitted per kilogram of hydrogen produced (Zgonnik 2020); the efficiency is not evaluable.

The crucial distinction between hydrogen colours is the pollutant emissions during the production process: grey hydrogen production produces the worst pollutant emissions amount, while purple and green hydrogen are the ones with the lowest carbon footprint. On the other hand, the grey hydrogen is mostly produced in Europe, with current 96% share (Dulian and Erbach 2025). White hydrogen also is a zero-emission one, even if hydrogen reservoirs are extremely limited. It has to be considered that carbon-based hydrogen production processes usually lead to impurities, from carbon monoxide to carbon dioxide and sulphuric-based substances, that need to be removed: impurities can further react in combustion processes leading to non-zero pollutant emissions, while in electro-chemical devices they can accelerate degradation processes (Murugan and Brown 2015).

I.2 Fuel cells technology

The key technology that exploits pollutant-free hydrogen energy is fuel cell. A fuel cell is an electrochemical device that converts hydrogen and oxygen in water with a reduction-oxidation reaction (ROR):

$$H_2 + \frac{1}{2}O_2 \rightarrow H_2O \tag{I.1}$$

The chemical reaction frees electrons, resulting in usable DC electrical energy to power any electrical load (Larminie and Dicks 2003). The ROR rate is influenced by the presence of catalyst particles in the reaction sites: without catalyst, the reaction would not be promoted. Every fuel cell is made of three fundamental components:

Anode One of the two electrodes, serves as reaction site for hydrogen oxidation and electrical conductor for electrons flow.

Cathode Electrode devoted to the oxygen reduction process, made of electrical conductive material and water production site.

Electrolyte Reactants physical barrier, allowing only ions flowing between the two electrodes.

The ideal fuel cell performance is given by the variation of Gibbs free energy. The reversible open circuit voltage is a function of temperature with the following relationship:

$$E_0(T) = -\frac{\Delta\bar{g}(T)}{2F} \tag{I.2}$$

where $\Delta\bar{g}$ is the molar variation of Gibbs free energy that depends on reaction temperature and catalyst material, while F is the Faraday's constant corresponding to the charge of one mole of electrons equal to 96485 $A \cdot s \cdot mol^{-1}$. The reversible OCV, as function of temperature, is shown in Figure I.1.

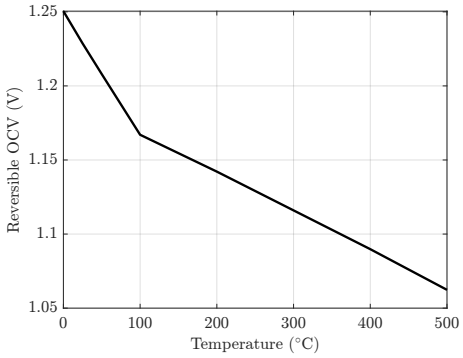


Figure I.1 *Reversible open circuit voltage produced by hydrogen-oxygen ROR.*

As it can be seen, the reversible open circuit voltage scales down from 1.23 V at 25°C to 1.18 V at 80°C (Wee 2007) considering only liquid water conditions: a single cell is often not enough to produce the required electrical power. Because of this, several cells can be modularly combined in a stack arrangement in series electrical layout, in order to share the same current while increasing the total voltage. To do so, bipolar plates are used to ensure reactants feeding to every single cell of the stack, while guaranteeing electrical conductivity and mechanical seal (Hermann, Chaudhuri, and Spagnol 2005). Furthermore, the stack must be supported by auxiliaries components to ensure proper reactants flow, cooling, and electrical management: this is namely called Balance of Plant (BoP). Thanks to the direct conversion of chemical energy in electrical energy, with only the reaction temperature influence, the fuel cells ideal efficiency is not limited by Carnot theorem, making able to reach ideal efficiency values higher than traditional power generation systems (Giorgi and Leccese 2013); an example considering ambient temperature as cooling temperature is reported in Figure I.2, with fuel cell ideal efficiency depicted with solid line and Carnot limit efficiency with dashed line.

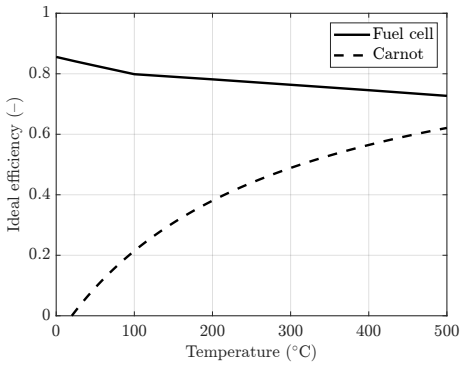


Figure I.2 *Comparison between fuel cell ideal efficiency and Carnot theorem with 20°C heat sink temperature.*

I.2.1 Classification of fuel cells

Based on the electrolyte material and working temperature range, in Table I.3 the main classification of principal fuel cells technologies is presented.

The electrochemical reactions happening inside fuel cells are promoted thanks to catalyst particles injected inside the electrodes; the different technologies differ also on catalyst material, from platinum to less noble metal alloys, further motivating the different temperature ranges (Singla, Nijhawan, and Oberoi 2021). The presented fuel cell technologies show several differences: the PEMFC technology is the preferred choice within fast applications and low temperature, together with high specific power (Pramuanjaroenkij and Kakaç 2023). Vehicles powered with fuel cells are namely considered hybrid, since the energy buffer capability provided by the battery is needed to satisfy sudden variations in power load requested by the driver (Lü et al. 2018). However, this class of fuel cells requires hydrogen with high purity, since the platinum catalyst particles are sensible to carbon contaminants. When high efficiency is needed, the Solid Oxide Fuel Cells (SOFC) are suitable for those applications, with good fuel tolerance, cheap catalyst materials, and high nominal power; on the other hand, these systems are extremely slow. The other technologies named in the Table I.3 are not spread as the previous mentioned. Fuel cells can cover different sectors application, from portable to stationary power generations up to transportation systems: for each sector, a single technology is better suited among the others, based on transient response, operating temperature, and maximum power targets (Sharaf and Orhan 2014).

Table I.3 *Classification of widely used fuel cell technologies, based on electrolyte material, adapted from ref. (Sharaf and Orhan 2014).*

Type	Electrolyte	Fuel	Charge carrier	Temperature
PEMFC	Proton exchange membrane	Hydrogen	H^+	60-80°C
SOFC	Solid oxide	Hydrogen, methane	O^{--}	800-1000°C
MCFC	Molten carbonate	Methane	CO_3^{--}	600-700°C
PAFC	Phosphoric acid	Hydrogen	H^+	Below zero-230°C
DMFC	Proton exchange membrane	Liquid water-methanol solution	H^+	Ambient-110°C

I.2.2 Proton Exchange Membrane Fuel Cells

PEMFC technology is one of the main solutions for sustainable powertrain development, reducing the environmental impact. Differently from traditional power generation systems, this class of fuel cells produce no exhaust emissions; the only byproduct is the liquid water, due to the working temperatures lower than 100°C. The ROR reaction happening inside the PEMFCs is based on the hydrogen oxidation in free protons and electrons happening at the anode side:

$$H_2 \rightarrow 2H^+ + 2e^- \tag{I.3}$$

Due to the electrical conductive material of the electrodes, the electrons are free to flow outside the cell following the potential direction, powering the electrical load connected to the cell. The protons, on the other hand, are forced to flow through the electrolyte: for this application, polymeric membrane are used to ensure protons flow from anode to cathode while impeding the reactants cross-flow. On the cathode side, water is generated with the following reduction reaction:

$$2H^+ + 2e^- + \frac{1}{2}O_2 \rightarrow H_2O \tag{I.4}$$

The electrodes are conventionally divided in two main regions: (i) Gas Diffusion Layer (GDL), through which the reactants can diffuse from the external down to the reaction sites; (ii) Catalyst Layer (CL), in which the most of catalyst particles are located. For PEMFC, platinum catalyst is required: due to the low working temperature, high noble material is fundamental to ensure enough activation energy for the reaction to sustain (Barbir 2013). The gases are provided to the single cell with external channels, namely Gas Flow Channel (GFC). A simple schematisation of PEMFC working principle is provided in Figure I.3, in which the electrodes and their sub-volumes are shown, together with reactants flows.

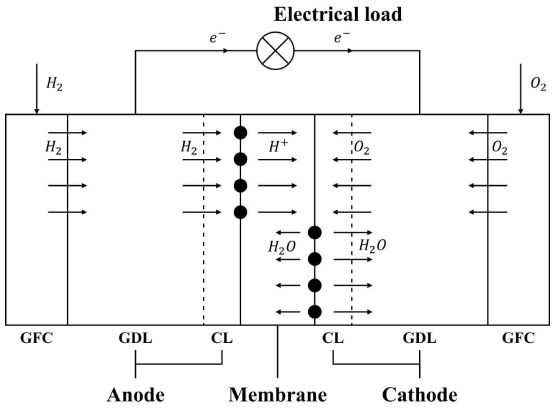


Figure I.3 *PEMFC single cell schematic, with electrodes, membrane, and gases flows highlighted.*

In the CL, the co-existence of electrode material, catalyst particle, and membrane material is identified as Triple Phase Boundary (TPB). The TPB is fundamental for the two semi-reactions to take place: it comprehends the catalyst particle surface where the reaction locally takes place. On the anode side, the electrode conductive material is needed to pave the way for the electrons flow to the load circuit; on the cathode side, the electrons come back through the electrode. The membrane material is also necessary, since the protons flow is promoted only through the membrane itself (Van Dao et al. 2019).

The single cell real voltage is not equal to the reversible potential shown with eq. (I.2): several irreversible losses have to be accounted, caused by insufficient reactants amount, membrane Ohmic resistance, electrodes liquid water saturation, and reactants cross-flow. In general, the actual fuel cell voltage can be described by the following polarisation curve:

$$V_{FC} = E_{Nernst} - V_{act} - V_{Ohm} - V_{conc} - V_{off} \tag{I.5}$$

where each term describes a single phenomena (Barbir 2013). The Nernst potential E_{Nernst} expresses the influence of operating conditions, i.e., cell temperature and reactants pressure, on the open circuit voltage as follows:

$$E_{Nernst} = E_0\,(T) + \frac{\tilde{R}T}{2F}\log\left(\frac{a_{H_2}a_{O_2}^{\frac{1}{2}}}{a_{H_2O}}\right) \tag{I.6}$$

where a_{H_2}, a_{O_2}, and a_{H_2O} are hydrogen, oxigen, and water activities, respectively. The activation losses V_{act} are caused by a non-equilibrium imbalance when the requested current is higher than the chemical equilibrium, meaning that a portion of energy is needed to sustain the chemical reaction (Husar, Strahl, and Riera 2012). The activation losses are expressed with the Tafel formulation:

$$V_{act} = a_{Tafel}\log\left(\frac{i}{i_0}\right) \tag{I.7}$$

where a is namely the Tafel slope, while i_0 is the exchange current density when chemical equilibrium is reached. The Ohmic losses V_{Ohm} are mainly caused by the Ohmic resistance slowing down the protons flow across the membrane and they are proportional to the current:

$$V_{Ohm} = ri \tag{I.8}$$

where r is the membrane area resistance. The membrane resistance is influenced by both the cell temperature and the membrane water content (Springer, T. A. Zawodzinski, and Gottesfeld 1991). The concentration losses V_{conc} are caused by reactants concentration gradient across the porous electrodes: the reaction rate must be lower than the feeding amount limited by the diffusive process, causing an overvoltage (Haji 2011). The concentration losses are expressed with the following formulation:

$$V_{conc} = c_{over}\log\left(\frac{i_{lim}}{i_{lim} - i}\right) \tag{I.9}$$

where c_{over} is an overvoltage coefficient, while i_{lim} is the limiting current density due to diffusive speed. The offset losses term V_{off} accounts for every other non-linear irreversibility, from reactants crossover to electrons crossover.

The Proton Exchange Membrane (PEM) is the main cell component, and it serves to three different functions : (i) guarantee the movement of proton charges from anode to cathode; (ii) physically separate reactants; (iii) electrically insulate the electrodes (Peighambardoust, Rowshanzamir, and Amjadi

2010). Its structure is composed by polymeric chains with three main elements: (i) a Polytetrafluoroethylene (PTFE) backbone, to ensure chemical and thermal stability; (ii) sulfonic acid groups SO3-, to allow the proton flow across the membrane; (iii) side chains, to link backbone and sulfonic groups (Valenzuela et al. 2009). The PTFE backbone is hydrophobic to avoid that water molecules adhere on its surface, whereas sulfonic groups are hydrophilic to guarantee that water molecules and protons can be absorbed, thus promoting protons transport with high water content. It is worth recalling that water and proton form the hydronium H3O+ ion, which acts as a proton carrier within the membrane (Ji and Wei 2009). As a result, the membrane is permeable to water. The movement of protons across the membrane is based on two main ions transport mechanisms, namely Grotthus hopping, according to which protons jump from one sulfonic group to another, and vehicular diffusion, where protons are carried by water molecules that spread through the membrane (Pan et al. 2021). Grotthus hopping is typically predominant at low water content, while vehicular diffusion occurs only in presence of water. Figure I.4 provides a schematic representation of the membrane structure along with the two mentioned ions transport mechanisms.

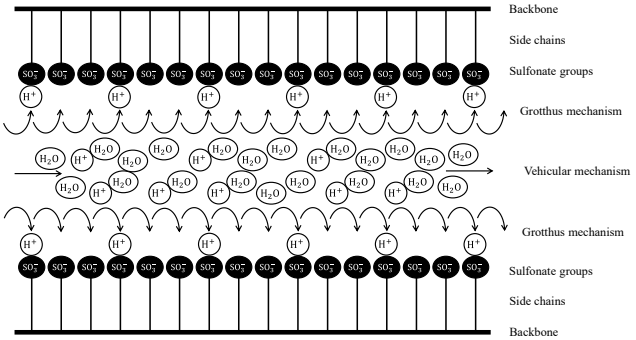


Figure I.4 *Schematic representation of PEM electrolyte structure and main protons transport mechanisms.*

The water membrane content is one of the key parameters to optimally manage the fuel cell, but it can't be directly measured, so a model representation is needed. With respect to the membrane volume, the three main water transport mechanisms are the following: (i) electro-osmotic drag, in which water is dragged by the ions flow through the membrane; (ii) hydraulic permeation, where the water flux is driven by pressure gradient across the membrane; (iii) diffusion, through which water flows thanks to concentration gradient across the membrane (K. Jiao and Li 2011). The three aforementioned mechanisms may occur in parallel, contributing to the overall water flow. However, to identify the net flux direction (i.e., from anode to cathode, or vice versa), the magnitude

and direction of each mechanism shall be properly identified. Electro-osmotic drag always follows the potential difference direction, hence the flux direction is always from anode to cathode, whereas both convection and diffusion are gradient driven (pressure and concentration, respectively), so water can move in either direction. Concentration gradient depends on the amount of water present in each electrode, specifically at CL sides at membrane boundaries. Hence, due to the water production occurring at cathode side, there is an intrinsic unevenness, which can be compensated through the humidification of the gases fed to the electrodes. From this physical description, it emerges the role of proper balance of the water transport mechanisms across the membrane and the humidification of the electrodes. Moreover, it is evident that the complexity of the several transport mechanisms can be described through non-linear equations, which require an accurate modelling analysis to achieve effective water management strategies to ensure the best water membrane content.

The performances of the PEMFCs are strictly related to the humidification of the cell itself: in literature, the problem of the cell's humidification is referred as water management. The working principle of PEMFCs relies on the ionic transport through the electrolyte, i.e., the membrane: water molecules inside the membrane are necessary to the ionic transport, hence the membrane must be humidified, otherwise the performances drastically drop due to drying. When drying occurs for a long time, membrane can become brittle with formation of cracks that causes the gases crossover through the membrane itself: the gases crossover causes uncontrollable chemical reactions leading to the formation of hot spots (Le Canut, Abouatallah, and Harrington 2006). On the other hand, if liquid water starves inside the cell, it can affect the reagent gases supply to the CL preventing them to reach the catalysts active areas: in this case, a flooding condition manifests and there is a worsening performances effect (Ijaodola et al. 2019). Water flooding is typical of cathode, since there is water production due to the electrochemical reaction, even if anode flooding can happen due to vapour water condensation in case of moist hydrogen supply to the cell (Kim et al. 2014). Many solutions can be applied to mitigate the problem of cathode flooding, from structural to design modifications of CL and GDL (Okonkwo and Otor 2021). The wettability of the GDL has a direct impact on the water removal rate: three-dimensional simulations support the wetting analysis, but the computational burden makes this diagnosis approach not suitable for on-board monitoring. The addition of a Micro-Porous Layer (MPL) between GDL and CL can positively impact the water management: due to the low porosity of the added layer, water removal is increased (Pourrahmani, Moghimi, and Siavashi 2019). The water removal rate is strictly connected to the water emersion from the GDL: water emerges as droplets that interacts with the air flow in the cathode. The main phases of water droplets are in order: emersion, oscillation, and detachment (Polverino, Esposito, and Pianese 2013).

The coalescence between adjacent droplets can increase the water removal rate: bigger water droplets are subjected to a greater shear force, leading to a faster detachment; in case of low air speed, the coalescence between adjacent droplets can cause the formation of a water film (Esposito, Pianese, and Guezennec 2010).

The need to have a fast estimator of water content is fundamental for control and monitoring purposes since typical three-dimensional analyses have a high computational burden. Many authors investigated the implementation of control-oriented models for motive applications: it is difficult to find a good balance between computational burden and computational time. One of the main approaches widely adopted in literature is the Mean Value Model, in which the stack and the plant are divided in finite sub-volumes, each one with their characteristic dynamic equations to be numerically solved (Pukrushpan, H. Peng, and Stefanopoulou 2004). A circuital modelling of PEMFCs is also possible to represent both static and dynamic behaviours under different load conditions (Benchouia et al. 2013). Predicting water content is fundamental to ensure PEMFC performances and minimizing its degradation: detailed simulation models can be useful to deeply understand physical phenomena, but only real-time models are suitable for on-board real-time monitoring (Nandjou et al. 2016).

I.3 Hybrid vehicles generalities

A hybrid vehicle is a vehicle powered by more than one power source: fixing the power demand by the driver or the road load, the delivered power is divided between power sources, leading to additional degrees of freedom of the powertrain (Gao, Ehsani, and Miller 2005). Most of hybrid vehicles consider an internal combustion engine coupled with a battery capable of delivering a certain amount of power comparable to that of the engine, differently from traditional vehicles where the battery serves only for start-up phases. In the last decade, the role of internal combustion engines has been replaced by PEMFC systems, using hydrogen as primary chemical energy source (Lü et al. 2018). The main advantage of using more than one power source is the possibility to run the internal combustion engine or the PEMFC in better efficiency operating conditions, by, e.g., decoupling the power request from the chemical energy power component or extending the vehicle range. In both cases, a reduction in fuel consumption and pollutant emissions is still achieved, while the power request by the driver can still be satisfied (W. Liu 2013). On the other hand, an increase in vehicle complexity and, often, components number occurs. It shall be noted that, to achieve a reduction in fuel consumption, a proper Energy Management Strategy (EMS) that manages the power outputs of each

powertrain component must be correctly designed and implemented (Krithika and Subramani 2018).

I.3.1 Classification of hybrid vehicles

A crucial design parameter to further characterize HEVs is the Degree of Hybridization (DoH), defined as the ratio between maximum power deliverable by the battery over the total maximum power of the powertrain as shown in the following:

$$DoH = \frac{P_b^{max}}{P_{chem}^{max} + P_b^{max}} \tag{I.10}$$

where P_{chem} is the maximum exploitable power by the chemical-based technology (i.e., internal combustion engine or PEMFC). Referring to traditional hybrids, based on the DoH a functional classification of hybrid vehicles is proposed in Table I.4: from micro hybrid to plug-in hybrid, many features are added to the powertrain with the reduction of engine size and increase in battery capacity (Govardhan 2017).

Together with DoH, hybrid vehicles design is also characterized by the battery capacity: lower battery capacity serves only to engine start-up and, in some cases, to start-stop features for micro-hybrids; to gain advantage of hybridization, the battery pack must be able to store enough energy. Typically, the battery capacity increases with DoH. When it comes to pure electric vehicles, the battery alone must accomplish every power requirement together with guaranteeing enough mileage to the driver; hence, the recharging technology for this class of batteries is more sophisticated with respect to hybrid vehicles, allowing fast recharging times. On the other hand, fast recharging technologies are critical for battery life and durability, while slow charging preserves battery life.

The layout of a hybrid vehicle powertrain is characterized by multiple energy flows exchanged among the present power systems (Overington and Rajakaruna 2012). With reference to traditional hybrids, three main layouts can be identified (K. V. Singh, Bansal, and D. Singh 2019):

Series The internal combustion engine directly charges the battery, sustaining the state of charge. To do so, the internal combustion engine is coupled with an electric generator and the proper power electronics. The traction power is provided by electric motors only.

Parallel The internal combustion engine contributes directly to traction power, while the battery feeds an electric motor. The mechanical power is shared

Table I.4 *Functional classification of hybrid vehicles based on degree of hybridization.*

Classification	**Degree of Hybridisation**	**Features**
Zero hybrid	0%	ICE start-up
Micro hybrid	< 10%	Start/Stop, Regenerative braking
Mild hybrid	10–30%	Start/Stop, Regenerative braking, Power assistance
Full hybrid	> 40%	Start/Stop, Regenerative braking, Power assistance, Short electric drive
Plug-in hybrid	> 50%	Start/Stop, Regenerative braking, Power assistance, Extended electric drive, Plug-in capability
Full electric	100%	Regenerative breaking, Full electric drive, Plug-in capability, No ICE

to the wheels through a common mechanical axle. In this configuration, the battery and the electric motor serve mainly for boosting purpose.

Mixed The internal combustion engine is able to both drive the wheels and to recharge the battery with a proper electric generator. The battery, on the other hand, feeds an electric motor for power boost. This configuration is the most complex and it combines advantages of both series and parallel layouts.

About fuel cell Hybrid Electric Vehicle (HEV) technology, the main difference with traditional hybrids is the energy conversion chain. In case of traditional hybrids, the chemical energy within the fuel is firstly converted to mechanical energy with a thermodynamic cycle thanks to the internal combustion engine and then, based on the powertrain layout, it may or may not be converted in electrical energy. Looking at fuel cells hybrid vehicles, however, there is the direct transformation of chemical energy in electrical energy with no intermediate steps thanks to the fuel cell technology; hence, the fuel cell vehicle can be considered purely electrical from an energetic point of view. The number of energy conversions on traditional hybrid vehicles is higher than fuel cell hybrid vehicles: it can be reasonable to assume that the well-to-wheel efficiency of fuel cells hybrid vehicles can be higher than traditional hybrids (Arshad et al. 2019). Given this main distinction, the fuel cell HEV can be classified based on the electrical layout as shown in Figure I.5.

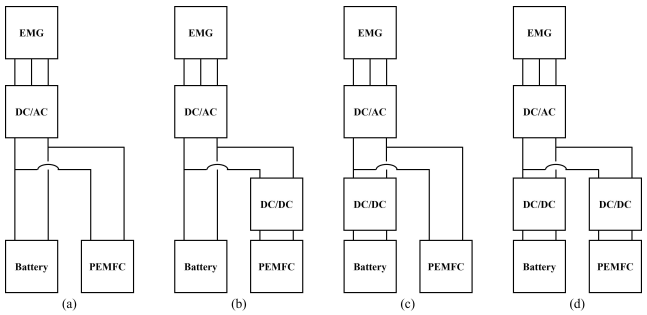


Figure I.5 *Fuel cells hybrid vehicle electrical layouts, adapted from ref. (Sorlei et al. 2021): (a) T1; (b) T2; (c) T3; (d) T4.*

In the first topology T1, battery and PEMFC stack are passively connected in parallel to the DC/AC converter: for this configuration, there is no voltage conversion, hence battery and PEMFC voltage characteristics must be compatible with DC/AC converter. From the second topology T2 to T4, DC/DC converters are progressively added to the energy sources side: the presence of DC/DC converters allows to better couple the components with great differences in

voltage capabilities, gaining the maximum powertrain control flexibility considering T4 layout (Aziz et al. 2015), at the expense of higher energy dissipation and powertrain complexity. Another possibility is given by adding a further degree of freedom to the system with the implementation of ultra-capacitors, an electrical energy buffer with high specific power and low specific energy that can be useful to manage sudden load variations (Xun, Y. Liu, and Holmberg 2018).

I.3.2 Control strategies overview

The additional degree of freedom given by the coexistence of more power components requires a proper control strategy implemented within the Electronic Control Unit (ECU). Since the battery acts as an energy buffer for the powertrain, the control strategy typically assumes battery power as control variable to manage fuel consumption while satisfying vehicle power demand (Munsi and Chaoui 2024). The ECU should accomplish different objectives while optimizing components at different complexity levels: this is generally referred to as multilevel control architecture, in which two or more levels are defined as objectives and actuation strategies (Sciarretta and Guzzella 2007).

The architecture of every multi-level control strategy is divided into three main levels described hereafter:

High level The power split controller establishes the amount of power that must be delivered by the different power sources following a pre-defined logic; the power split logic is the main core of the overall control strategy, and it has direct effects on fuel consumption.

Medium level This level defines the optimal combination of component parameters to ensure the single power delivery as established by the high-level controller; to fulfil the efficiency optimisation, the efficiency must be maximised for the single power component as well.

Low level It involves the actuators for the ICE and the battery, actuating the required component parameters.

For a PEMFC hybrid vehicle, in Figure I.6 a simple schematisation of a multi-level control strategy architecture is depicted.

The high-level control logic is the core of the entire strategy: its definition has direct consequences on fuel consumption and vehicle global efficiency. The high level can be based on heuristic approaches, or it can be de-rived from an optimal algorithm.

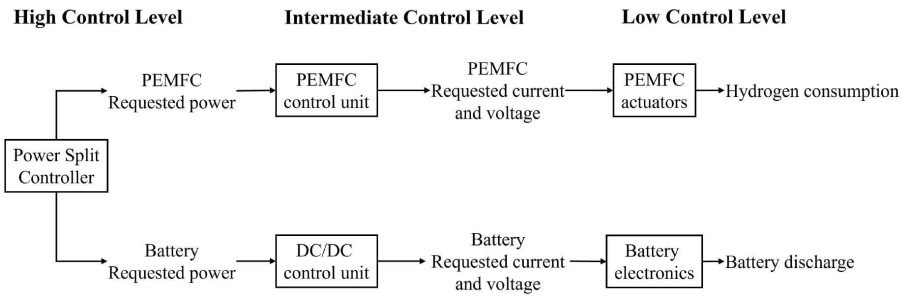


Figure I.6 *Multilevel control architecture schematization for HEVs.*

Heuristic approach

With the heuristic approach, the developed control strategy neither follows an optimality criterion nor uses past or future information; instead, it is based on reasonable assumptions coming from real-life practice or simple considerations about powertrain behaviour and limits. Mainly, a deterministic rule-based strategy is applied: simple activation rules and state machines are defined to satisfy a given condition based on the vehicle state, in particular the battery State of Charge (SoC) (Cervone, Sicilia, Romano, et al. 2023). Normally, the rule-based control strategies ensure that the SoC does not fall outside a given range with a thermostat control activation on the other power source to compensate for every discharge (i.e., charge sustaining); alternatively, it is possible to define a given battery discharge rate, using the battery as an electrical assist to the powertrain (i.e., charge depleting). Rule-based strategies are suitable for micro and mild hybrid, mainly series-layout configurations, but they are neither capable of minimizing fuel consumption nor of correctly managing the hybrid powertrain, especially in the case of plug-in configurations (Banvait, Anwar, and Y. Chen 2009). Another possibility is represented by fuzzy logic control strategies, in which the rule-based concept is extended to overcome said limitations. Fuzzy controllers still need predefined rules, but the transition between rules is not step-like in the case of simple rule-based controllers: this time, the control output is a mix of different rules, known as fuzzification, allowing a more coherent control of powertrain dynamics (Maghfiroh, Wahyunggoro, and Cahyadi 2024). To manage the fuzzification process, different membership functions in the literature can be found, such as trapezoidal rules, Singleton fuzzifiers, Gaussian-type fuzzifiers, etc. For PEMFC-based hybrid vehicles, the rule-based EMS can also implement additional criteria like PEMFC temperature stabilisation for optimal performance (P. Singh et al. 2025).

Optimal control

In the case of optimal control strategies, a mathematical constrained minimization problem is defined for each specific application. In general, a cost function J_{cost} that involves fuel consumption $\dot{m}_f$ must be minimised for a given driving cycle:

$$J_{cost} = \int_0^{t_{end}} \dot{m}_f \left(t, x\left(t\right), u\left(t\right)\right) dt \tag{I.11}$$

where $x\left(t\right)$ is the problem state variable, while $u\left(t\right)$ is the control variable. Both state and control variables can be single or a set. The cost function can also be improved by implementing penalty factors for pollutant emissions, moving from pure fuel consumption to minimization to a multi-objective problem (Böhme and Frank 2017). For HEVs, battery SoC is usually assumed as the only state variable, while battery power is used as control variable; furthermore, a penalty function depending on the final SoC value is usually considered to ensure a certain discharge rate over the entire driving cycle.

$$J_{cost} = \int_0^{t_{end}} \dot{m}_f \left(t, x\left(t\right), u\left(t\right)\right) dt + \phi\left(\xi\left(t_{end}\right)\right) \tag{I.12}$$

The minimisation problem should also account for feasible limits, such as power limits, battery SoC limits, and power rates. The choice of the time span is crucial: a long time range allows to include a larger set of information, with a severe computational burden on the other hand. The time range must be coherent with the driving conditions, differing between city conditions and highway roads (Rezaei and Burl 2015).

Dynamic Programming

Dynamic Programming (DP) is one of the main techniques to approach the fuel consumption minimisation problem for hybrid vehicles (R. Wang and Lukic 2012): its implementation guarantees a globally optimal solution over the drive cycle within the constraints; on the other hand, it requires a heavy computational burden both for memory usage and CPU operations, with computational time exponentially growing with the problem complexity. In addition, DP allows the calculation of an optimal solution for fuel consumption minimisation, but it is not implementable on-board for big time ranges, leaving only an offline minimisation (Polverino, Arsie, and Pianese 2021).

To implement DP, a discretisation of time, state, and control variables must be introduced, typically with constant time step: the discretised version of the

cost function can be derived from eq. (I.11) as shown below.

$$J_{cost} = \sum_{k=0}^{N-1} \dot{m}_f \left(t^k, P_b^k\right) \Delta t + \phi \left(\xi^N\right) \tag{I.13}$$

with k as time step index, and N as the total number of time-steps. The penalty function on the final SoC value is a simple step function that is equal to infinity in the case of the constraint violation; otherwise, it is equal to zero. To determine the optimal solution, the algorithm proceeds backward over time: for a given k time instant, the span of every possible SoC value for the next time step is calculated with a direct explicit numerical difference scheme:

$$f_i^{k+1} = \xi_i + \dot{\xi}\left(\xi_i, P_b^k\right) \Delta t \tag{I.14}$$

where ξ_i is the given value of the SoC grid. The optimal battery power is the value corresponding to the minimum cost function according to the following:

$$P_{b_{opt}}^k = \text{argmin}_{P_b^k} \left\{J_i^{k+1} + \dot{m}_{f_i}^k \Delta t\right\} \tag{I.15}$$

The classical approach to this optimal algorithm is backward, in order to easily accomplish the final SoC constraint. A forward approach for DP is introduced by Donatantonio et al. (2022): since the DP calculates the control strategy profile backward, it is not guaranteed that the final solution computed forward would still be feasible. To overcome this issue, a time-independent formulation of minimization, which can run both forward (hence the name Forward Approach to Dynamic Programming, or FADP) and backward, is introduced, with a bijective correspondence between state variable (i.e., battery SoC) and control variable (i.e., battery power). In addition, another reason for using FADP is to compute the states of a dynamical system. Indeed, the computation of the system dynamics is only possible by performing a forward time marching to integrate the diffe-ential equations (e.g., the thermal dynamics of a battery). Since this algorithm is still computationally difficult to implement, an iterative variation was also proposed (namely Iterative Approach to Dynamic Programming, or IFADP) to narrow the SoC boundary grid while keeping the number of points intact, hence increasing the grid fitting with no expense on computational burden (Donatantonio et al. 2022).

Pontryagin's Minimum Principle

When the computational requirements of DP cannot be satisfied, Pontryagin's Minimum Principle (PMP) comes in hand: this algorithm allows us to find a sub-optimal solution, often close to the global optimum of DP, with

drastically low computation requirements and time (Y. Wang et al. 2018). The PMP algorithm starts with the definition of the Hamiltonian function as the instantaneous value of the original cost function:

$$H\left(t,\xi\left(t\right),P_b\left(t\right),\lambda_{co}\left(t\right)\right)=\dot{m}_f\left(t,P_b\left(t\right)\right)+\lambda_{co}(t)\dot{\xi}\left(\xi\left(t\right),P_b\left(t\right)\right) \tag{I.16}$$

where $\lambda_{co}\left(t\right)$ is the co-state variable needed for the accomplishment of the boundary SoC constraint, whose dynamics are defined by the following:

$$\dot{\lambda}_{co}=-\lambda_{co}\frac{\partial\dot{\xi}}{\partial\xi} \tag{I.17}$$

The PMP states that the necessary condition to reach the optimal solution is that every instantaneous condition is optimal: the Hamiltonian has to be minimised at every time-step.

$$H\left(\xi_{opt}\left(t\right),P_{b_{opt}}\left(t\right),\lambda_{co,opt}\left(t\right)\right)\leq H\left(\xi\left(t\right),P_b\left(t\right),\lambda_{co}\left(t\right)\right)\ \forall t\in[0,t_{end}] \tag{I.18}$$

The optimality condition is a necessary but not sufficient mathematical condition for the global problem optimality; hence, the PMP algorithm can only reach a sub-optimal solution, differently from DP. The initial co-state value must be calculated by imposing the respect of the final SoC value constraint: this leads to a non-linear problem that can be solved with classical methods known in the literature, such as the shooting or bi-section methods.

Equivalent Consumption Minimisation Strategy

In many applications in which the PMP algorithm is implemented, the co-state shows slight variations over time, especially when it is required that the SoC initial value must be maintained at the end of the cycle; hence, one can assume the co-state as a constant value, to simplify the mathematical treatment without the need to nest other minimisation algorithms to identify the initial value. Hence, the Hamiltonian can be rewritten as follows:

$$H\left(t,\xi\left(t\right),P_b\left(t\right)\right)=\dot{m}_f\left(t,P_b\left(t\right)\right)+s_0\dot{\xi}\left(\xi\left(t\right),P_b\left(t\right)\right) \tag{I.19}$$

where s_0 is the equivalence factory, namely corresponding to the constant co-state. The influence of the equivalence factor on the Hamiltonian is simply demonstrated: a high value of s_0 increases the weight on battery charging, while a low value of s_0 would lead to battery depleting. In general, the Equivalent Consumption Minimisation Strategy (ECMS) can be seen as a direct

derivation of the PMP algorithm (Serrao, Onori, and Rizzoni 2009). This is the main idea of ECMS: there is an optimal energy balance between the different power systems, including the battery; hence, the minimisation problem must also include the electrical energy delivered from the battery. To introduce electrical energy consumption, a key role is covered by the equivalence factor that establishes the weight of battery electrical power in the minimisation process.

Adaptive Equivalent Consumption Minimisation Strategy

The main limitation of the ECMS approach is that a constant equivalence factor is not capable of managing powertrain balance optimality in dynamic vehicle operative conditions, such as, for example, (i) road profiles with frequent slope variations; (ii) driving conditions, e.g., urban or highway; (iii) vehicle weight variation, such as in the case of the public transportation sector or delivery vans; and (iv) variable traffic conditions. Changing the weight factor on battery usage would increase the powertrain efficiency in situations in which the electric motor would be preferable or vice versa, still respecting component constraints.

Adaptive Equivalent Consumption Minimisation Strategy (A-ECMS) is used to address the aforementioned issue: the equivalence factor is not constant, but it can vary over time based on different criteria . The equivalence factor is once again dynamic and variable in time: a functional classification of different A-ECMS approaches is presented in Table I.5.

Table I.5 *Functional classification of A-ECMS for HEVs.*

Criteria	**Focus**
Adaptivity mechanism	SoC dependent Drive cycle Operative conditions
Time horizon	Short term Long term
Adaptation technique	Parametric optimization Real-time optimization Data-driven approach
Emerging technology integration	V2X communication system GPS integration AI-supported

The choice of one A-ECMS approach over another mainly depends on several factors such as data availability, computational resources, and scalability. Of course, different features can be combined implementing model-predictive control capabilities; Guo and An (2025) propose a integrated hierarchical A-ECMS for PEMFC-based heavy-duty vehicles, combining artificial intelligence, model-predictive control, and SoC following rules to optimise the powertrain operations.

I.4 Conclusions

In this chapter, a comprehensive review of the role of hydrogen in the transition toward sustainable mobility has been presented. The analysis confirms that hydrogen represents a promising energy carrier for the transport sector, characterised by a high energy content and the potential for a completely pollutant-free lifecycle, provided that green or white production pathways are utilised. Among the various electrochemical conversion technologies, PEMFCs stand out as a suitable solution for automotive applications due to their high specific power, fast response, and low operating temperatures.

However, several technical challenges remain to be addressed for the full-scale deployment of hydrogen-based powertrains. At the stack level, water management emerges as a critical factor for ensuring durability and performance. The delicate balance between membrane dehydration and liquid water flooding requires accurate, real-time modelling to prevent degradation and maximise efficiency. The review of current literature highlights that while complex three-dimensional simulations offer deep physical insights, there is a clear need for low-computational-burden models suitable for on-board monitoring and control.

Finally, the integration of PEMFCs into hybrid powertrain is essential to compensate for the slow dynamics of the fuel cell and to manage peak power demands through energy buffers like batteries. The effectiveness of these hybrid systems is strictly dependent on the EMS. While heuristic rules offer technical simplicity, optimal control strategies ranging from DP to A-ECMS are necessary to minimise fuel consumption and maintain the battery SoC in different driving conditions. These findings provide the theoretical foundation for the modelling and control architectures that will be developed and discussed in the following chapters of this thesis.

Chapter II
Membrane advanced lumped model for dynamic simulation

In this chapter, the advancements on PEM lumped modelling for dynamic simulation purposes are described and demonstrated. The main purpose of this activity is to define a rigorous assumption framework in which it is possible to write the membrane water balance equation that can be solved analytically with a good grade of approximation. This modelling activity is a major progress of a previous work (Ferrara, Polverino, and Pianese 2018). Then, applying the integral method, a general Ordinary Differential Equation (ODE) formulation can be identified, which can be easily implemented as a virtual sensor of the water content and, hence, the membrane Ohmic resistance.

II.1 Description of the problem

Following the work of Mazumder (2005), it is possible to write the membrane water balance, in terms of molar concentrations, accounting for the three main water transport mechanisms as shown below:

$$\frac{\partial c_w}{\partial t} + \boldsymbol{\nabla} \cdot \left(\mathbf{J}_{EOD} + \mathbf{J}_{conv} + \mathbf{J}_{diff} \right) = 0 \tag{II.1}$$

where c_w is the water molar concentration, while $\mathbf{J}_{EOD}$, $\mathbf{J}_{conv}$, and $\mathbf{J}_{diff}$ are, respectively, electro-osmotic drag, convective, and diffusive water molar fluxes. Since any water flow in membrane area plane can be neglected, the Partial Differential Equation (PDE) simplifies in the preferred dimension, i.e., the orthogonal direction from anode to cathode:

$$\frac{\partial c_w}{\partial t} + \frac{\partial}{\partial x} \left(J_{EOD} + J_{conv} + J_{diff} \right) = 0 \tag{II.2}$$

The PDE can be manipulated, exploding functional dependencies on problem state variable, i.e., the membrane water content λ.

II.1.1 Swelling effect

The water molar concentration is defined from the membrane water content as follows:

$$c_w = \frac{\lambda}{1+\delta} c_{mem}^{dry} \tag{II.3}$$

where δ is the swelling thickness fractional change, while c_{mem}^{dry} is the membrane molar concentration in dry conditions, a physical feature often provided by membrane's manufacturer. When the membrane is humidified it swells, increasing its volume: this behaviour is expressed by the thickness fractional change δ, which has been experimentally identified as proportional to λ (Springer, T. A. Zawodzinski, and Gottesfeld 1991):

$$\delta = \beta\lambda \tag{II.4}$$

where β is the swelling factor, identified to be equal to 0.0126. Other authors have introduced different functional relationships, increasing the model correlation at costs of non-linearities (Ferrara, Polverino, and Pianese 2018). The swelling effects can be decomposed from spatial coordinate x as shown below:

$$dx = (1+\delta)\, dx^{dry} \tag{II.5}$$

where dx^{dry} is the fixed spatial coordinate, with no swelling effect contemplated.

II.1.2 Electro-osmotic drag

The electro-osmotic drag flux is defined as the product between the number of water molecules dragged by a single proton and the number of protons produced by the hydrogen oxidation as follows:

$$J_{EOD} = n_d \frac{i}{F} \tag{II.6}$$

where n_d is the number of molecules dragger per proton, i is the current density, while F is the Faraday's constant. In literature, n_d is experimentally defined as the product between linear functions of temperature and water membrane

content, as reported by Ferrara, Polverino, and Pianese (2018):

$$n_d = \frac{(0.02T - 3.86)}{22.5}\lambda \tag{II.7}$$

Substituting eq. (II.7) into eq. (II.6), it is possible to write the electro-osmotic drag flux as shown below:

$$J_{EOD} = c_{mem}^{dry} u_{EOD} \lambda \tag{II.8}$$

where u_{EOD} is the transport's characteristic speed, defined as follows:

$$u_{EOD} = \frac{(0.02T - 3.86)\, i}{22.5 c_{mem}^{dry} F} \tag{II.9}$$

II.1.3 Convection

The convective transport molar flux is typically expressed as directly proportional to water concentration as follows (Mazumder 2005):

$$J_{conv} = c_w u_{conv} \tag{II.10}$$

where u_{conv} is the bulk fluid speed. The bulk speed can be calculated by means of Darcy's law, approximating the gradient pressure across the membrane as linear with the distance:

$$u_{conv} = -\frac{k_w}{\mu_w}\frac{p_c - p_a}{L_{mem}} \tag{II.11}$$

where k is the membrane permeability, μ_w is the water viscosity, while p_a and p_c are, respectively, anode and cathode's pressure at membrane boundaries. The membrane thickness L_{mem}, following the definition of membrane swelling introduced by Springer, T. A. Zawodzinski, and Gottesfeld (1991), changes with membrane humidification as follows:

$$L_{mem} = L_{mem}^{dry}\,(1 + \delta) \tag{II.12}$$

The swelling effect can be decomposed from bulk speed introducing the reference dry speed u_{conv}^{dry}:

$$u_{conv} = -\frac{k}{\mu_w}\frac{p_c - p_a}{L_{mem}^{dry}}\frac{1}{1+\delta} = \frac{u_{conv}^{dry}}{1+\delta} \tag{II.13}$$

Combining definitions of eqs. (II.3) and (II.13) into convective flux defi-

nition of eq. (II.10), it is possible to rewrite the convective transport flux as follows:

$$J_{conv} = c_{mem}^{dry} u_{conv}^{dry} \frac{\lambda}{(1+\delta)^2} \tag{II.14}$$

II.1.4 Diffusion

The water diffusive molar flux can be defined applying Fick's first law of diffusion as proposed by Springer, T. A. Zawodzinski, and Gottesfeld (1991):

$$J_{diff} = -D^{Fick} \frac{\partial c_w}{\partial x} \tag{II.15}$$

where D^{Fick} is the Fick diffusion coefficient. This flux term can be directed both from anode to cathode and vice-versa; however, since the water concentration is typically higher at cathode side, it is often directed from cathode to anode. Hence, the diffusive transport mechanism is generally called back-diffusion. Following the work by Ferrara, Polverino, and Pianese (2018), it is possible to separate thermal and water content effects on diffusion coefficient by means of the following dimensionless $\Gamma(\lambda)$:

$$\Gamma = \frac{D_a^{chem} f^{Darken}}{(1+\delta)^2} \tag{II.16}$$

where D_a^{chem} is the water chemical diffusion coefficient in Nafion 117 membranes, experimentally identified by T. A. J. Zawodzinski et al. (1991) as proportional to water activity a_w squared:

$$D_a^{chem} = a_w^2 \tag{II.17}$$

Furthermore, the Darken factor f^{Darken} can be expressed as an analytical expression of water activity a as proposed Ferrara, Polverino, and Pianese (2018), deriving it from the relationship between water membrane content λ and water activity a:

$$f^{Darken} = \frac{19.36 - 44.93 a_w + 40.29 a_w^2}{19.36 - 89.86 a_w + 120.87 a_w^2} \tag{II.18}$$

The Γ function plot as function of water membrane content λ is reported in Figure II.1. It can be noted that this dimensionless function is quite flat for $\lambda > 5$: this trend can be used later for problem linearisation.

The final diffusive water molar flux, combining eqs. (II.3), (II.5) and (II.16),

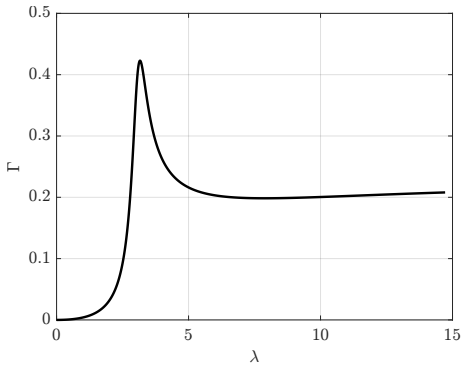


Figure II.1 *Dimensionless* Γ *function for diffusion coefficient characterisation with respect to water membrane content* λ*.*

can be rewritten as follows:

$$J_{diff} = -c_{mem}^{dry} D_T^{chem} \Gamma \frac{\partial \lambda}{\partial x^{dry}} \tag{II.19}$$

where D_T^{chem} is the chemical thermal-dependent diffusion coefficient (Ferrara, Polverino, and Pianese 2018), calculable as follows:

$$D_T^{chem} = 0.265 \cdot 10^{-4} \exp\left(-\frac{3343}{T}\right) \tag{II.20}$$

II.1.5 The complete well-posed PDE problem

It is now possible to compose the final comprehensive PDE problem, exploding every term of the water balance shown in eq. (II.2) as function of water membrane content and simplifying common terms, as shown below:

$$\frac{\partial \lambda}{\partial t} + (1 + \beta\lambda) \frac{\partial}{\partial x^{dry}} \left(u_{EOD} \lambda + \frac{u_{conv}^{dry}}{(1 + \beta\lambda)^2} \lambda - D_T^{chem} \Gamma(\lambda) \frac{\partial \lambda}{\partial x^{dry}} \right) = 0 \tag{II.21}$$

The presented PDE problem can be closed with boundary conditions and initial condition:

$$\begin{cases} \lambda(0, t) = \lambda_a(t) \\ \lambda\left(L_{mem}^{dry}, t\right) = \lambda_c(t) \\ \lambda\left(x^{dry}, t\right) = \lambda_0\left(x^{dry}\right) \end{cases} \tag{II.22}$$

The well-posed PDE problem presented in this section is a complete description of water transport mechanisms inside the membrane, derived from literature: the solution of this problem can be found only with numerical resolution algorithms.

II.2 Numerical resolution of the PDE problem

The well-posed PDE problem is highly non-linear; hence, it can't be solved by means of PDEs solving techniques. In this section, a numerical algorithm is proposed to calculate a numerical solution to the problem, both in steady-state and transient conditions.

II.2.1 Steady-state solution

The relative steady-state boundary values problem is here shown:

$$\begin{cases} \dfrac{d}{dx^{dry}}\left(u_{EOD}\lambda + \dfrac{u_{conv}^{dry}}{(1+\beta\lambda)^2}\lambda - D_T^{chem}\Gamma(\lambda)\dfrac{d\lambda}{dx^{dry}}\right) = 0 \\ \lambda(0) = \lambda_a \\ \lambda\left(L_{mem}^{dry}\right) = \lambda_c \end{cases} \tag{II.23}$$

The stencil considered is defined over an uniform grid, with constant spacing equal to Δx^{dry}. A second-order accuracy scheme is chosen to be implemented, to preserve a balanced accuracy between first- and second-order derivatives: a staggered stencil is then considered, with the schematisation shown in Figure II.2.

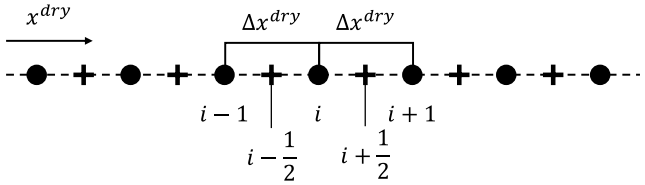


Figure II.2 *Grid stencil considered for steady-state numerical resolution.*

A distinction between advection fluxes, i.e., electro-osmotic drag and convection, and diffusive flux is needed in the numerical discretization. The advective flux terms can be discretized with a central finite differences approach

with second-order accuracy as follows:

$$\frac{d}{dx^{dry}}\left(u_{EOD}\lambda + \frac{u_{conv}^{dry}}{(1+\beta\lambda)^2}\lambda\right) \approx$$
$$u_{EOD}\frac{\lambda_{i+1}-\lambda_{i-1}}{2\Delta x^{dry}} + u_{conv}^{dry}\frac{\frac{\lambda_{i+1}}{(1+\beta\lambda_{i+1})^2} - \frac{\lambda_{i-1}}{(1+\beta\lambda_{i-1})^2}}{2\Delta x^{dry}} \tag{II.24}$$

About the diffusive flux, the midpoint integration scheme has to be applied due to the presence of the Γ function, interpolating the midpoint with a linear approximation:

$$\frac{d}{dx^{dry}}\left(-D_T^{chem}\Gamma(\lambda)\frac{d\lambda}{dx^{dry}}\right) \approx$$
$$-D_T^{chem}\frac{1}{\Delta x^{dry}}\left(\frac{\Gamma_{i+1}+\Gamma_i}{2}\frac{\lambda_{i+1}-\lambda_i}{\Delta x^{dry}} - \frac{\Gamma_i+\Gamma_{i-1}}{2}\frac{\lambda_i-\lambda_{i-1}}{\Delta x^{dry}}\right) \tag{II.25}$$

The implementation of the discretised balance equation leads to a system of non-linear equations to be solved with numerical methods. The Newton-Rhapson method is chosen as numerical solving algorithm, thanks to its fast convergence and solution stability. The following non-linear problem has to be solved:

$$\mathbf{f}(\boldsymbol{\lambda}) = \mathbf{0} \tag{II.26}$$

where $\mathbf{f}$ is the residual of the discretized steady-state boundary values differential equation, calculated all over $\boldsymbol{\lambda}$ grid except at boundaries. According to Newton-Rhapson method, the solution has to be iteratively updated:

$$\boldsymbol{\lambda}^{k+1} = \boldsymbol{\lambda}^k + \alpha\boldsymbol{\Delta\lambda}^k \tag{II.27}$$

where α is a relaxing factor to avoid numerical instabilities, while the update $\boldsymbol{\Delta\lambda}^k$ is calculated from the function Jacobian matrix:

$$\boldsymbol{\Delta\lambda}^k = -\mathbf{J}\left(\boldsymbol{\lambda}^k\right)^{-1}\cdot\mathbf{f}\left(\boldsymbol{\lambda}^k\right) \tag{II.28}$$

According to the numerical discretization of the three flux terms introduced before, the Jacobian matrix is a tri-diagonal matrix built as follows:

$$\mathbf{J}\left(\boldsymbol{\lambda}^k\right) = \begin{bmatrix} \ddots & \ddots & \ddots & & \\ & \frac{\partial f}{\partial\lambda_{i-1}} & \frac{\partial f}{\partial\lambda_i} & \frac{\partial f}{\partial\lambda_{i+1}} & \\ & & \ddots & \ddots & \ddots \end{bmatrix} \tag{II.29}$$

where the partial derivatives $\frac{\partial f}{\partial \lambda}$ are easily calculable from the discretised problem.

A grid convergence analysis is firstly conducted to define the optimal number of grid points in terms of computational time without losing the solution accuracy. The parameter chosen to conduct the grid convergence analysis is the average water membrane content, calculated as the trapezoidal integral of the numerical solution:

$$\bar{\lambda} = \frac{1}{L_{mem}^{dry}} \sum_{i=1}^{N-1} \frac{\lambda_{i+1} + \lambda_i}{2} \Delta x^{dry} \tag{II.30}$$

where N is the total number of points of the discretised grid. In Table II.1, the operative conditions and membrane features are considered for the convergence analysis:

Table II.1 *Operative conditions and membrane physical features dataset for the steady-state solution numerical convergence analysis*

Description of the variable	**Symbol**	**Value (Units)**
Dry membrane molar concentration	c_{mem}^{dry}	1800 (mol/m^3)
Dry membrane thickness	L_{mem}^{dry}	100 (μm)
Membrane water permeability	k_w	$1 \cdot 10^{-18}$ (m^2)
Current density	i	0.5 (A/cm^2)
Temperature	T	20 (°C)
Cathode pressure	p_c	1 (bar)
Anode pressure	p_a	1.5 (bar)
Anode water content boundary condition	λ_a	7 (−)
Cathode water content boundary condition	λ_c	14 (−)

The results of the convergence analysis are shown in Figure II.3: the blue line with circles represents the average water membrane content for each grid points number at left axis, while the red line with squares is referred to computational time, to be read on the logarithmic scale of right axis.

A final configuration of 256 points grid is chosen, ensuring fast computational time with a final error with respect to the finest grid of 2048 points of $1 \cdot 10^{-4}$%. The steady-state solution of the proposed boundary values differential equation, in same configuration set of Table II.1, is graphed in Figure II.4.

Analysing the result, the water content profile is non-linear, highlighting a non-uniform water distribution across the membrane coherently with the advection-diffusion nature of the physical problem. This solution shape paves

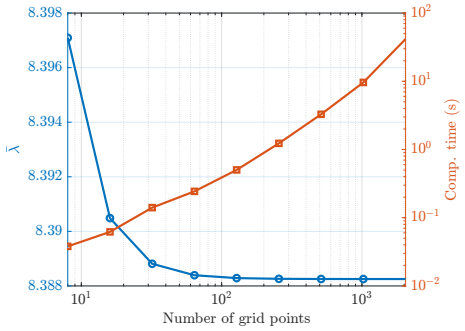


Figure II.3 *Grid convergence analysis results: average water membrane content (left axis, blue); computational time (right axis, red).*

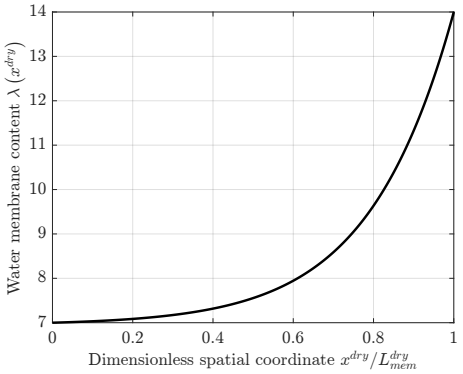


Figure II.4 *Water membrane content steady state solution with respect to normalised dry thickness, with Table II.1 as dataset.*

the way for the introduction of the simplification attempt, which is shown in the proper section. In Figure II.5 the water molar fluxes are shown, with every colour corresponding to a different flux according to the legend.

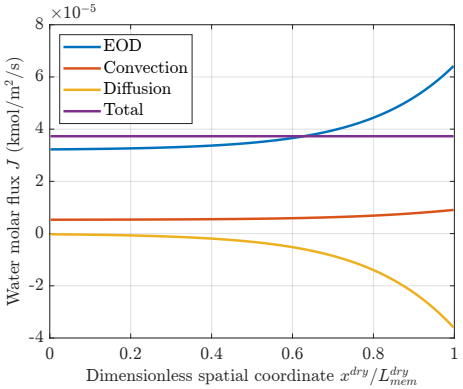


Figure II.5 *Water molar fluxes steady state solution with respect to normalised dry thickness, with Table II.1 as dataset.*

The main observation is that the net water molar flux is perfectly flat across the membrane, confirming the goodness and physical consistency of the solution. To further validate the obtained steady-state solution, the results in terms of membrane average conductivity and net water molar flux are calculated parametrising boundary conditions, similarly to what done by Mazumder (2005). In Table II.2, the dataset used for the parametric analysis extracted from the literature paper as reference is reported.

Table II.2 *Operative conditions and membrane physical features dataset for the steady-state solution numerical literature validation.*

Description of the variable	**Symbol**	**Value (Units)**
Dry membrane molar concentration	c_{mem}^{dry}	1800 (mol/m^3)
Dry membrane thickness	L_{mem}^{dry}	175 (μm)
Membrane water permeability	k_w	$1.6 \cdot 10^{-18}$ (m^2)
Current density	i	0.5 (A/cm^2)
Temperature	T	30 (°C)
Cathode pressure	p_c	3 (bar)
Anode pressure	p_a	1 (bar)
Anode water content boundary condition	λ_a	4:15 (−)
Cathode water content boundary condition	λ_c	4:15 (−)

The membrane average conductivity is calculated applying the relationship

identified by Springer, T. A. Zawodzinski, and Gottesfeld (1991):

$$\sigma = \left(0.005139\bar{\lambda} - 0.00326\right) \exp\left(1268\left(\frac{1}{303} - \frac{1}{T}\right)\right) \tag{II.31}$$

The average net water molar flux, on the other hand, is calculated similarly to the average membrane water content. In Figure II.6, the contour plot of membrane average conductivity is reported.

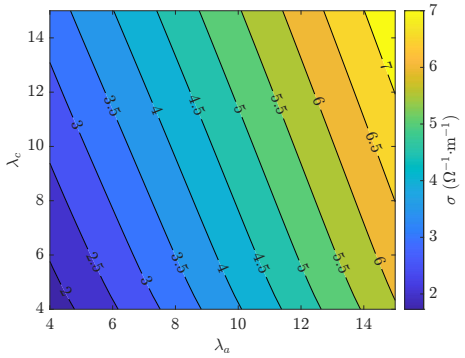


Figure II.6 *Membrane average conductivity as function of boundary conditions, with Table II.2 as dataset.*

The results in terms of order of magnitude and trend are coherent with what found by the author. In Figure II.7, the contour plot of membrane average net water molar flux is reported.

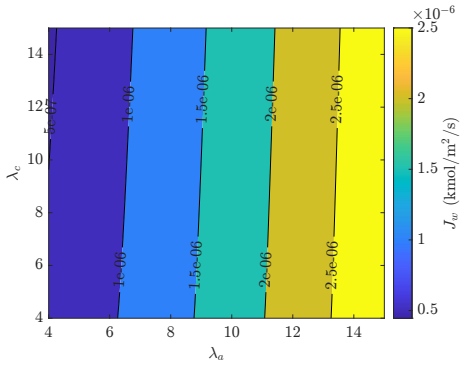


Figure II.7 *Membrane average net water molar flux as function of boundary conditions, with Table II.2 as dataset.*

Similar considerations can be performed looking at the average net water molar flux. However, there are some differences in fluxes definitions. First of all, the author defines the electro-osmotic drag as only function of water

membrane content, while in this proposed formulation there is also a thermal influence; furthermore, the diffusion coefficient is defined differently, since the author relies on the diffusion coefficient identified by Springer, T. A. Zawodzinski, and Gottesfeld (1991).

II.2.2 Transient solution

The PDE presented before can be collected together with boundary conditions and initial condition, forming the following well-posed closed system:

$$\begin{cases} \frac{\partial \lambda}{\partial t} + (1+\beta\lambda)\frac{\partial}{\partial x^{dry}}\left(u_{EOD}\lambda + \frac{u_{conv}^{dry}}{(1+\beta\lambda)^2}\lambda - D_T^{chem}\Gamma(\lambda)\frac{\partial \lambda}{\partial x^{dry}}\right) = 0 \\ \lambda(0,t) = \lambda_a \\ \lambda\left(L_{mem}^{dry}, t\right) = \lambda_c \\ \lambda\left(x^{dry}, 0\right) = \lambda_a + (\lambda_c - \lambda_a)\frac{x^{dry}}{L_{mem}^{dry}} \end{cases} \tag{II.32}$$

This equation systems is relative to a dynamic advection-diffusion problem, in which the inertial term is also proportional to the state variable λ due to the presence of the pre-multiplication factor $1+\beta\lambda$. In order to separate the effects, constant boundary conditions are considered, with a linear initial solution to the problem consistent with the boundaries. To solve this system, the explicit Runge-Kutta 4th order scheme is implemented to keep implementation easiness, good computational time, and high temporal accuracy. Applying the spatial discretisation introduced in the steady-state solution solver, the corresponding numerical scheme is the following:

$$\begin{aligned} \frac{d\lambda_i}{dt} = -\frac{1+\beta\lambda_i}{\Delta x^{dry}}\Bigg(& u_{EOD}\frac{\lambda_{i+1}-\lambda_{i-1}}{2} + u_{conv}^{dry}\frac{\frac{\lambda_{i+1}}{(1+\beta\lambda_{i+1})^2} - \frac{\lambda_{i-1}}{(1+\beta\lambda_{i-1})^2}}{2} + \\ & - \frac{D_T^{chem}}{\Delta x^{dry}}\frac{(\Gamma_{i+1}+\Gamma_i)(\lambda_{i+1}-\lambda_i) - (\Gamma_i+\Gamma_{i-1})(\lambda_i-\lambda_{i-1})}{2}\Bigg) \end{aligned} \tag{II.33}$$

For the following simulations, the spatial coordinate is divided into 2^6 elements, while a time step equal to 10^{-2} is chosen over a time span of 100 seconds: the choice of time step and spatial delta is critical to ensure numerical stability of the algorithm. The reference dataset used for the following results is the same as the steady-state solution calculation one, collected in Table II.1. In Figure II.8, the results obtained from the numerical algorithm are shown: the water membrane content distribution across the membrane is reported, with

every shade corresponding to a different time instant.

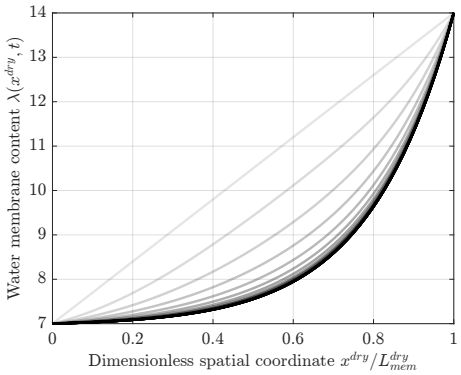


Figure II.8 *Water membrane content transient solution with respect to normalised dry thickness, with Table II.1 as dataset.*

The solution is consistent with the physical nature of the presented problem. The advective fluxes, i.e., electro-osmotic drag and convection, pushes water molecules in the cathode direction, hence, ”bending” the water distribution profile towards right; the diffusive flux, on the other hand, opposes to the water non-homogeneous distribution, leading to an equilibrium condition. The equilibrium is reached after a certain amount of time with an exponential decay-like temporal behaviour. This trend is further confirmed by looking at the average water membrane content over time, pictured in Figure II.9.

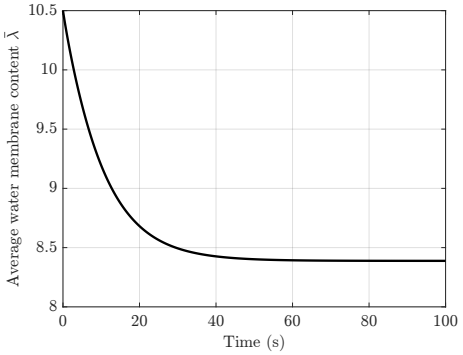


Figure II.9 *Average water membrane content transient solution evolving in time, with Table II.1 as dataset.*

In Figure II.10, the average water molar fluxes time evolutions are reported, with every colour corresponding to a different flux according to the legend.

Similar considerations can be made looking at water molar fluxes. After a first transient phase, in which the water fluxes distributes differently, a steady-

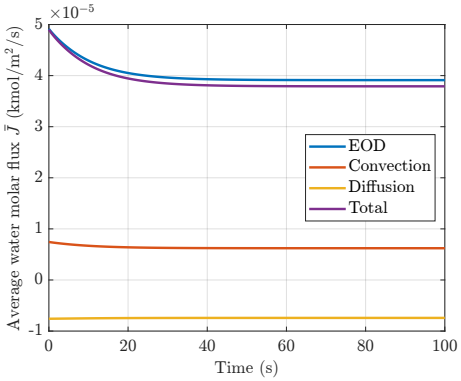


Figure II.10 *Average water molar fluxes transient solution evolving in time, with Table II.1 as dataset.*

state equilibrium is reached. Comparing the time needed for transient extinction between the average water membrane content and net water molar flux, it seems that the dynamic behaviour is comparable.

II.3 Analytical resolution of the linearised PDE problem

From the analysis of the numerical resolution, the following observations emerge: (i) the steady-state water content profile is similar to an exponential curve, due to the balance between advective and diffusive forces; (ii) the transient solution tends from the initial condition to steady-state solution with exponential-like decay. Based on these considerations, the linearisation of the PDE is proposed in order to obtain the analytical solution of the water membrane content problem.

II.3.1 Main assumptions and problem normalisation

Two different assumptions are proposed and here discussed. The first assumption regards the swelling effect: as stated by eq. (II.4), the swelling influence on the solution depends on the swelling factor s. Due to the low numerical value, one can neglect the effects on swelling behaviour on membrane solution, considering the membrane as fixed:

$$s \approx 0 \tag{II.34}$$

This simplification has consequences on inertial factor $1 + \beta\lambda$ and on convective transport as well. The second assumption can be derived looking at

Γ function behaviour from Figure II.1: this dimensionless function tends to a constant value for $\lambda > 5$. Hence, excluding conditions in which the water membrane content is lower than 5, it is possible to consider a fixed Γ value as follows:

$$\Gamma\left(\lambda > 5\right) \approx \Gamma^* = \frac{1}{5} \tag{II.35}$$

Combining the two proposed assumptions of eqs. (II.34) and (II.35) into the PDE problem of eq. (II.32), the following linear well-posed PDE problem is obtained:

$$\begin{cases} \frac{\partial \lambda}{\partial t} + \frac{\partial}{\partial x^{dry}}\left(\left(u_{EOD} + u_{conv}^{dry}\right)\lambda - D_T^{chem}\Gamma^* \frac{\partial \lambda}{\partial x^{dry}}\right) = 0 \\ \lambda\left(0, t\right) = \lambda_a \\ \lambda\left(L_{mem}^{dry}, t\right) = \lambda_c \\ \lambda\left(x^{dry}, 0\right) = \lambda_a + \left(\lambda_c - \lambda_a\right)\frac{x^{dry}}{L_{mem}^{dry}} \end{cases} \tag{II.36}$$

To generalise the mathematical discussion, the time and spatial coordinates can be made dimensionless:

$$dx^{dry} = L_{mem}^{dry} d\xi \tag{II.37}$$

$$dt = \frac{L_{mem}^{dry\ 2}}{D_T^{chem}\Gamma^*} d\tau \tag{II.38}$$

where ξ and τ are, respectively, the dimensionless spatial and temporal coordinates. In addition, the water membrane content can be normalised between boundary conditions:

$$a = \frac{\lambda - \lambda_a}{\lambda_c - \lambda_a} \tag{II.39}$$

Combining eqs. (II.37), (II.38), and (II.39) into the PDE problem of eq. (II.36) and simplifying common terms, the following dimensionless normalised PDE problem is formulated:

$$\begin{cases} \frac{\partial a}{\partial \tau} + \frac{\partial}{\partial \xi}\left(aPe - \frac{\partial a}{\partial \xi}\right) = 0 \\ a\left(0, \tau\right) = 0 \\ a\left(1, \tau\right) = 1 \\ a\left(\xi, 0\right) = \xi \end{cases} \tag{II.40}$$

where Pe is the Peclet number, a dimensionless constant that expresses the ratio between advection forces, i.e., electro-osmotic drag and convection, over

diffusion mechanism:

$$Pe = \frac{u_{EOD} + u_{conv}^{dry}}{u_{diff}} \tag{II.41}$$

where u_{diff} is the diffusive representative speed:

$$u_{diff} = \frac{D_T^{chem}\Gamma^*}{L_{mem}^{dry}} \tag{II.42}$$

II.3.2 Steady-state solution

The relative steady-state problem derived from eq. (II.40) is shown below.

$$\begin{cases} \frac{d}{d\xi}\left(a_s Pe - \frac{da_s}{d\xi}\right) = 0 \\ a_s\,(0) = 0 \\ a_s\,(1) = 1 \end{cases} \tag{II.43}$$

The solution of the linear ODE problem of eq. (II.43) is easily obtainable by means of differential equations solving techniques:

$$a_s\,(\xi) = \frac{e^{Pe\xi} - 1}{e^{Pe} - 1} \tag{II.44}$$

In Figure II.11, the normalised steady-state analytical solution is reported at different Pe values, with every colour corresponding to a different value according to the legend.

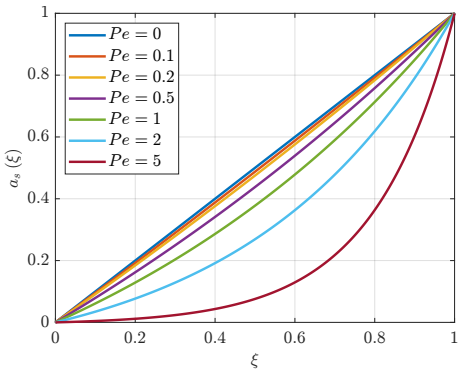


Figure II.11 *Normalised steady-state water membrane content calculated from linearised water problem, as function of Peclet number.*

Looking at the figure, the normalised solution already hints that severe Peclet

conditions, corresponding to operative conditions in which the advection forces are largely stronger than the diffusion, increasingly bend the water distribution towards the electrode with higher water content. The operative condition corresponding to $Pe = 0$ is referred to a pure diffusion condition, which can be obtained as the limit of eq. (II.44):

$$\lim_{Pe \to 0} a_s = \xi \tag{II.45}$$

The corresponding average normalised steady-state analytical water membrane content is obtained integrating the solution over the dimensionless coordinate ξ:

$$\bar{a}_s = \int_0^1 a_s\left(\xi\right) d\xi = \frac{1}{Pe} - \frac{1}{e^{Pe} - 1} \tag{II.46}$$

In Figure II.12, the average normalised steady-state analytical solution is reported for different Pe values up to 50.

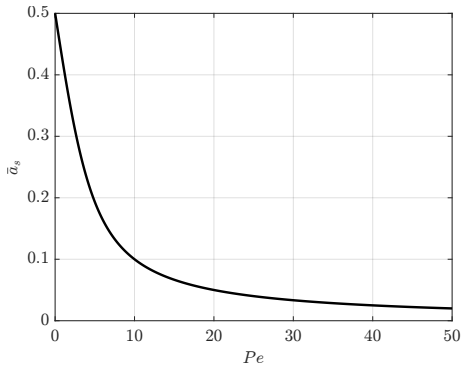


Figure II.12 *Normalised average steady-state water membrane content calculated from linearised water problem, as function of Peclet number.*

The Figure II.12 confirms that in high advection cases the water distribution is strongly pushed towards the moister electrode, with the average water content decreasing with Peclet number. The pure-diffusive condition is defined once again as the limit for Peclet tending to zero as follows:

$$\lim_{Pe \to 0} \bar{a}_s = \frac{1}{2} \tag{II.47}$$

Inverting the normalisation process, the steady-state analytical water membrane content can be calculated as follows:

$$\lambda_s = \lambda_a + \left(\lambda_c - \lambda_a\right) \frac{e^{Pe\,\xi} - 1}{e^{Pe} - 1} \tag{II.48}$$

The solution found is the same as the ones proposed in the works by Mazumder (2005) and Ferrara, Polverino, and Pianese (2018), reaffirming the consistency and robustness of the linearisation process proposed in this section. The average steady-state analytical water membrane content is defined below:

$$\bar{\lambda}_s = \lambda_a + (\lambda_c - \lambda_a)\left(\frac{1}{Pe} - \frac{1}{e^{Pe} - 1}\right) \tag{II.49}$$

With reference to the dataset collected in Table II.1, the analytical steady-state solution is compared to the numerical one obtained before in Figure II.13: the numerical solution is graphed with solid black line, while the analytical one defined in this section is shown with dashed black line.

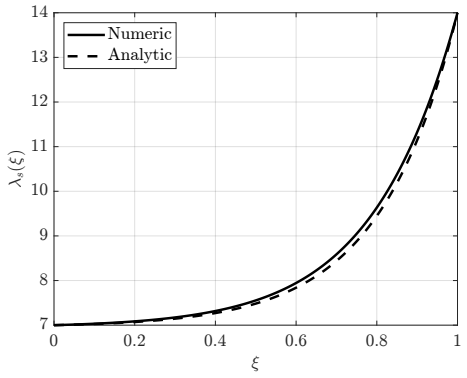


Figure II.13 *Comparison between numerical (solid line) and analytical (dashed line) steady state solutions, with Table II.1 as dataset.*

It can be seen that the analytical water membrane distribution is very close to the numerical one, confirming that the simplification hypotheses proposed before are acceptable, with minor effects on water distribution behaviour. The maximum deviation between the two profiles is roughly 2% of underestimation; the Root Mean Square Error (RMSE) is equal to 0.1405, corresponding to 1.25% of average numerical water membrane content. The correlation factor R^2 between the two profiles is equal to 0.9995, reaffirming the physical consistency and robustness of the analytical solution. In Figure II.14, the comparison between average numerical and steady state solutions are reported as function of Peclet number: the numerical solution is graphed with a solid line, while the analytical one is shown with a dashed line.

The comparison between averaged solutions still reaffirms the physical consistency of the analytical solution. The RMSE of the average analytical solution is 0.0089, with a correlation factor R^2 equal approximatively to 1. The two profiles show a maximum percent deviation of 0.28%.

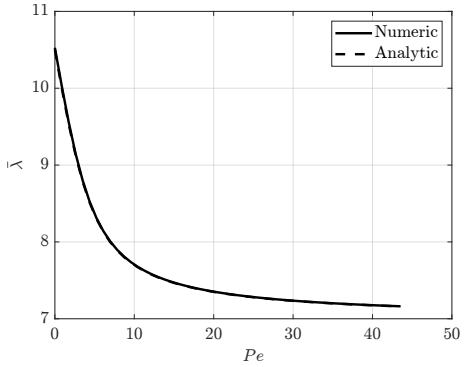


Figure II.14 *Comparison between average numerical (solid line) and analytical (dashed line) steady state solutions varying Peclet number, with Table II.1 as dataset.*

II.3.3 Transient solution

The solution to the well-posed linear PDE problem, shown in eq. (II.40), can be found by means of PDE solving techniques applying the superposition principle:

$$a\left(\xi,\tau\right)=a_s\left(\xi\right)+a_u\left(\xi,\tau\right) \tag{II.50}$$

where a_s is the same steady-state solution found with eq. (II.44), while the unsteady contribution a_u is defined applying the Fourier series expansion:

$$a_u\left(\xi,\tau\right)=\sum_{n=1}^{\infty}k_nX_n\left(\xi\right)T_n\left(\tau\right) \tag{II.51}$$

The spatial eigenfunctions are defined as follows:

$$X_n\left(\xi\right)=e^{\frac{Pe}{2}\xi}\sin\left(n\pi\xi\right) \tag{II.52}$$

As expected, every eigenfunction is proportional to a sine wave, according to Fourier series. The first five modes are depicted in Figure II.15: the first five modes are reported with different colours according to the legend, together with the envelope curves. To show the effect of operative conditions, it is considered Peclet equal to five, corresponding to a high advection case.

The temporal eigenfunctions are simple exponential decay functions, shown below:

$$T_n\left(\tau\right)=e^{-\frac{\tau}{\tau n}} \tag{II.53}$$

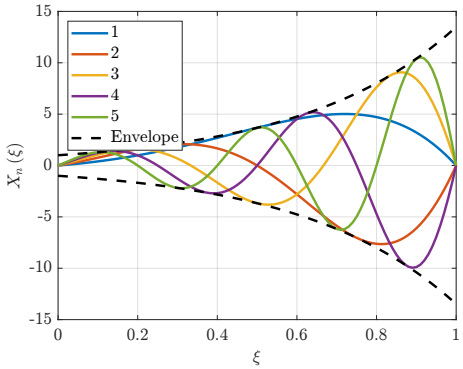


Figure II.15 *Representation of the first five spatial eigenfunctions, together with envelope curves, for* $Pe = 5$.

where τ_n is a characteristic time constant derived from eigenvalues as a function of Peclet number:

$$\tau_n = \frac{4}{Pe^2 + 4n^2\pi^2} \tag{II.54}$$

Coherently with Fourier series application, the eigenvalues decrease with mode number: higher modes have shorter time constants, hence, faster decay times. In Figure II.16, the time constants are represented based on mode number (x-axis) and several Peclet values (different colours, according to the legend).

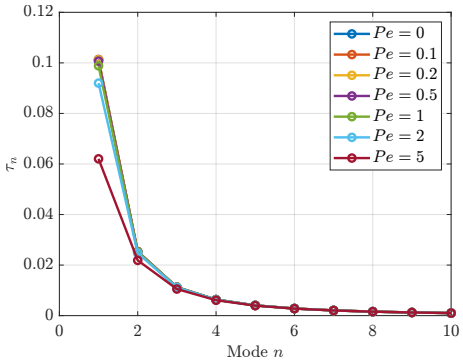


Figure II.16 *Representation of time constants for different modes as function of Peclet number.*

It can be observed that the operative conditions, expressed by the magnitude of Pe, have a direct influence on unsteady behaviour decay time: advection forces tend to move water molecules faster than the diffusion, speeding up the

solution decaying process with higher Peclet values. The pure diffusive case, in which $Pe = 0$, is the slowest case.

The integration constants k_n are defined from the coupling of initial condition and steady-state solution applying the orthogonality principle of trigonometric functions:

$$k_n = 2 \int_0^1 \left(a_0(\xi) - a_s\left(\xi\right)\right) e^{-\frac{Pe}{2}\xi} \sin\left(n\pi\xi\right) d\xi \tag{II.55}$$

The integration constants are specific to the initial condition of the problem. Considering the pure diffusive solution as initial condition, in Figure II.17 the values of integration costants are reported as function both of mode numbers (x-axis) and Peclet values (different line colours, according to legend).

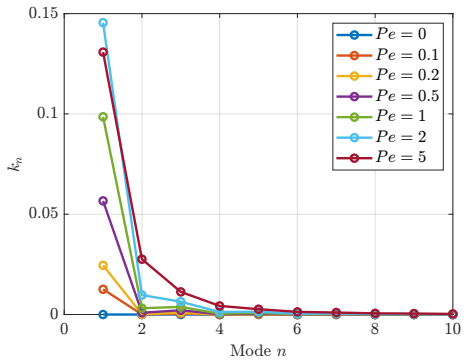
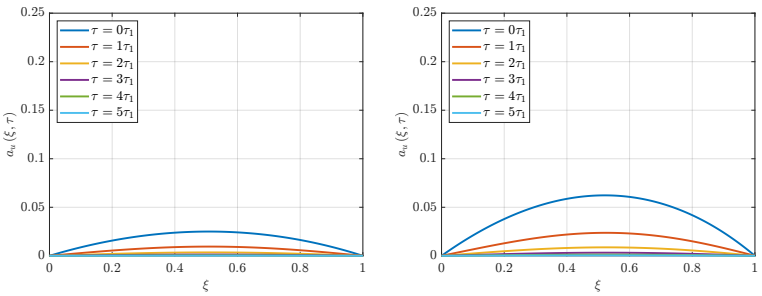


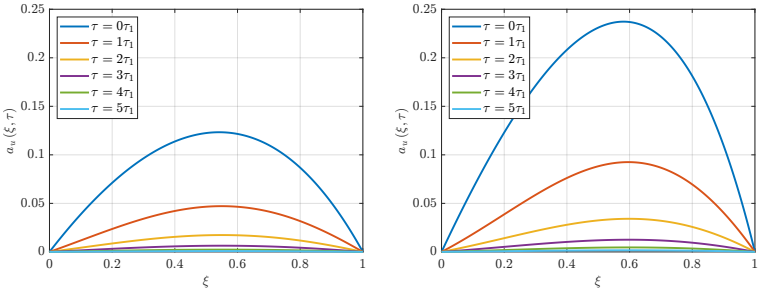
Figure II.17 *Representation of integration constants for different modes as function of Peclet number, considering a pure diffusive initial condition.*

From the results, it can be noted that the first mode always has the greater integration constants, independently from Peclet value. Combining all the components of the unsteady part, in Figure II.18 the unsteady normalised water membrane content is depicted in four different Peclet values. Every line colour corresponds to a different τ dimensionless time, defined as integer multiple of the first eigenvalue τ_1 from eq. (II.54).

The first consideration is about the magnitude of the unsteady solution: it can be noted that higher Peclet values correspond to higher unsteady amount, since the steady-state solution to be reached gets increasingly bent. In addition, the unsteady solution peak shifts towards right as Peclet increases. The second consideration is about the τ_1 used as time reference: since the exponential decays are function of Pe as stated by eqs. (II.54) and (II.53), the first eigenvalue calculated for each Pe value is chosen as reference time for every simulation, reporting the integers from 0 to 5 corresponding to 99.3% exponential extinction. Combining the steady-state solution of eq. (II.44) with the



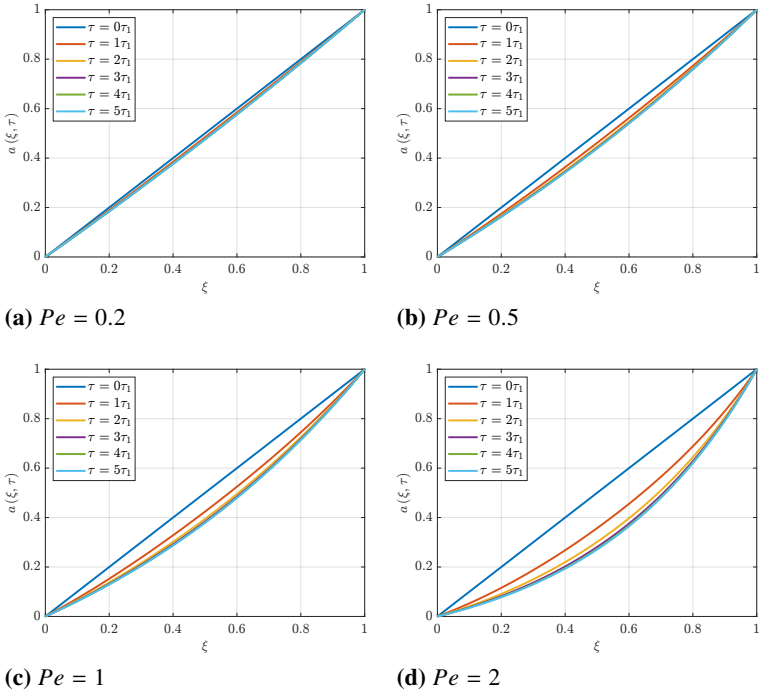
(a) $Pe = 0.2$ **(b)** $Pe = 0.5$



(c) $Pe = 1$ **(d)** $Pe = 2$

Figure II.18 *Normalised unsteady water membrane content calculated from linearised water problem, as function of Peclet number, space, and time.*

unsteady contribution of eq. (II.51), the final complete linearised normalised water membrane content solution is reported in Figure II.19, for the same Peclet values as Figure II.18.



(a) $Pe = 0.2$ **(b)** $Pe = 0.5$

(c) $Pe = 1$ **(d)** $Pe = 2$

Figure II.19 *Normalised water membrane content calculated from linearised water problem, as function of Peclet number, space, and time.*

From the analysis of the normalised solution, one main observation can be made. The Peclet number shows a direct influence on both the steady-state solution shape bending and temporal dynamics, meaning that operative conditions with strong advection forces are critical from both water distribution and membrane dynamics perspectives.

The last mathematical effort regards the average quantity. Applying the superposition principle, the average normalised water membrane content can be calculated as follows:

$$\bar{a}(\tau) = \int_0^1 a(\xi,\tau)\, d\xi = \bar{a}_s + \bar{a}_u(\tau) \tag{II.56}$$

where $\bar{a}_u(\tau)$ is the average unsteady contribution shown below:

$$\bar{a}_u = \sum_{n=1}^{\infty} k_n T_n(\tau) \int_0^1 X_n(\xi)\, d\xi = \sum_{n=1}^{\infty} k_n \bar{X}_n T_n(\tau) \tag{II.57}$$

The average eigenfunction $\bar{X}_n$ is obtained integrating the eigenfunction X_n over the ξ coordinate as follows:

$$\bar{X}_n = \int_0^1 X_n(\xi)\, d\xi = \frac{4n\pi\left(1-(-1)^n e^{\frac{Pe}{2}}\right)}{Pe^2+4n^2\pi^2} \tag{II.58}$$

The average normalised water membrane content, derived from the discussed linearised PDE problem, is shown for different Peclet values in Figure II.20.

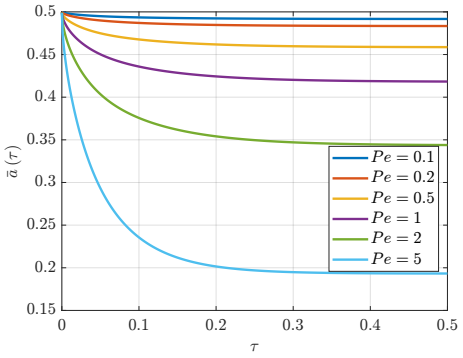


Figure II.20 *Normalised average water membrane content calculated from linearised water problem, as function of Peclet number.*

The results confirm that two phenomena happens corresponding to a Peclet increase: (i) reduction of average steady-state value; (ii) increase in transient decay speed. Hence, when advection forces are strong, for example, in case of high power request with high current, the membrane tends to get rapidly dryer on average, with non-uniform water distribution inside requiring precise water management control strategies.

II.3.4 Comparison with the numerical solution

To validate the results between numerical resolution and linearised analytical results, the proposed solution is tested within the dataset of Table II.1. In Figure II.21, the comparison between numerical solution, reported with solid lines, and analytical solution, reported with dashed lines, is depicted, with every colour corresponding to a different time instant according to the legend.

It can be noted that the physical consistency of the proposed linearised problem is fully kept during the simulation: the analytical solution tends to the steady-state condition within the same time needed for the numerical one. As also noted before, the two steady-state conditions show a negligible deviation

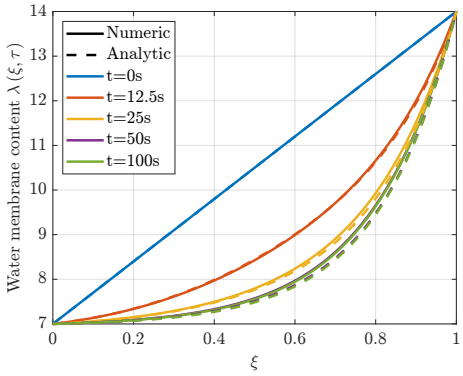


Figure II.21 *Comparison between numerical (solid line) and analytical (dashed line) solutions, with Table II.1.*

due to the assumptions needed for the linearisation process. In Figure II.22, the comparison between average dynamic solutions is reported: the numeric average water membrane content is depicted with solid line, while the analytical one is shown with dashed line.

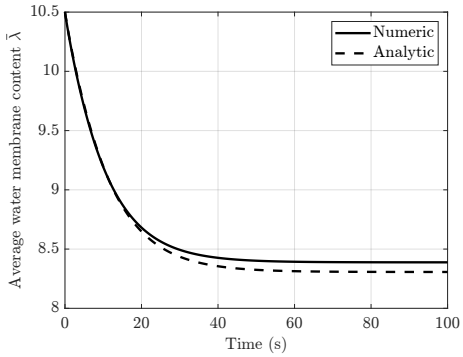


Figure II.22 *Comparison between average numerical (solid line) and analytical (dashed line) solutions over time, with Table II.1 as dataset.*

As expected, the two profiles share similar exponential decay dynamics, with the analytical average steady-state condition slightly lower than the numerical one. The maximum deviation between the two average solutions is 0.97% underestimation, while the RMSE is equal to 0.067. The correlation factor R^2 is equal to 0.9996, reaffirming the physical coherence of the proposed linearised problem. The mathematical effort needed for these steps is necessary to identify directly the average water membrane content, which is required for the characterisation of the membrane's Ohmic resistance.

II.4 Application of the integral method

In the previous sections, the membrane water balance problem is solved using two different approaches. In the first approach, the membrane water balance is solved as it is with numerical algorithms to understand the water distribution behaviour when sudden variations in operating conditions occur. In the successive step, the introduced PDE is linearised under rigorous assumptions in order to define an analytical solution that best captures the physical behaviour of the membrane water profile, finding the functional dependencies of membrane dynamics with respect to physical features and operative conditions. The problem with the two aforementioned approaches is that the proposed algorithms are not implementable. It is not feasible to implement the numerical algorithm in on-board controllers and virtual sensors, since a high computational burden would be required to improve solution quality, along with numerical precautions to preserve numerical stability. The analytical solution, even if it is based on solid physical background with no problems on grid definition and computational burden, is highly specific to a certain configuration of membrane parameters, operating conditions, and boundary conditions as well, making it not generalisable for on-board purposes. Hence, the integral method proposed in this section extracts from the analytical solution, validated on numerical results, the physical essence of the average water membrane content with the main objective of algorithm implementability and generalisability.

II.4.1 Integral solution identification

Analysing both numerical and analytical solutions, since the water balance problem is based on the mass conservation law, the water membrane profile exhibits an exponential decay-like dynamic from the initial condition to the steady-state solution. Hence, it is possible to define an arbitrary function that best approximates this behaviour on average, since the direct calculation of the average water membrane content is the objective of this work. The proposed solution for the normalised water membrane content is the following:

$$\begin{aligned} a^{*}(\xi,\tau) = a_0(\xi)\, f(\tau) + a_s(\xi)\,(1 - f(\tau)) = \\ a_s(\xi) + f(\tau)\,(a_0(\xi) - a_s(\xi)) \end{aligned} \tag{II.59}$$

where $f(\tau)$ is an unknown function to be identified. The proposed function correctly respects the boundary conditions:

$$a^{*}(0,\tau) = a_0(0)\, f(\tau) + a_s(0)\,(1 - f(\tau)) = 0 \tag{II.60}$$

$$a^{*}(1,\tau) = a_0(1)\, f(\tau) + a_s(1)\,(1 - f(\tau)) = 1 \tag{II.61}$$

The proposed solution main approximation is that every point of the water distribution has the same instantaneous dynamic. To identify the time function according to the integral method, the proposed solution has to respect the spatial integral average of the linearised PDE problem of eq. (II.40) as follows:

$$\frac{d}{d\tau}\int_0^1 a^*(\xi,\tau)\,d\xi+(a^*(1,\tau)-a^*(0,\tau))\,Pe-\left(\frac{\partial a^*}{\partial \xi}(1,\tau)-\frac{\partial a^*}{\partial \xi}(0,\tau)\right)=0 \tag{II.62}$$

Substituting and simplifying the common terms, the following linear ODE is obtained:

$$\frac{df}{d\tau}+f\frac{2Pe^2\left(e^{Pe}-1\right)}{e^{Pe}Pe-2e^{Pe}+2+Pe}=0 \tag{II.63}$$

The initial condition needed to completely define the new ODE problem can be obtained from the PDE's initial condition:

$$a^*(\xi,0)=\xi \;\rightarrow\; f(0)=1 \tag{II.64}$$

Finally, the following Cauchy linear problem is defined and it can be solved by means of ODE solving techniques:

$$\begin{cases} \dfrac{df}{d\tau}+\dfrac{f}{\tau_d}=0 \\ f(0)=1 \end{cases} \tag{II.65}$$

where τ_d is a dimensionless characteristic time constant, defined as follows:

$$\tau_d=\frac{e^{Pe}Pe-2e^{Pe}+Pe+2}{2Pe^2\left(e^{Pe}-1\right)} \tag{II.66}$$

In Figure II.23, the characteristic time constant trend with respect to Peclet number is shown.

It can be observed that the time function is a function of the operative conditions as expected: higher advection conditions correspond to faster dynamics. The pure diffusive condition is obtained calculating the limit:

$$\lim_{Pe\to 0}\tau_d=\frac{1}{12} \tag{II.67}$$

The mathematical solution to this linear ODE problem is trivial:

$$f(\tau)=e^{-\frac{\tau}{\tau_d}} \tag{II.68}$$

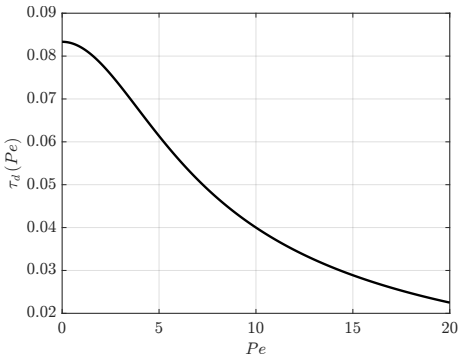


Figure II.23 *Dimensionless characteristic time constant as function of Peclet number.*

Analysing the obtained solution, the decay is exactly exponential, with steady-state condition reaching as time passes by. In Figure II.24, the comparison between analytical and integral solutions is reported for a given Peclet numbers set: every colour corresponds to a certain time instant as integer multiple of the characteristic time τ_1 with eq. (II.54) chosen as reference, according to the legend.

The integral solution shows higher deviations in first time instants, when the analytical solution is not able to keep the exponential shape across the membrane; the gap is then recovered and closed when the steady-state conditions are reached. This behaviour is similar also for the average solution, shown below:

$$\bar{a}^* (\tau) = \bar{a}_s + f (\tau) (\bar{a}_0 - \bar{a}_s) \tag{II.69}$$

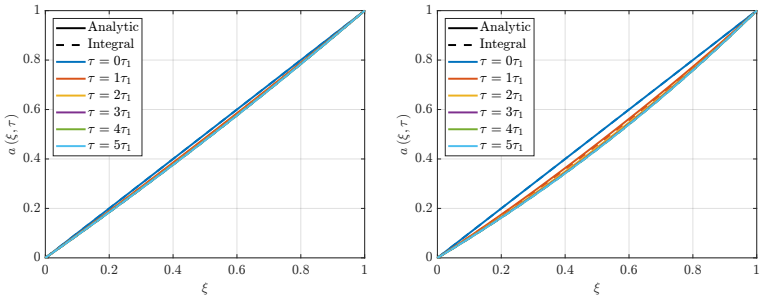
This type of behaviour is also confirmed looking at average solutions, shown in Figure II.25: the comparison between average solutions is reported, with different Peclet values according to the legend.

It is also possible to analytically evaluate the deviation error trend between the two average solutions based on Peclet number. The percent error function depending on time and Peclet is the following:

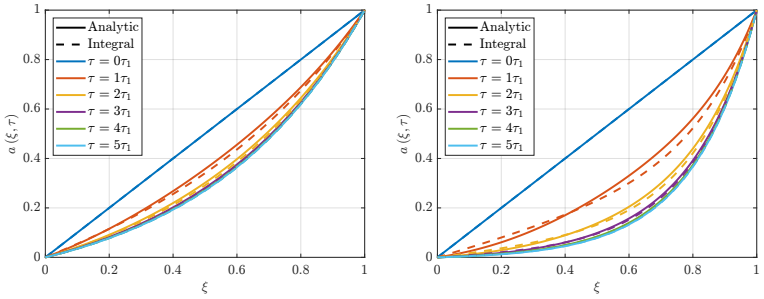
$$\varepsilon_{\%} (Pe, \tau) = \frac{\bar{a}^* (Pe, \tau) - \bar{a} (Pe, \tau)}{\bar{a} (Pe, \tau)} \cdot 100 \tag{II.70}$$

The percent error function is shown in Figure II.26 as coloured contour map.

Analysing the error function, two main considerations can be made. First of all, the average integral solution shifts from underestimation to overestimation of the average analytical solution with Peclet, meaning that the approximation error indefinitely increases with the advection forces; however, it is generally



(a) $Pe = 0.2$ **(b)** $Pe = 0.5$



(c) $Pe = 2$ **(d)** $Pe = 5$

Figure II.24 *Comparison between analytical (solid lines) and integral (dashed lines) solutions as function of Peclet number, space, and time.*

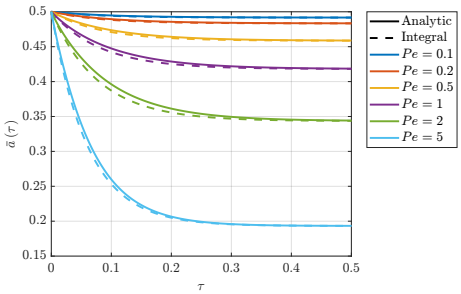


Figure II.25 *Comparison between analytical (solid lines) and integral (dashed lines) average solutions as function of time, varying Peclet.*

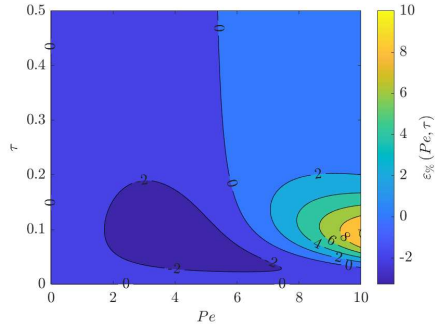


Figure II.26 *Error map between average analytical and integral solutions, as function of Peclet number and dimensionless time.*

difficult to achieve operative conditions with Peclet values higher than 5÷10. The second consideration is that, no matter the Peclet number value, the maximum deviation between the two solutions occurs only in the initial time instants, and it is fully recovered towards the steady-state conditions.

II.4.2 Validation of the proposed integral solution

To validate the integral solution, a first comparison between numeric, analytical, and integral results is performed. The integral solution is finally defined as follows:

$$\lambda^* (\xi, t) = \lambda_a + (\lambda_c - \lambda_a)\, a^* (\xi, t) \tag{II.71}$$

The corresponding average integral solution is simply the following:

$$\bar{\lambda}^* (t) = \lambda_a + (\lambda_c - \lambda_a)\, \bar{a}^* (t) \tag{II.72}$$

Finally, the characteristic time is obtained from the dimensionless version of eq. (II.66):

$$t_d = \frac{L_{mem}^{dry^2}}{D_T^{chem} \Gamma^*} \tau_d \tag{II.73}$$

The three solutions are obtained based on the dataset collected in Table II.1. In Figure II.27, the three solutions are compared: according to the legend, several time instants are reported on the figure based on line colour, while different markers are used to identify the three algorithms.

As it can be seen, the analytical solution is the closest to the numerical

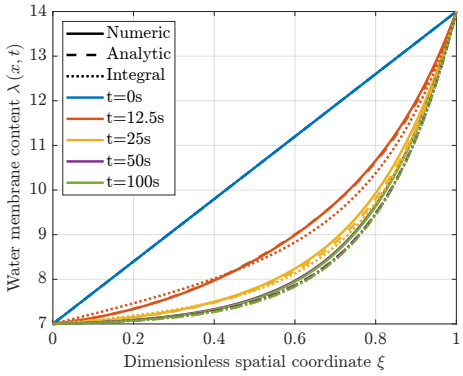


Figure II.27 *Comparison between numeric (solid lines), analytic (dashed lines), and integral (dotted lines) water membrane content distributions at different time instants, with Table II.1 as dataset.*

one, taken as reference, during the initial time instants. The integral method contemplates a water distribution slightly different from reference, with both overestimation and underestimation. However, as time passes by, the integral and analytical solutions converge to the same steady-state condition, with a little gap on average with respect to the numerical one. In Figure II.28, the three average solutions are compared in time: a solid line is used to represent the numerical solution, while dashed and dotted lines are, respectively, for analytical and integral ones.

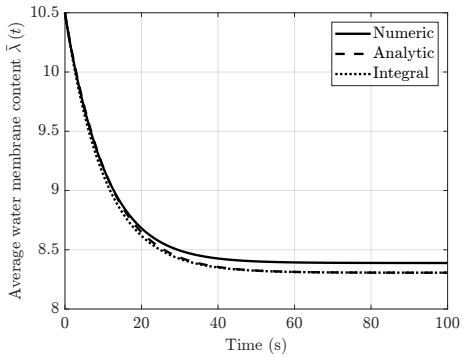


Figure II.28 *Comparison between average numeric (solid lines), analytic (dashed lines), and integral (dotted lines) water membrane content distributions, with Table II.1 as dataset.*

The three average solutions exhibit similar dynamics, reaffirming the physical consistency of the exponential decay assumption made applying the integral method. The final gap between average steady-state conditions is about 0.97%

underestimation. The RMSE of the analytical solution with respect to the numerical one is 0.0674, with a correlation factor R^2 equal to 0.9996; the integral solution performs worse on average, with RMSE equal to 0.0739, but with higher correlation up to 0.9999.

To better understand the integral solution performance with respect to numerical reference in terms of mean error and its standard deviation, the following parametric analyses are here proposed. The first parametric analysis is for the operative conditions, while the second analysis contemplates boundaries parametrisation; in Table II.3, the dataset for the following simulations is reported.

Table II.3 *Membrane physical features and operative conditions dataset for the integral solution parametric analysis.*

Description of the variable	**Symbol**	**Value (Units)**
Dry membrane molar concentration	c_{mem}^{dry}	1800 (mol/m^3)
Dry membrane thickness	L_{mem}^{dry}	100 (μm)
Membrane water permeability	k_w	$1 \cdot 10^{-18}$ (m^2)
Current density	i	0:1 (A/cm^2)
Temperature	T	20:80 (°C)
Cathode pressure	p_c	1-1.5 (bar)
Anode pressure	p_a	1-1.5 (bar)
Anode water content boundary condition	λ_a	7:15 (−)
Cathode water content boundary condition	λ_c	7:15 (−)

In Figure II.29, the results in terms of mean percent error parametrising current density and temperature with negative pressure gradient are reported as contour map. The boundary conditions are kept fixed, with $\lambda_a = 7$ and $\lambda_c = 14$. The final time for the simulations is set equal to five times the characteristic time calculated from the integral method, to ensure the steady-state conditions reaching by numeric and integral solutions.

It can be observed that the integral method proposed a solution close to the one calculated with the numerical techniques, with a minimum conditions of -1.6% with low current and temperature. The gap between solution is recovered at high currents and temperature, inducing an overestimation. The error map shape changes significantly when the pressure gradient is positive, as shown in Figure II.30.

When the pressure gradient is positive, it opposes the electro-osmotic drag: in this condition, the integral method tends to overestimate the numerical solution in almost all the tested conditions. However, the mean percent error is still contained within 1.2%. In Figure II.29, the results in terms of mean

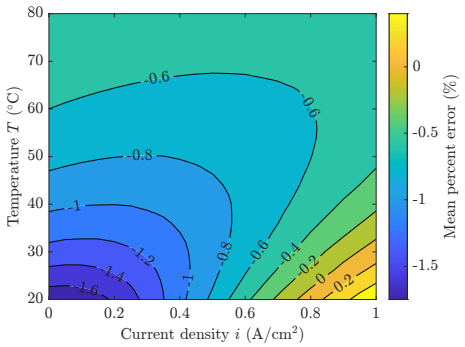


Figure II.29 *Mean percent error between average numerical and integral transient solutions as function of current density and temperature with negative pressure gradient, with Table II.3 as dataset.*

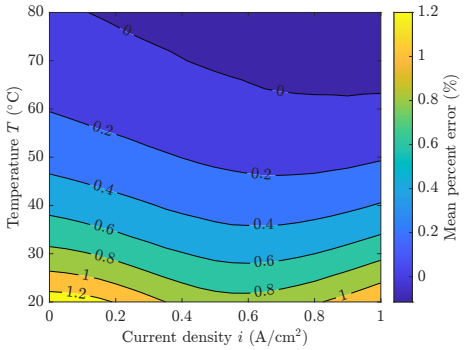


Figure II.30 *Mean percent error between average numerical and integral transient solutions as function of current density and temperature with positive pressure gradient, with Table II.3 as dataset.*

percent error parametrising the boundary conditions are reported as contour map. The operative conditions are kept fixed, with $i = 0.5$ A/cm^2, $T = 30°$ C, and negative pressure gradient.

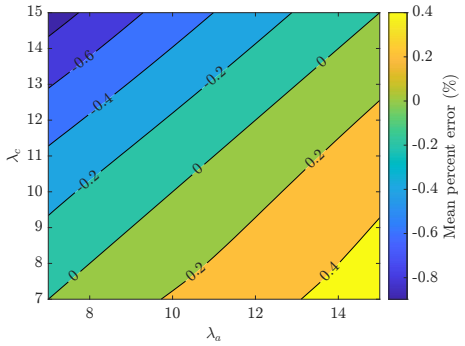


Figure II.31 *Mean percent error between average numerical and integral transient solutions as function of boundary conditions, with Table II.3 as dataset.*

The influence of boundary conditions is minor with respect to operating conditions weight, with the mean percent error within -0.8% and 0.4%. The integral solution slightly overestimates the numerical one in case of anode water content higher than cathode one and vice versa.

II.4.3 Net water molar fluxes integration

To complete the integral approach proposal, the net water molar fluxes exchanged between the membrane and the electrodes must be defined. Looking at the original PDE of eq. (II.32), it can be observed that the reason of water membrane content variation in time is the non-equilibrium of water fluxes involving the membrane; in addition, for simulation purposes only the fluxes at membrane boundaries are of interest. Starting from the linearised problem of eq. (II.36), the net water molar flux across the membrane is described by the following:

$$J_w(\xi,t) = c_{mem}^{dry} u_{diff} \left(\lambda(\xi,t)\, Pe - \frac{\partial \lambda}{\partial \xi}(\xi,t) \right) \tag{II.74}$$

In this case, the dimensionless dry spatial coordinate is directly considered for the sake of clarity. The water flux distribution can be specified at boundaries:

$$J_a(t) = J_w(0,t) = c_{mem}^{dry} u_{diff} \left(\lambda_a Pe - \frac{\partial \lambda}{\partial \xi}(0,t) \right) \tag{II.75}$$

$$J_c(t) = J_w(1,t) = c_{mem}^{dry} u_{diff} \left(\lambda_c Pe - \frac{\partial \lambda}{\partial \xi}(1,t) \right) \tag{II.76}$$

The main unknown is the time evolution of λ spatial gradient at boundaries. Since the main purpose is to directly identify the average water membrane content without necessarily defining the water distribution across the membrane, an alternative approximation of boundary water fluxes is here proposed. Starting from the steady-state solution of eq. (II.48), it is easy to calculate the solution profile tangent lines at boundaries as the first term of the Taylor expansion series:

$$\lambda_{left} = \lambda_a + (\lambda_c - \lambda_a) \frac{Pe}{e^{Pe} - 1} \xi \tag{II.77}$$

$$\lambda_{right} = \lambda_c - (\lambda_c - \lambda_a) Pe \frac{e^{Pe}}{e^{Pe} - 1} (1 - \xi) \tag{II.78}$$

The two tangent lines intersect at the following coordinates:

$$\begin{cases} \xi_s^{int} = \dfrac{e^{Pe} Pe - e^{Pe} + 1}{Pe \left(e^{Pe} - 1 \right)} \\ \lambda_s^{int} = \lambda_a + (\lambda_c - \lambda_a) \dfrac{e^{Pe} Pe - e^{Pe} + 1}{\left(e^{Pe} - 1 \right)^2} \end{cases} \tag{II.79}$$

It can be assumed that the intersection point defined by eq. (II.79), since it is directly derived by the water content profile, has the time dynamics of the solution itself. Assuming the same dynamic behaviour introduced by the integral method with the characteristic time t_d, it is possible to define the intersection coordinates as new dynamic states with the following dynamics:

$$\xi^{int}(t) = \xi_s^{int} + f(t) \left(\xi_0^{int} - \xi_s^{int} \right) \tag{II.80}$$

$$\lambda^{int}(t) = \lambda_s^{int} + f(t) \left(\lambda_0^{int} - \lambda_s^{int} \right) \tag{II.81}$$

where $f(t)$ is the dimensional version of time rensponse function of eq. (II.68). The intersection point of coordinates $\left(\xi_s^{int}, \lambda_s^{int} \right)$ can be then used to directly calculate the water gradient specified at boundaries:

$$\frac{\partial \lambda}{\partial \xi}(0,t) = \frac{\lambda^{int} - \lambda_a}{\xi^{int}} \tag{II.82}$$

$$\frac{\partial \lambda}{\partial \xi}(1,t) = \frac{\lambda_c - \lambda^{int}}{1 - \xi^{int}} \tag{II.83}$$

Finally, the approximate version of boundary net water molar fluxes can be

calculated as follows:

$$\begin{cases} J_a^*(t) = c_{mem}^{dry} u_{diff} \left(\lambda_a Pe - \dfrac{\lambda^{int} - \lambda_a}{\xi^{int}} \right) \\ J_c^*(t) = c_{mem}^{dry} u_{diff} \left(\lambda_c Pe - \dfrac{\lambda_c - \lambda^{int}}{1 - \xi^{int}} \right) \end{cases} \tag{II.84}$$

II.4.4 Integral solution implementation algorithm

In the previous paragraphs, applying the integral method a good approximation of average water membrane content is defined together with boundary net water molar fluxes. It can be noted that eqs. (II.72), (II.80), and (II.81) are the solutions of the following ODEs:

$$\begin{cases} \dfrac{d\bar{\lambda}^*}{dt} = \dfrac{\bar{\lambda}_s - \bar{\lambda}^*}{t_d} \\ \bar{\lambda}^*(0) = \bar{\lambda}_0 \end{cases} \tag{II.85}$$

$$\begin{cases} \dfrac{d\xi^{int}}{dt} = \dfrac{\xi_s^{int} - \xi^{int}}{t_d} \\ \xi^{int}(0) = \xi_0^{int} \end{cases} \tag{II.86}$$

$$\begin{cases} \dfrac{d\lambda^{int}}{dt} = \dfrac{\lambda_s^{int} - \lambda^{int}}{t_d} \\ \lambda^{int}(0) = \lambda_0^{int} \end{cases} \tag{II.87}$$

The Cauchy problems introduced above can be easily implemented in any dynamic solver to fully characterise membrane performance and water fluxes exchanged with electrodes, integrating every-time step with every numerical scheme. Here, the implementation approach is finally proposed to be applied every time-step:

1. Compute the Peclet number, based on operating conditions and membrane characteristics:

$$Pe = \frac{u_{EOD} + u_{conv}^{dry}}{u_{diff}}$$

2. Identify the membrane steady-state condition from Peclet and boundary conditions:

$$\bar{\lambda}_s = \lambda_a + (\lambda_c - \lambda_a) \left(\frac{1}{Pe} - \frac{1}{e^{Pe} - 1} \right)$$

3. Identify the membrane characteristic time, based on Peclet and mem-

brane features:

$$t_d = \frac{L_{mem}^{dry^2}}{D_T^{chem}\Gamma^*}\frac{e^{Pe}Pe - 2e^{Pe} + Pe + 2}{2Pe^2\left(e^{Pe} - 1\right)}$$

4. Integrate the following ODEs:

$$\frac{d\bar{\lambda}^*}{dt} = \frac{\bar{\lambda}_s - \bar{\lambda}^*}{t_d}$$
$$\frac{d\xi^{int}}{dt} = \frac{\xi_s^{int} - \xi^{int}}{t_d}$$
$$\frac{d\lambda^{int}}{dt} = \frac{\lambda_s^{int} - \lambda^{int}}{t_d}$$

5. Compute the water molar fluxes at boundaries:

$$J_a^*(t) = c_{mem}^{dry} u_{diff}\left(\lambda_a Pe - \frac{\lambda^{int} - \lambda_a}{\xi^{int}}\right)$$
$$J_c^*(t) = c_{mem}^{dry} u_{diff}\left(\lambda_c Pe - \frac{\lambda_c - \lambda^{int}}{1 - \xi^{int}}\right)$$

The proposed implementation algorithm serves two main objectives. First of all, the average water membrane content integration is needed to identify the membrane Ohmic resistance, which can be calculated using the same formulation proposed by Springer, T. A. Zawodzinski, and Gottesfeld (1991). Secondly, the water fluxes exchanged between membrane and electrodes is useful in cell comprehensive models where mass flows calculations are necessary.

II.5 Conclusions

Within this chapter, an advanced lumped membrane model for water content characterisation and mass flows identification for fast dynamic simulations is proposed. In a first attempt, the comprehensive water molar balance derived from the literature is analysed with the implementation of solving numerical algorithms based on membrane characteristics and operating conditions as well. The water balance is solved both in steady-state and transient conditions, defining the benchmark reference solutions as well as the numerical environment for direct simulations. In the second step, the PDE of the water balance is linearised with reasonable assumptions, leading to the introduction of a linear PDE problem solved with standard differential equation solving techniques. Finally, from the linear PDE problem a new solution is proposed, based on the application of the integral method searching the best approximation of the

linear solution on integral average, together with the fast computation of water fluxes exchanged between membrane and electrodes.

The analytical integral solution assumes a linearised representation of the water balance PDE. This approximation holds with high accuracy ($R^2 > 0.999$) under standard operating conditions typical of near-ambient or low-to-medium current density regimes. However, the model accuracy could decreases in high Peclet number regimes ($Pe \gg 10$), where strong convective/drag forces dominate over diffusion, or under extremely high current density steps where sharp local water content gradients and severe non-linear membrane swelling occur; furthermore, the main assumption on Γ is valid only when $\lambda < 5$, reducing the model validity in case of severe drying conditions. Under such off-design situations, the higher-order non-linear terms in the diffusion coefficient cannot be fully neglected, requiring either dynamic adaptation of the linearisation parameters or full numerical grid resolution.

This activity leads to the definition of a simple implementation algorithm based on few parameters and three dynamic states to be integrated, that can be implemented in any model or on-board virtual sensors thanks to its simplicity and accuracy. The algorithm presented here is strongly grounded on physical consistency and it is tested in different operating conditions, showing robustness and correlation with numerical reference.

Chapter III
PEMFC lumped model for on-board monitoring and control purposes

In this chapter, the activities for PEMFC stack modelling are presented. The development of mathematical models must always have rigorous physical assumptions in order to write coherent equations that represent the behaviour of the components; hence, every model presented here is characterised firstly by their main assumptions. The modelling activity involves the PEMFC stack at the cell level, focussing on internal transport mechanisms, liquid water behaviour, and membrane performance. The model is a main advancement of a previous work (Esposito, Pianese, and Guezennec 2010). Once the model is presented as a whole, the validation is carried out with experimental data available from the literature and from a previous experimental campaign conducted in the Laboratory (Lipartiti 2022).

III.1 Model description and main assumptions

The PEMFC model presented here aims to calculate the mass of every species (hence, pressure) to characterise the thermodynamic properties needed for the polarisation curve: several control volumes are defined, and, for each control volume, dynamic mass balances are computed for every species.

The most important hypothesis is the equivalent single cell approach: it is assumed that every cell in the stack behaves the same, with identical properties and no temperature gradient across the stack. This hypothesis allows to scale down the problem at the cell level, characterising the phenomenology for a single cell. The single cell is divided into sub-volumes: for each of them, the mean value modelling approach is adopted, assuming spatially uniform thermodynamic properties. Between the sub-volumes, it is assumed that exchanged mass flows are one-dimensional across sub-volumes, defining a preferred flow

direction. Finally, the heat transfer between gases and cell materials is considered instantaneous, assuming an equal temperature shared by the gases inside and the volume walls. These five physical hypotheses are the fundamental background for the proposed modelling approach.

The single cell is divided into three main volumes: anode, membrane, and cathode; while the two electrodes share the same modelling approach, the membrane model is described in a proper following section. Every electrode is further divided into three sub-volumes: (i) GFC; (ii) GDL; (iii) CL. In turn, the GDL is further divided in three parts, from GFC-GDL interface to GDL core to GDL-CL interface: this division is considered to account for capillarity phenomenon accuracy, since the capillary mechanism is strictly related to the GDL porosity and permeability properties (Esposito, Pianese, and Guezennec 2010). Finally, supply and discharge manifolds for both anode and cathode are considered with infinite extension for pressure stabilisation. The gas species considered for every anode volume are hydrogen, vapour water, and liquid water; for every cathode volume, the gases are oxygen, nitrogen, vapour water, and liquid water. No nitrogen crossover is considered between electrodes.

Combining all together, in Figure III.1 the schematic of the proposed model is presented: every sub-volume is drawn as a white box with black borders, while the gas species are reported as coloured arrows, with every colour corresponding to different species (orange: hydrogen; green: oxygen; grey: nitrogen; light blue: vapour water; blue: liquid water).

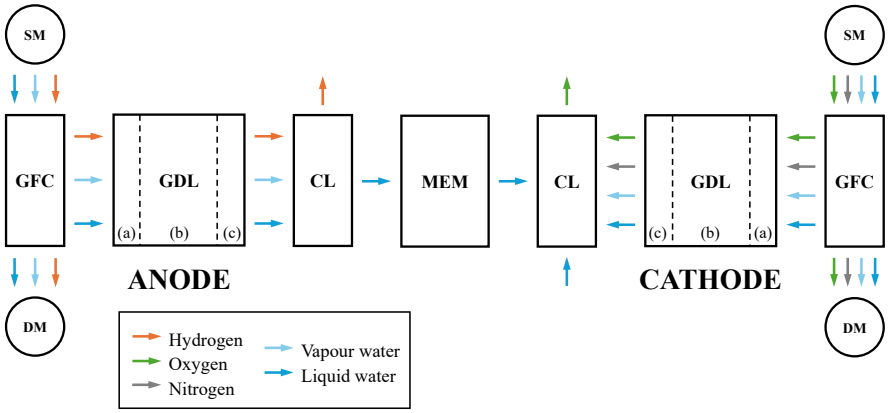


Figure III.1 *PEMFC model schematic, with main volumes and gas flows*

To explicitly frame the novel contribution of the proposed PEMFC dynamic lumped model within the literature, a comparative positioning against widely adopted control-oriented frameworks, such as the benchmark Pukrushpan, H. Peng, and Stefanopoulou (2004) and subsequent dynamic formulations, is sum-

marised in Table III.1. While classical control-oriented models primarily rely on empirical spatial approximations or static membrane hydration assumptions, the integral-method approach applied in this work keeps the physical fidelity for transient water balance dynamics within the membrane while achieving fast execution speeds, making it particularly suited for real-time digital twin and prognostic applications.

Table III.1 *Model comparison with literature works.*

Literature work	**Modelling approach**	**Membrane model**	**Real-time capability**	**Applications**
Pukrushpan, H. Peng, and Stefanopoulou (2004)	Lumped mean-value model	Uniform water content distribution	High	Air-feed control systems design
Strahl et al. (2014)	Non-linear 1D lumped-parameter model	Diffusion, EOD, and cathode liquid water dynamics	Low to Moderate	Water management and flooding/dehydration diagnosis
F. Chen, Zhang, and J. Jiao (2021)	Dynamic multi-dimensional (2D/3D) PDE model	Multiphase transport, phase change and channel distribution	Very Low (Offline)	Micro-structural component design and local optimization
Proposed model	Physics-based lumped with integral PDE method	Analytical dynamic spatial water profile	High	On-board diagnostics, prognostics, optimal EMS

III.1.1 Mass balances

Following the mean value modelling approach, for every sub-volume and for every species, the mass balance ODE is defined and integrated at each time step.

For hydrogen, the mass balance equations to be integrated for the anode are

shown below:

$$\begin{cases} \dfrac{dm_{H_2}^{GFC}}{dt} = \dot{m}_{H_2}^{SM\to GFC} - \dot{m}_{H_2}^{GFC\to GDL(a)} - \dot{m}_{H_2}^{GFC\to DM} \\ \dfrac{dm_{H_2}^{GDL(a)}}{dt} = \dot{m}_{H_2}^{GFC\to GDL(a)} - \dot{m}_{H_2}^{GDL(a)\to GDL(b)} \\ \dfrac{dm_{H_2}^{GDL(b)}}{dt} = \dot{m}_{H_2}^{GDL(a)\to GDL(b)} - \dot{m}_{H_2}^{GDL(b)\to GDL(c)} \\ \dfrac{dm_{H_2}^{GDL(c)}}{dt} = \dot{m}_{H_2}^{GDL(b)\to GDL(c)} - \dot{m}_{H_2}^{GDL(c)\to CL} \\ \dfrac{dm_{H_2}^{CL}}{dt} = \dot{m}_{H_2}^{GDL(c)\to CL} - \dot{m}_{H_2}^{st} \end{cases} \tag{III.1}$$

The mass flow signs are taken by convention from outside to inside the cell. The flow exchanged between GFC and manifolds $\dot{m}_{H_2}^{SM\to GFC}$ and $\dot{m}_{H_2}^{GFC\to DM}$ is defined by the nozzle equation; the application of the isentropic nozzle theory is shown in the proper section. The flow exchanged between the generic sub-volumes i and j $\dot{m}_{H_2}^{i\to j}$ is a combination of diffusion and convection transport mechanisms; the physical equations involved are shown in the following section. Finally, the stoichiometric hydrogen consumption $\dot{m}_{H_2}^{st}$ can be easily calculated from the hydrogen oxidation reaction, as shown below:

$$\dot{m}_{H_2}^{st} = \frac{I}{2F} M_{H_2} \tag{III.2}$$

For oxygen, the mass balance equations to be integrated for the cathode are shown below:

$$\begin{cases} \dfrac{dm_{O_2}^{GFC}}{dt} = \dot{m}_{O_2}^{SM\to GFC} - \dot{m}_{O_2}^{GFC\to GDL(a)} - \dot{m}_{O_2}^{GFC\to DM} \\ \dfrac{dm_{O_2}^{GDL(a)}}{dt} = \dot{m}_{O_2}^{GFC\to GDL(a)} - \dot{m}_{O_2}^{GDL(a)\to GDL(b)} \\ \dfrac{dm_{O_2}^{GDL(b)}}{dt} = \dot{m}_{O_2}^{GDL(a)\to GDL(b)} - \dot{m}_{O_2}^{GDL(b)\to GDL(c)} \\ \dfrac{dm_{O_2}^{GDL(c)}}{dt} = \dot{m}_{O_2}^{GDL(b)\to GDL(c)} - \dot{m}_{O_2}^{GDL(c)\to CL} \\ \dfrac{dm_{O_2}^{CL}}{dt} = \dot{m}_{O_2}^{GDL(c)\to CL} - \dot{m}_{O_2}^{st} \end{cases} \tag{III.3}$$

The sign convention is the same as the one considered for hydrogen. The

theory for manifolds and inter-volume flows is the same as that presented for computing hydrogen mass balances. The stoichiometric oxygen consumption $\dot{m}^{st}_{O_2}$ is defined from the oxygen reduction reaction with the following relationship:

$$\dot{m}^{st}_{O_2} = \frac{I}{4F} M_{O_2} \tag{III.4}$$

For nitrogen, the mass balance equations to be integrated for the cathode are shown below:

$$\begin{cases} \dfrac{dm^{GFC}_{N_2}}{dt} = \dot{m}^{SM\rightarrow GFC}_{N_2} - \dot{m}^{GFC\rightarrow GDL(a)}_{N_2} - \dot{m}^{GFC\rightarrow DM}_{N_2} \\ \dfrac{dm^{GDL(a)}_{N_2}}{dt} = \dot{m}^{GFC\rightarrow GDL(a)}_{N_2} - \dot{m}^{GDL(a)\rightarrow GDL(b)}_{N_2} \\ \dfrac{dm^{GDL(b)}_{N_2}}{dt} = \dot{m}^{GDL(a)\rightarrow GDL(b)}_{N_2} - \dot{m}^{GDL(b)\rightarrow GDL(c)}_{N_2} \\ \dfrac{dm^{GDL(c)}_{N_2}}{dt} = \dot{m}^{GDL(b)\rightarrow GDL(c)}_{N_2} - \dot{m}^{GDL(c)\rightarrow CL}_{N_2} \\ \dfrac{dm^{CL}_{N_2}}{dt} = \dot{m}^{GDL(c)\rightarrow CL}_{N_2} - \dot{m}^{st}_{N_2} \end{cases} \tag{III.5}$$

The sign convention is the same as before. Since nitrogen is an inert gas for the reduction-oxidation reaction, no stoichiometric consumption or production is present; in addition, the membrane is considered perfectly non-permeable to nitrogen, excluding nitrogen crossover from the model description.

The water mass balances for both vapour and liquid phases are written for both anode and cathode; in addition, the mass balance equations for the same sub-volume are linked by the evaporation/condensation phenomena, which is described in the next section. The equations for vapour mass balances, valid

for both anode and cathode, are shown in the following:

$$\begin{cases} \dfrac{dm^{GFC}_{H_2O,vap}}{dt} = \dot{m}^{SM\rightarrow GFC}_{H_2O,vap} - \dot{m}^{GFC\rightarrow GDL(a)}_{H_2O,vap} - \dot{m}^{GFC\rightarrow DM}_{H_2O,vap} + \\ \qquad\qquad + \dot{m}^{GFC}_{evap} - \dot{m}^{GFC}_{cond} \\ \dfrac{dm^{GDL(a)}_{H_2O,vap}}{dt} = \dot{m}^{GFC\rightarrow GDL(a)}_{H_2O,vap} - \dot{m}^{GDL(a)\rightarrow GDL(b)}_{H_2O,vap} + \\ \qquad\qquad + \dot{m}^{GDL(a)}_{evap} - \dot{m}^{GDL(a)}_{cond} \\ \dfrac{dm^{GDL(b)}_{H_2O,vap}}{dt} = \dot{m}^{GDL(a)\rightarrow GDL(b)}_{H_2O,vap} - \dot{m}^{GDL(b)\rightarrow GDL(c)}_{H_2O,vap} + \\ \qquad\qquad + \dot{m}^{GDL(b)}_{evap} - \dot{m}^{GDL(b)}_{cond} \\ \dfrac{dm^{GDL(c)}_{H_2O,vap}}{dt} = \dot{m}^{GDL(b)\rightarrow GDL(c)}_{H_2O,vap} - \dot{m}^{GDL(c)\rightarrow CL}_{H_2O,vap} + \\ \qquad\qquad + \dot{m}^{GDL(c)}_{evap} - \dot{m}^{GDL(c)}_{cond} \\ \dfrac{dm^{CL}_{H_2O,vap}}{dt} = \dot{m}^{GDL(c)\rightarrow CL}_{H_2O,vap} + \dot{m}^{CL}_{evap} - \dot{m}^{CL}_{cond} \end{cases} \tag{III.6}$$

The vapour water transport mechanisms are still diffusion and convection. As it can be seen, the evaporation rate is modelled for the generic i volume with $\dot{m}^{i}_{evap}$, while the condensation rate is modelled with $\dot{m}^{i}_{cond}$. The liquid water mass balances are different for the anode and cathode sub-volumes; for the anode, the liquid water mass balances are shown below:

$$\begin{cases} \dfrac{dm^{An,GFC}_{H_2O,liq}}{dt} = \dot{m}^{An,SM\rightarrow GFC}_{H_2O,liq} - \dot{m}^{An,GFC\rightarrow GDL(a)}_{H_2O,liq} + \\ \qquad - \dot{m}^{An,GFC\rightarrow DM}_{H_2O,liq} - \dot{m}^{An,GFC}_{evap} + \dot{m}^{An,GFC}_{cond} \\ \dfrac{dm^{An,GDL(a)}_{H_2O,liq}}{dt} = \dot{m}^{An,GFC\rightarrow GDL(a)}_{H_2O,liq} - \dot{m}^{An,GDL(a)\rightarrow GDL(b)}_{H_2O,liq} + \\ \qquad\qquad - \dot{m}^{An,GDL(a)}_{evap} + \dot{m}^{An,GDL(a)}_{cond} \\ \dfrac{dm^{An,GDL(b)}_{H_2O,liq}}{dt} = \dot{m}^{An,GDL(a)\rightarrow GDL(b)}_{H_2O,liq} - \dot{m}^{An,GDL(b)\rightarrow GDL(c)}_{H_2O,liq} + \\ \qquad\qquad - \dot{m}^{An,GDL(b)}_{evap} + \dot{m}^{An,GDL(b)}_{cond} \\ \dfrac{dm^{An,GDL(c)}_{H_2O,liq}}{dt} = \dot{m}^{An,GDL(b)\rightarrow GDL(c)}_{H_2O,liq} - \dot{m}^{An,GDL(c)\rightarrow CL}_{H_2O,liq} + \\ \qquad\qquad - \dot{m}^{An,GDL(c)}_{evap} + \dot{m}^{An,GDL(c)}_{cond} \\ \dfrac{dm^{An,CL}_{H_2O,liq}}{dt} = \dot{m}^{An,GDL(c)\rightarrow CL}_{H_2O,liq} - \dot{m}^{An,CL\rightarrow mem}_{H_2O,liq} - \dot{m}^{An,CL}_{evap} + \\ \qquad\qquad + \dot{m}^{An,CL}_{cond} \end{cases} \tag{III.7}$$

For liquid water, the main transport mechanisms considered are convection and capillarity: a detailed description of mass flow calculation is provided in the next sections. In addition, the water flow from CL to the membrane $\dot{m}_{H_2O,liq}^{An,CL\rightarrow mem}$ is considered, with a detailed description of the phenomena in the membrane section. For the cathode, the balances are similar, as shown below:

$$\begin{cases} \dfrac{dm_{H_2O,liq}^{Ca,GFC}}{dt} = \dot{m}_{H_2O,liq}^{Ca,SM\rightarrow GFC} - \dot{m}_{H_2O,liq}^{Ca,GFC\rightarrow GDL(a)} + \\ \qquad -\dot{m}_{H_2O,liq}^{Ca,GFC\rightarrow DM} - \dot{m}_{evap}^{Ca,GFC} + \dot{m}_{cond}^{Ca,GFC} \\ \dfrac{dm_{H_2O,liq}^{Ca,GDL(a)}}{dt} = \dot{m}_{H_2O,liq}^{Ca,GFC\rightarrow GDL(a)} - \dot{m}_{H_2O,liq}^{Ca,GDL(a)\rightarrow GDL(b)} + \\ \qquad -\dot{m}_{evap}^{Ca,GDL(a)} + \dot{m}_{cond}^{Ca,GDL(a)} \\ \dfrac{dm_{H_2O,liq}^{Ca,GDL(b)}}{dt} = \dot{m}_{H_2O,liq}^{Ca,GDL(a)\rightarrow GDL(b)} - \dot{m}_{H_2O,liq}^{Ca,GDL(b)\rightarrow GDL(c)} + \\ \qquad -\dot{m}_{evap}^{Ca,GDL(b)} + \dot{m}_{cond}^{Ca,GDL(b)} \\ \dfrac{dm_{H_2O,liq}^{Ca,GDL(c)}}{dt} = \dot{m}_{H_2O,liq}^{Ca,GDL(b)\rightarrow GDL(c)} - \dot{m}_{H_2O,liq}^{Ca,GDL(c)\rightarrow CL} + \\ \qquad -\dot{m}_{evap}^{Ca,GDL(c)} + \dot{m}_{cond}^{Ca,GDL(c)} \\ \dfrac{dm_{H_2O,liq}^{Ca,CL}}{dt} = \dot{m}_{H_2O,liq}^{Ca,GDL(c)\rightarrow CL} + \dot{m}_{H_2O,liq}^{Ca,CL\rightarrow mem} - \dot{m}_{evap}^{Ca,CL} + \\ \qquad +\dot{m}_{cond}^{Ca,CL} + \dot{m}_{H_2O,liq}^{st} \end{cases} \tag{III.8}$$

For the cathode, along with the water flow coming from the membrane $\dot{m}_{H_2O,liq}^{mem\rightarrow Ca,CL}$, the water generation term $\dot{m}_{H_2O,liq}^{st}$, defined by the reaction stoichiometry as follows:

$$\dot{m}_{H_2O,liq}^{st} = \frac{I}{2F} M_{H_2O} \tag{III.9}$$

III.1.2 Gas mixture properties

For the generic sub-volume i, the main thermodynamic and physical properties can be calculated, starting from geometrical features and the mass balances. The mass fraction of the generic species a can be calculated as follows:

$$y_a^i = \frac{m_a^i}{\sum_a m_a^i} \tag{III.10}$$

In addition, the molar fraction of the generic species a can be calculated

from the single masses, as shown below:

$$x_a^i = \frac{\frac{m_a^i}{M_a}}{\sum_a \frac{m_a^i}{M_a}} \tag{III.11}$$

For the molar fractions, liquid water should not be considered in the computation, since it is a gas-related parameter. Thanks to the isothermal hypothesis, the partial pressure of the generic species can be calculated using Dalton's law under the assumption of a perfect gas:

$$p_a^i = \frac{\frac{m_a^i}{M_a}\tilde{R}T_{FC}}{V_{eff}^i} \tag{III.12}$$

where V_{eff}^i is the effective available volume for the gas mixture, accounting for porosity and liquid water amount, calculated as follows:

$$V_{eff}^i = \left(1 - s^i\right)\varepsilon^i V_{geom}^i \tag{III.13}$$

where ε^i is the electrode porosity, while V_{geom}^i is the geometric volume of the considered sub-volume. Furthermore, s^i is the liquid water saturation, calculated from water mass:

$$s^i = \frac{m_{H_2O,liq}^i}{\rho_{H_2O,liq}\varepsilon^i V_{geom}^i} \tag{III.14}$$

The water molar concentration is another key parameter that can be derived from mass balances since it is needed to define the boundary conditions of membrane water balance, described in the following section. The water molar concentration for the generic volume is defined as follows:

$$c_{H_2O}^i = \frac{m_{H_2O,vap}^i + m_{H_2O,liq}^i}{M_{H_2O}\varepsilon^i V_{geom}^i} \tag{III.15}$$

The thermodynamic properties of the gas mixture can be calculated using the molar fraction presented with eq. (III.11). The isentropic expansion coefficient is defined with the following:

$$\gamma^i = \sum_a x_a^i \gamma_a \tag{III.16}$$

The gas constant can also be calculated with molar fractions as follows:

$$R^i = \frac{\tilde{R}}{\sum_a x_a^i M_a} \tag{III.17}$$

III.1.3 Supply and discharge manifold flows

Due to pressure gradient, the mass flow between manifolds and GFCs through the respective nozzle can be modelled as a subsonic flow: there is room for the implementation of the isentropic nozzle equation for both the supply and discharge manifolds and both electrodes.

The general nozzle mass flow for gas mixtures can be modelled with the following:

$$\dot{m}_{gas}^{i\to j} = C_d^i A^i \rho_{gas}^i v_{gas}^{i\to j} \tag{III.18}$$

where the flow mean speed $v_{gas}^{i\to j}$ is a fraction of the propagation speed:

$$v_{gas}^{i\to j} = \sqrt{\gamma^i R^t T^i}\sqrt{\frac{2}{\gamma^i - 1}}\sqrt{\left(\frac{p_{gas}^j}{p_{gas}^i}\right)^{\frac{2}{\gamma^i}} - \left(\frac{p_{gas}^j}{p_{gas}^i}\right)^{\frac{\gamma^i+1}{\gamma^i}}} \tag{III.19}$$

The pressure ratio is saturated between unity, i.e., zero pressure gradient causing no mass flow, and the critical ratio:

$$\left(\frac{p_{gas}^j}{p_{gas}^i}\right)_{crit} = \left(\frac{2}{\gamma^i + 1}\right)^{\frac{\gamma^i}{\gamma^i - 1}} \tag{III.20}$$

Once the gas mixture mass flow is known, the molar fraction introduced with eq. (III.11) can be used to specify the mass flow of the single species. For the supply flow, the mass flow is calculated using the following:

$$\dot{m}_a^{SM\to GFC} = x_a^{SM}\dot{m}_{gas}^{SM\to GFC} \tag{III.21}$$

For the discharge flow, a similar relationship applies:

$$\dot{m}_a^{GFC\to DM} = x_a^{GFC}\dot{m}_{gas}^{GFC\to DM} \tag{III.22}$$

For liquid water, a different approach is considered. No incoming liquid water is considered from the supply manifolds, assuming that no condensation occurs before entering the cell gas flow channels; for discharge manifolds, a modified Bernoulli principle is implemented, assuming a water film flow

corrected by a non-linear factor:

$$\dot{m}_{H_2O,liq}^{GFC\rightarrow DM} = \left(s^{GFC}\right)^{l} C_d^{GFC} A^{GFC} \rho_{H_2O,liq} \sqrt{2\frac{p^{GFC} - p^{DM}}{\rho_{H_2O,liq}}} \tag{III.23}$$

The non-linear correction is introduced to scale down the Bernoulli flow from totally dry conditions (i.e., $s^{GFC} = 0$) to fully flooded conditions (i.e., $s^{GFC} = 1$). The exponential factor s has been tuned in a previous master thesis (Amatruda 2014).

III.1.4 Transport mechanisms

As already mentioned, three different transport mechanisms are considered for the species inside the single cell. For gas species including water vapour, diffusion and convection are considered with the following equation:

$$\dot{m}_{gas}^{i\rightarrow j} = \dot{m}_{diff}^{i\rightarrow j} + \dot{m}_{conv}^{i\rightarrow j} \tag{III.24}$$

For liquid water only, convection and capillarity are the main transport mechanisms, as shown below:

$$\dot{m}_{H_2O,liq}^{i\rightarrow j} = \dot{m}_{conv}^{i\rightarrow j} + \dot{m}_{cap}^{i\rightarrow j} \tag{III.25}$$

The convective transport is shared between gases and liquid water: in the case of liquid water, the pressure effect on water density is neglected, unlike gases.

The diffusion transport mechanism is related to concentration gradient across the media, media porosity, and gases interaction. Since a gas mixture is involved in the process, the Stefan-Maxwell discretised equations for binary diffusion (Barbir 2013) between two generic volumes i and j for two generic species a and b can be considered:

$$\begin{cases} \dfrac{x_a^i - x_a^j}{L^{i\rightarrow j}} = \dfrac{\tilde{R}T_{FC}}{p^j} \dfrac{x_a^i \dot{n}_b^{i\rightarrow j} - x_b^i \dot{n}_a^{i\rightarrow j}}{D_{ab,eff}^i} \\ \dfrac{x_b^i - x_b^j}{L^{i\rightarrow j}} = \dfrac{\tilde{R}T_{FC}}{p^j} \dfrac{x_b^i \dot{n}_a^{i\rightarrow j} - x_a^i \dot{n}_b^{i\rightarrow j}}{D_{ab,eff}^i} \end{cases} \tag{III.26}$$

where $D_{ab,eff}^i$ is the effective binary diffusion coefficient, a combination of pure binary diffusion and porous media interaction applying the parallel

resistors' similarity approach:

$$\frac{1}{D^i_{ab,eff}} = \frac{1}{D^i_{ab}} + \frac{1}{D^i_a} + \frac{1}{D^i_b} \tag{III.27}$$

D^i_a and D^i_b are the Knudsen diffusion coefficients of a and b gases, respectively, depending on the volume's mean pore radius r^i_p (Pant, Mitra, and Secanell 2012):

$$D^i_a = \frac{2}{3} r^i_p \sqrt{\frac{8\tilde{R}T_{FC}}{\pi M_a}} \tag{III.28}$$

The binary diffusion coefficient D^i_{ab} is calculated with the empirical model proposed by Barbir (2013), knowing the species critical temperature T_c and pressure p_c as follows:

$$D^i_{ab} = \frac{1.01325 a_g}{p^i} \left(\frac{T_{FC}}{\sqrt{T_{c,a}T_{c,b}}} \right)^{b_g} \sqrt[3]{p_{c,a}p_{c,b}} \left(T_{c,a}T_{c,b}\right)^{\frac{5}{12}} \sqrt{\frac{1}{M_a} + \frac{1}{M_b}} \tag{III.29}$$

where the coefficients a_g and b_g are empirical coefficients that differ between pure gas interactions and gas-water vapour interactions. The diffusion equations can be collected in a linear system of equations with molar flows as unknowns:

$$\mathbf{A} \begin{bmatrix} \vdots \\ \dot{n}_a^{i \to j} \\ \vdots \end{bmatrix} = \mathbf{b} \tag{III.30}$$

However, this system of equations is redundant by definition due to the molar conservation law; hence, the pseudo-inversion of the coefficients matrix is implemented to ensure the calculation of molar flows.

The convective transport mechanism is related to the pressure gradient across the media, the media porosity, and the interaction between different gas species. For the generic a fluid, the volume flow exchange between i and j volumes can be calculated by applying the discretised Darcy's convection law:

$$\dot{V}_a^{i \to j} = -\frac{k^i_{perm} A^i}{\mu_a} \frac{p^j - p^i}{L^{i \to j}} \tag{III.31}$$

where k^i_{perm} is the volume permeability, A_i is the flow cross-sectional area, μ_a is the fluid viscosity, and $\frac{p^j - p^i}{L^{i \to j}}$ is the discretised pressure gradient. The Darcy

convection law is valid for both gases and liquid water. The gas viscosity is a function of temperature applying the Sutherland law as follows:

$$\mu_{gas} = \mu_{0,gas} \frac{T_{0,gas} + C_{gas}}{T_{FC} + C_{gas}} \left(\frac{T_{FC}}{T_{0,gas}} \right)^{\frac{3}{2}} \tag{III.32}$$

where $\mu_{0,gas}$ and $T_{0,gas}$ are the reference viscosity and temperature, respectively, while C_{gas} is the Sutherland constant. For water vapour, the dynamic viscosity is calculated using an appropriate model proposed by Sengers and Kamgar-Parsi (1984):

$$\mu_{H_2O,vap} = g \left(\frac{T_{FC}}{T^*} \right) f \left(\frac{\rho_{H_2O,vap}}{\rho^*_{H_2O,vap}}, \frac{T_{FC}}{T^*} \right) \tag{III.33}$$

where f and g are functions identified by the authors, while T^* and $\rho^*_{H_2O,vap}$ are the reference temperature and vapour density. For liquid water, the empirical model proposed by Kestin, Sokolov, and Wakeham (1978) is considered:

$$\begin{aligned} \log \left(\frac{\mu_{H_2O,liq}}{\mu^*_{H_2O,liq}} \right) = \frac{20 - T_{FC}}{T_{FC} + 96} \Big(& 1.2378 - 1.303 \cdot 10^{-3} \left(20 - T_{FC}\right) + \\ & + 3.06 \cdot 10^{-6} \left(20 - T_{FC}\right)^2 + 2.55 \cdot 10^{-8} \left(20 - T_{FC}\right)^3 \Big) \end{aligned} \tag{III.34}$$

where $\mu^*_{H_2O,liq}$ is the reference liquid water viscosity measured at 20 °C, while T_{FC} is expressed in Celsius degrees °C.

The capillarity mechanism involves only liquid water and it accounts for water emerging from inside to outside across media porosity due to surface tension. The capillary flow can be modelled as a capillary pressure gradient-driven mechanism, similar to convective transport, as shown below (Domenico 2007):

$$\dot{m}^{i \to j}_{cap} = -\rho_{H_2O,liq} \frac{k^j_{perm,liq} \left(s^j\right)^{2.16} A^i}{\mu_{H_2O,liq}} \frac{p^j_{cap} - p^i_{cap}}{L^{i \to j}} \varepsilon^j \left(1 - s^j\right) \tag{III.35}$$

where $k^j_{perm,liq}$ is the media liquid permeability, while $\frac{p^j_{cap} - p^i_{cap}}{L^{i \to j}}$ is the discretised capillary pressure gradient across the media. The capillary transport depends on the available void volume; hence, the correction of porosity with water saturation s^j is needed. To calculate the capillary pressure, the modified Leverett equation from carpentry engineering (Kumbur, Sharp, and Mench 2007) is implemented as follows:

$$p^i_{cap} = -4854.1 \left(s^i_{red}\right)^2 + 12958 s^i_{red} \tag{III.36}$$

where s^i_{red} is the reduced water saturation, accounting for immobile conditions s_{imm}:

$$s^i_{red} = \frac{s^i - s_{imm}}{1 - s_{imm}} \tag{III.37}$$

III.1.5 Water evaporation and condensation modelling

As presented in the previous sections, the water mass balances share a common flow depending on condensation and evaporation phenomena. Liquid water can evaporate if the vapour water partial pressure is lower than the saturation pressure, i.e., the relative humidity is lower than unity; on the other hand, when the vapour water partial pressure is higher than the saturation water pressure, excess vapour mass must condense into liquid water to limit the relative humidity down to unity. The two physical behaviours are modelled considering the needed/excess vapour amount to obtain a fully saturated gas mixture.

In a given volume i, evaporation occurs when vapour water partial pressure is lower than the saturation pressure:

$$p^i_{H_2O,vap} < p_{sat} \tag{III.38}$$

where the water saturation pressure p_{sat} is a function of temperature expressed by the Buck equation (Buck Research Instruments L.L.C 1996):

$$p_{sat} = 0.61121 \exp\left(\left(18.678 - \frac{T_{FC}}{234.5}\right)\frac{T_{FC}}{257.14 - T_{FC}}\right) \tag{III.39}$$

where p_{sat} is expressed in kPa, while the temperature is expressed in Celsius degrees °C. This model is significantly more accurate than other interpolations available in the literature, even if it requires a slightly higher computational burden. When the evaporation constraint is respected, the required liquid mass needed to evaporate is calculated from the pressure difference applying the ideal gas law as follows:

$$\dot{m}^i_{evap} = \frac{1}{\tau_{evap}} \frac{p_{sat} - p^i_{H_2O,vap}}{\frac{\tilde{R}}{M_{H_2O}} T_{FC}} V^i_{eff} \tag{III.40}$$

where τ_{evap} is a characteristic time constant identified from literature (Domenico 2007).

Similarly to evaporation, for a given volume i condensation occurs when

water vapour partial pressure is higher than the saturation pressure:

$$p^i_{H_2O,vap} > p_{sat} \tag{III.41}$$

When the condensation constraint is respected, the required liquid mass needed to evaporate is calculated from the pressure difference applying the ideal gas law as follows:

$$\dot{m}^i_{cond} = \frac{1}{\tau_{cond}} \frac{p^i_{H_2O,vap} - p_{sat}}{\frac{\tilde{R}}{M_{H_2O}} T_{FC}} V^i_{eff} \tag{III.42}$$

where τ_{evap} is a characteristic time constant identified from the literature (Domenico 2007).

III.1.6 Polarisation curve and electrical performance

The results obtained from the mass balances are fundamental to determine every term of the polarization curve of the single cell, needed to characterize stack electrical performances. According to Larminie and Dicks (2003), the single cell voltage is given by the algebraic summation of open circuit voltage and irreversible losses as shown:

$$V_{FC} = E_{Nernst} - V_{act} - V_{Ohm} - V_{conc} - V_{off} \tag{III.43}$$

where E_{Nernst} is the Nernst potential, while V_{act}, V_{Ohm}, V_{conc}, and V_{off} are, respectively, the activation, Ohmic, concentration, and offset losses. The Nernst potential represents the reversible open circuit voltage of the single cell, operating in non-reference conditions, due only to chemical potential. It can be calculated with the Nernst equation:

$$E_{Nernst} = E_0\left(T_{FC}\right) + \frac{\tilde{R} T_{FC}}{2F} \log\left(\frac{\frac{p^{CL}_{H_2}}{p_0} \left(\frac{p^{CL}_{O_2}}{p_0} \right)^{\frac{1}{2}}}{\frac{p^{Ca,CL}_{H_2O}}{p_0}} \right) \tag{III.44}$$

where $E_0\left(T\right)$ is the reversible open circuit voltage in reference condition, defined by the Gibbs free energy variation, while $\frac{p_i}{p_0}$ is the gas activity referred to atmospheric pressure p_0. Considering temperatures lower than 100 °C, the water activity is equal to unity since the produced water is liquid. To calculate the reversible open circuit voltage in the hypothesis of liquid water generation,

the following linear interpolation is accounted:

$$E_0\left(T_{FC}\right) = 1.229 - 0.8676 \cdot 10^{-3}\left(T_{FC} - 298.15\right) \tag{III.45}$$

The activation irreversible losses are due to the energetical barrier to be overcome to sustain the electrochemical reactions happening on reaction sites, influenced by temperature and available electroactive area. The activation losses are calculated with Tafel equation:

$$V_{act} = \frac{\tilde{R}T_{FC}}{2F\alpha}\log\frac{i}{i_0} \tag{III.46}$$

where i is the current density, equal to the ratio between current and fuel cell cross-sectional area, α is the charge transfer coefficient, while i_0 is the exchange current density referred to chemical equilibrium conditions:

$$i_0 = i_{0,Pt}S_{Pt}W_{Pt}U_{Pt} \tag{III.47}$$

where $i_{0,Pt}$ is the reference exchange current density per catalyst particle surface unit, S_{Pt} is the catalyst particle surface area, W_{Pt} is the platinum loading, and U_{Pt} is the catalyst utilisation factor. PEM fuel cells generally use platinum as catalyst; hence, the catalyst specie is here referred directly as Pt.

The Ohmic losses are mainly due to the electrical internal resistance of proton flow across the membrane. This class of irreversible losses depends on current, temperature, and membrane humidification. The Ohmic losses are calculable with Ohm's law:

$$V_{Ohm} = ri \tag{III.48}$$

where r is the area specific resistance, depending on Ohmic conductivity as follows:

$$r = \frac{L_{mem}}{\sigma_{mem}} \tag{III.49}$$

where L_{mem} is the membrane thickness, while σ_{mem} is the membrane Ohmic lineal conductivity. The membrane thickness can change when the membrane is humidified due to the swelling effect: more details are provided in the membrane model section. The Ohmic conductivity is modelled with the empirical model introduced by Springer, T. A. Zawodzinski, and Gottesfeld (1991):

$$\sigma_{mem} = \left(0.005139\bar{\lambda}_{mem} - 0.00326\right)\exp\left(1268\left(\frac{1}{303} - \frac{1}{T_{FC}}\right)\right) \tag{III.50}$$

where $\bar{\lambda}_{mem}$ is the average membrane water content. The estimation of average

membrane water content is crucial to calculate the Ohmic resistance, that is the cause of the main irreversible voltage loss all over the operative range and it is strongly linked to water management.

The concentration losses are due to reactants unavailability with respect to stoichiometry conditions in reaction sites, since the diffusive transport is slower than reactants consumption. This losses typology can be calculated with the following model:

$$V_{conc} = -\frac{\tilde{R}T_{FC}}{2F}\log\left(1 - \frac{i}{i_{lim}}\right) \tag{III.51}$$

where i_{lim} is the limiting current density, defined as the maximum current density possible when diffusion and reactants consumption speeds are balanced. The limiting current density can be referred both for anode and cathode sides; however, the hydrogen limiting current density is generally higher than oxygen one, since hydrogen diffuse faster. Hence, the limiting current density considered is modelled with the formulation proposed by Maggio, Recupero, and Pino (2001):

$$i_{lim} = -\frac{2FD_{O_2N_2}\left(\varepsilon_{mem}\left(1 - s^{Ca,CL}\right)\right)^{1.5}\left(\frac{T_{FC}}{273}\right)^{0.853}}{V_m\left(L_{GDL} + L_{CL}\right)}\log\left(1 - x_{O_2}^{Ca,CL}\right) \tag{III.52}$$

where $D_{O_2N_2}$ and V_m are, respectively, oxygen-nitrogen binary diffusion coefficient and molar volume in standard conditions, while ε_{mem} is the membrane porosity, and $L_{GDL} + L_{CL}$ is the total diffusion thickness.

The offset losses account for three main phenomena: (i) molecular hydrogen cross-flow across the membrane, due to imperfect gas impermeability; (ii) electron flow across the membrane, due to imperfect membrane electrical insulation; (iii) other gas losses. For the purposes of this work, the offset losses are directly tuned based on difference between theoretical and measured open circuit voltages.

Once the polarization curve is defined, for the single cell it is possible to calculate the electrical power as the simple product between voltage and current as follows:

$$P_{FC} = V_{FC}I \tag{III.53}$$

where A_{FC} is the fuel cell orthogonal area. To characterize the stack performances, it is useful to remark that the single cells are connected in electrical series, meaning that the stack voltage is the summation of the single cells

voltage as follows:

$$V_{stack} = N_{cells} V_{FC} \tag{III.54}$$

where N_{cells} is the total number of cells mounted within the stack, assuming that every cell behaves the same. The stack power is then defined as shown:

$$P_{stack} = V_{stack} I \tag{III.55}$$

Finally, the stack efficiency can be defined as the ratio between electrical power and total hydrogen chemical energy consumption as follows:

$$\eta_{stack} = \frac{P_{stack}}{N_{cells} \dot{m}^{st}_{H_2} LHV_{H_2}} \tag{III.56}$$

where LHV_{H_2} is the hydrogen lower heating value. It is interesting to note that the stack efficiency, also equal to cell efficiency due to the single cell assumption, can be also seen to the product between two distinct efficiency, one thermodynamic and one electrical, as follows:

$$\eta_{FC} = \eta_{stack} = \frac{-\Delta G}{LHV_{H_2}} \frac{V_{FC}}{E_0} = \eta_{th} \eta_{el} \tag{III.57}$$

This type of formulation shows that the total efficiency depends on thermodynamic properties, i.e., the energy conversion efficiency between chemical and electrical, and electrical irreversibility, i.e., the ratio between theoretical open circuit voltage and actual voltage.

III.1.7 Dynamic energy balance

Considering the assumptions of single cell hypothesis, no temperature gradient across the stack, and ideal heat transfer between cell and gases, the following first-principle thermodynamic balance is introduced to model the stack temperature:

$$m_{stack} c_{stack} \frac{dT_{FC}}{dt} = \dot{H}_{in} - \dot{H}_{out} + N_{cells} \dot{m}^{st}_{H_2} LHV_{H_2} - P_{stack} \tag{III.58}$$

where m_{stack} and C_{stack} are, respectively, stack mass and specific heat capacity, while $\dot{H}_{in}$ and $\dot{H}_{out}$ are, respectively, inlet and outlet enthalpy flows. This thermal balance approach defines the temperature variation as the consequence of enthalpy flows of inlet and outlet gases and the heat generation due to electrochemical reaction irreversibility as the difference between chemical energy and electrical consumption. Thanks to the hypotheses defined above, the stack

temperature can be considered equal to the single cell temperature. The inlet enthalpy flow is the sum of single enthalpy flows defined as follows:

$$\dot{H}_{in} = N_{cells} \sum_{a} \dot{m}_a^{SM \to GFC} c_{p,a} T^{SM} \tag{III.59}$$

where $c_{p,a}$ and T^{SM} are, respectively, specific heat capacity at constant pressure and temperature of the generic a inlet gas. The outlet enthalpy total flow is defined similarly, with the temperature equal to the cell temperature thanks to ideal heat transfer assumption:

$$\dot{H}_{out} = N_{cells} \sum_{a} \dot{m}_a^{GFC \to DM} c_{p,a} T_{FC} \tag{III.60}$$

Integrating the thermal balance, it is possible to define the stack and, hence, the single cell temperature for every time instant.

III.2 Lumped dynamic model for polymeric membrane

The polymeric electrolyte membrane is the core element of the single cell and, as extension, of the entire stack system: the membrane humidification is the key parameter for good cell performance, since it directly influences the Ohmic resistance. In literature, the water membrane content was originally modelled as a black-box function of membrane water activity (Springer, T. A. Zawodzinski, and Gottesfeld 1991) and this black-box model has been widely used through the years; a more sophisticated approach proposed by Mazumder (2005) accounts for the membrane water balance considering three main water transport mechanisms that are properly described in the following paragraphs. In addition, Ferrara, Polverino, and Pianese (2018) derived an analytical solution to the steady-state problem under certain assumptions. In the previous chapter, a dynamic lumped model to directly estimate the average water membrane content is described and validated with literature data; here, the main equations are collected, together with the implementation procedure.

III.2.1 Characterisation of operative conditions

The main water transport mechanisms across the membrane are three the following: electro-osmotic drag, convection, and diffusion. Each mechanism is characterised by a representative transport speed. For the electro-osmotic

drag, the reference speed can be calculated as follows:

$$u_{EOD} = \frac{(0.02T_{FC} - 3.86)\, i}{22.5 c_{mem}^{dry} F} \tag{III.61}$$

where c_{mem}^{dry} is the membrane molar concentration in dry conditions. The convective fluid bulk speed can be estimated with Darcy's law discretising the pressure gradient:

$$u_{conv} = -\frac{k_{liq}^{mem}}{\mu_{H_2O,liq}} \frac{p^{Ca,CL} - p^{An,CL}}{L_{mem}^{dry}} \tag{III.62}$$

where k_{liq}^{mem} is the membrane water permeability, while L_{mem}^{dry} is the membrane dry thickness. The diffusion characteristic speed is defined by the following relationship:

$$u_{diff} = \frac{D_T^{chem} \Gamma^*}{L_{mem}^{dry}} \tag{III.63}$$

where Γ^* is a dimensionless constant, equal to 0.2, while $D_T chem$ is the diffusion coefficient identified as follows:

$$D_T^{chem} = 0.265 \cdot 10^{-4} e^{-\frac{3343}{T_{FC}}} \tag{III.64}$$

The electro-osmotic drag and convective transport mechanisms are advective mechanisms, since they do not depend on water distribution gradient across the membrane. To estimate the ratio between advective forces and diffusion, the Peclet number is introduced:

$$Pe = \frac{u_{EOD} + u_{conv}}{u_{diff}} \tag{III.65}$$

III.2.2 Water membrane content identification

Based on the Peclet number, it is possible to define the average water membrane content in steady-state conditions:

$$\bar{\lambda}_s = \lambda^{An,CL} + \left(\lambda^{Ca,CL} - \lambda^{An,CL}\right)\left(\frac{1}{Pe} - \frac{1}{e^{Pe} - 1}\right) \tag{III.66}$$

where $\lambda^{An,CL}$ and $\lambda^{Ca,CL}$ are electrodes' water membrane contents in CL:

$$\lambda^{An,CL} = \frac{c_{H_2O}^{An,CL}}{c_{mem}^{dry} - \beta c_{H_2O}^{An,CL}} \tag{III.67}$$

$$\lambda^{Ca,CL} = \frac{c_{H_2O}^{Ca,CL}}{c_{mem}^{dry} - \beta c_{H_2O}^{Ca,CL}} \tag{III.68}$$

where β is the membrane swelling factor, equal to 0.0126.

The operating conditions expressed by the Peclet number have also a direct influence on membrane transient response, expressed by the characteristic time delay:

$$t_d = \frac{L_{mem}^{dry}}{u_{diff}} \frac{e^{Pe} Pe - 2e^{Pe} + Pe + 2}{2Pe^2 \left(e^{Pe} - 1\right)} \tag{III.69}$$

Knowing the steady-state solution and the characteristic time, the average membrane water content is modelled as the solution of the following first-order differential equation:

$$\frac{d\bar{\lambda}_{mem}}{dt} = \frac{\bar{\lambda}_s - \bar{\lambda}_{mem}}{t_d} \tag{III.70}$$

With the proposed approach, it is possible to rapidly estimate the average water membrane content based on membrane characteristic and operating conditions as well. The water membrane content, so modelled, is an additional dynamic state that has to be integrated over time. Once the water membrane content is computed, the membrane Ohmic conductivity can be calculated with eq. (III.50).

III.2.3 Net water flows exchange

The membrane exchanges water with electrodes at its boundaries; hence, the membrane flows $\dot{m}_{H_2O,liq}^{An,CL \rightarrow mem}$ and $\dot{m}_{H_2O,liq}^{mem \rightarrow Ca,CL}$ of eqs. (III.7) and (III.8) have to be characterised.

Two additional dynamic states are introduced, needed for the calculation of net water molar fluxes. The two states are referred to a virtual point coordinates of the water distribution profile across the membrane to characterise the distribution gradient at boundaries. The idea behind this modelling approach is well explained in the membrane model chapter. The two coordinates steady-state

conditions are computed from Peclet number and boundary conditions as well:

$$\begin{cases} \xi_s^{int} = \dfrac{e^{Pe}Pe - e^{Pe} + 1}{Pe\left(e^{Pe} - 1\right)} \\ \lambda_s^{int} = \lambda_a + (\lambda_c - \lambda_a)\dfrac{e^{Pe}Pe - e^{Pe} + 1}{\left(e^{Pe} - 1\right)^2} \end{cases} \tag{III.71}$$

Knowing the steady state conditions, the dynamic states are computed with the following ODEs:

$$\begin{cases} \dfrac{d\xi^{int}}{dt} = \dfrac{\xi_s^{int} - \xi^{int}}{t_d} \\ \dfrac{d\lambda^{int}}{dt} = \dfrac{\lambda_s^{int} - \lambda^{int}}{t_d} \end{cases} \tag{III.72}$$

It is assumed that both dynamic states, since they are derived from the same modelling approach used to identify the average water membrane content, are characterised by the same characteristic time t_d.

The net water flows can finally be calculated applying the following:

$$\dot{m}_{H_2O,liq}^{An,CL\rightarrow mem} = M_{H_2O}A_{FC}c_{mem}^{dry}u_{diff}\left(\lambda^{An,CL}Pe - \frac{\lambda^{int} - \lambda^{An,CL}}{\xi^{int}}\right) \tag{III.73}$$

$$\dot{m}_{H_2O,liq}^{mem\rightarrow Ca,CL} = M_{H_2O}A_{FC}c_{mem}^{dry}u_{diff}\left(\lambda^{Ca,CL}Pe - \frac{\lambda^{Ca,CL} - \lambda^{int}}{1 - \xi^{int}}\right) \tag{III.74}$$

III.3 Experimental validation and dynamic testing

To assess the model performance, a validation process involving both steady-state and transient conditions is performed, analysing the average residuals and error distribution across different operating conditions. The reference data are obtained from an experimental campaign previously conducted in the laboratory on a research PEM fuel cell stack (Lipartiti 2022).

III.3.1 Experimental data acquisition

The tested stack is the H-100 Research PEM fuel cell stack produced by Horizon Technologies: it is an open-cathode, self-humidified, semi-integrated PEM fuel cell stack of 20 cells with 22.5 cm^2 cross-sectional area, and 100

W as maximum power exploitable by the stack. The stack comes with a purging valve, normally closed, for automated and manual purging operations; for humidification, a short-circuit unit is present to induce instantaneous water generation inside the cells. The stack is also provided with an external blower for air feeding and cooling purposes. The stack can be managed with the proprietary control unit, powered by an external voltage source: the thermal management is ensured by controlling the blower voltage; on the other hand, the water management is performed periodically through purging and short-circuiting operations at fixed frequencies (Horizon Technologies 2023a). A photograph of the stack extracted from the user manual is presented in Figure III.2.



Figure III.2 *H-100 PEM fuel cell stack, by Horizon Technologies.*

A more detailed insight is provided in Table III.2, with the main technical features extracted from the stack's user manual.

In Figure III.3, the voltage and power curves with respect to stack current, as declared by the manufacturer, are reported with blue and red lines, respectively.

The single cell performances are characterised by single cell voltage, defined as the ratio between stack voltage and cells number (under the hypothesis of single cell approach), and current density, defined as the ratio between current and cross-sectional area. The polarisation curve of the single cell for this stack is represented in Figure III.4.

It can be noted that this type of fuel cell reaches a lower maximum current density compared to other technologies that can exploit limiting current densities greater than 1 A/cm^2. This behaviour can be explained by considering that the stack is open-cathode: unlike closed-cathode cells, the amount of air is

Table III.2 *H-100 datasheet, by Horizon Technologies.*

Parameter description	**Value (Units)**
Type of cells	PEM (−)
Number of cells	20 (−)
Cross-sectional area	22.5 (cm^2)
Humidification	Self (−)
Cooling	Air (−)
Rated power	100 (W)
Rated performance	12 @ 8.3 (V @ A)
Rated efficiency	40 (%)
Hydrogen flow rate at max power	1.3 (Nl/min)
Hydrogen inlet pressure	1.45-1.55 (bar)

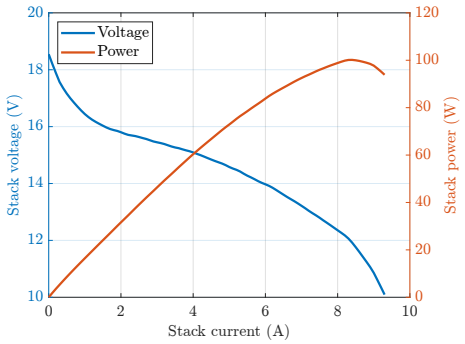


Figure III.3 *H-100 voltage-current curve (blue line) and power-current curve (red line), adapted from ref. (Horizon Technologies 2023a).*

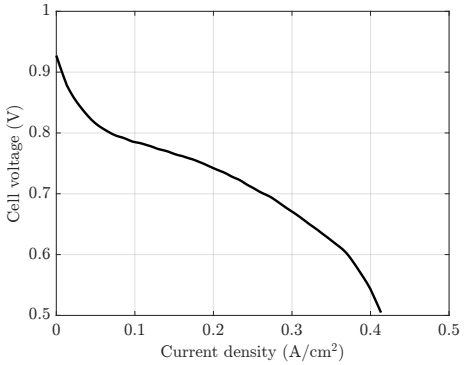


Figure III.4 *H-100 single cell polarization curve.*

significantly greater than the stoichiometric quantity needed, as the air serves both for reactant supply and cooling purposes. The high excess air ratio can cause a severe drying condition, thereby limiting the maximum current density; this can also explain the need for a short-circuit unit for self-humidification.

The H-100 is tested on the PEMFC experimental test bench available at the Energy and Propulsion Systems Laboratory at the University of Salerno. A photograph of the PEMFC test rig is available in Figure III.5.



Figure III.5 *PEMFC test bench at the Energy and Propulsion Systems Laboratory, University of Salerno.*

The test bench is equipped for open-cathode fuel cell testing with the following components: (i) mass flow controller for hydrogen fuelling; (ii) air flow stabilisation duct; (iii) air flow sensor; (iv) DC current-controlled electrical load; (v) stack temperature sensor. The hydrogen mass flow controller is the Alicat MC-2SLPM tared for hydrogen, with a range from 0.5% up to 100% full scale equal to 2 Slpm, ±(0.8% reading + 0.2% full scale) accuracy, installed upstream of the stack. The air probe is the Air Velocity Transducer 8455 produced by TSI, with a range from 0.125 to 10 m/s, ±0.2 accuracy, 0.07% full scale resolution, installed 1 meter far from the stack inside the stabilisation duct. The electronic load is the Keithley 2380-120-60 used in constant current mode, with a range from 0 to 6 A, a resolution of 0.1 mA, and an accuracy of ±(0.05% reading + 0.1% full scale) accuracy; the voltage measure range is 0-18 V with a resolution of 0.1 mV and ±(0.025% reading + 0.025% full scale) accuracy. The temperature measurement is achieved with a NTC voltage divider temperature sensing electrical circuit, with a 10 kΩ resistor and ±5% tolerance. The test bench is managed with a LabVIEW dedicated interface in order to collect the measured variables and to command the desired stack current and hydrogen flow, with a closed-loop control. In Figure III.6, the schematization of the PEMFC test bench is reported with the main components highlighted.

For the experimental campaign, the following setup is contemplated: (i)

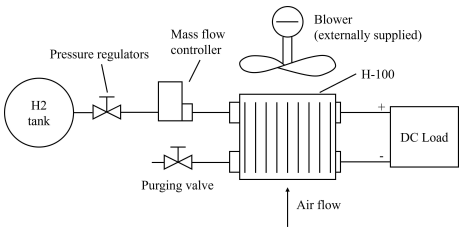


Figure III.6 *Schematic of the PEMFC test rig facility.*

closed purging valve; (ii) current-controlled operations; (iii) step ramps, with 10 minutes for relaxation; (iv) fixed blower voltage. In addition, the proprietary controllers are disconnected from the system: the short-circuit unit is not present, while the purging valve is kept closed during all operations to avoid severe drying conditions.

For the testing phase, the controlled current is chosen as the main input to the system: after a first starting phase of roughly 45 minutes, step-up and step-down ramps are imposed to cell, with current ranging from 0 to 5 A with 1 A delta step. Every step is maintained for 10 minutes to ensure steady-state conditions. The mass flow controller feeds the stack the stoichiometric amount of hydrogen with an additional bias to overcome eventual spillage or crossover issues. The blower voltage is kept at fixed 13 V. In Figure III.7, the current trajectory induced over time to the PEMFC stack is represented.

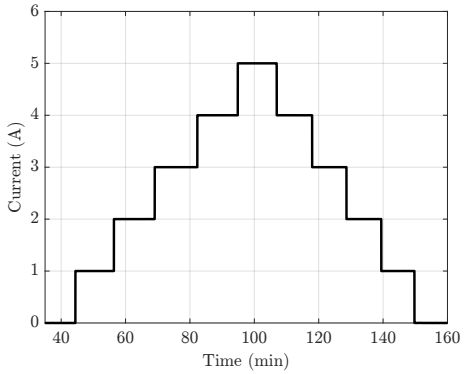


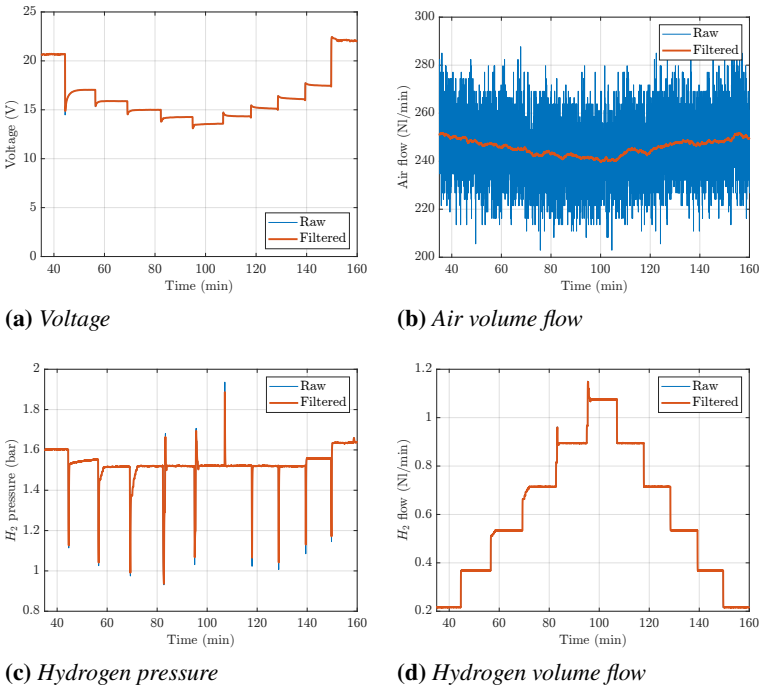
Figure III.7 *Actual controlled current profile over time.*

The measurement acquisition frequency is fixed at 1 Hz. The measured stack variables are voltage and temperature; for the reactant gases, air flow is measured, while flow and pressure are collected for hydrogen line. To address measurement noises, exponential moving average filters are implemented; the tuning of filter coefficients is empirical, based on signal shape and expected

results. The following general formulation is applied for every measured signal:

$$y^n_{filt} = \alpha_{filt} y^n + \left(1 - \alpha_{filt}\right) y^{n-1}_{filt} \tag{III.75}$$

where y^n is the n-th original signal value, y^{n-1}_{filt} and y^n_{filt} are, respectively, the previous and actual filtered signal values, and α_{filt} is the filter weight. The exponential filtering treatment involved voltage, hydrogen flow, hydrogen pressure, and air flow. In Figure III.8, the comparison between the original data, plotted with blue lines, and the filtered data, shown with red lines, is reported.



(a) *Voltage*

(b) *Air volume flow*

(c) *Hydrogen pressure*

(d) *Hydrogen volume flow*

Figure III.8 *Comparison between raw (blue line) and filtered (red line) experimental data, with exponential filters.*

The voltage measured shows typical trends of fuel cells when subjected to step current variation: when the current increases, undershooting voltage happens due to slow humidification increase; when the current decreases, overshooting voltage shows since the stack slowly dries. The hydrogen pressure measured by the mass flow controller follows the hydrogen supply: when more hydrogen is consumed by the stack at high currents the pressure slightly decreases, sign of high consumption. The hydrogen flow correctly follows the current profile; the air flow, on the other hand, exhibits a lot of noise requiring a low filtering coefficient, even if the average air flow is mostly maintained

during all testing duration.

The temperature raw data shows excessive measurement noise: a filter that is too strong would cause the dynamics to disappear, whereas a filter that is too weak would not be able to eliminate enough noise. Hence, a different filtering approach is followed. For every current step, the steady-state temperature is calculated as the numerical integral average of the last 70% data portion; to preserve data dynamics, a first order dynamic is assumed between every step:

$$T_{filt}(t) = T_{SS} + (T_0 - T_{SS})\, e^{-\frac{t}{\tau}} \tag{III.76}$$

where T_{SS} is the steady-state temperature of the given time interval, T_0 is the previous temperature before current variation, and τ is a time constant representative of this dynamic. The time constant has been identified for all current steps minimising the RMSE between raw data and filtered data, choosing an average value at the end. The comparison between raw and filtered temperature is reported in Figure III.9.

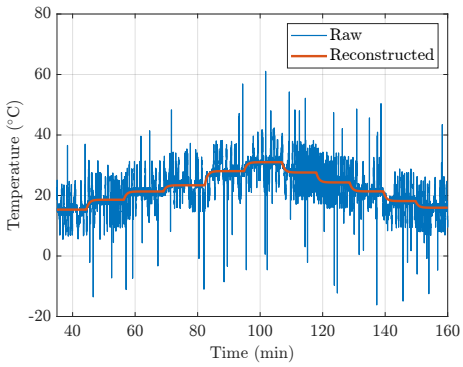


Figure III.9 *Comparison between raw (blue line) and reconstructed (red line) measured temperature, with model-based filter.*

From the filtered data it is also possible to extract the steady-state reference data for every current value, needed for model steady-state validation. To extract the steady-state value, the numerical trapezoidal integral average is implemented:

$$y_{ss} = \frac{1}{t^N - t^1} \sum_{n=1}^{N-1} \frac{y^{n+1} + y^n}{2} \left(t^{n+1} - t^n\right) \tag{III.77}$$

where y_{ss} is the actual steady-state value, $t^N - t^1$ is the time span of the numerical integral, $t^{n+1} - t^n$ is the actual time-step, and $\frac{y^n + y^{n+1}}{2}$ is the average between the n-th and successive steps. The time span is the last 40% portion of the total number of measures, in order to exclude every initial dynamic after

the current variation. The final steady-state average data is obtained as the arithmetical average between up-step and down-step corresponding variations. In Figure III.10, the final data set for steady-state validation is shown for stack voltage and current, hydrogen pressure and flow, and air flow for every current value.

Analysing the steady-state flows, it can be noted that the air excess ratio range is 93-483: this is consistent with the open-cathode typology of this PEMFC stack.

III.3.2 Steady-state validation

The steady-state validation of the model is performed by comparing the polarisation curve resulting from the model and comparing the results with steady-state experimental data. To perform an adequate validation process, the model is run for 1000 seconds with fixed boundary conditions for every current value, from 0 to 5. The temperature is kept constant equal to the experimental one, as well as hydrogen pressure and gases flow. In Figure III.11, the steady-state validation procedure results are reported: on the left, the comparison between experimental and model datasets is shown; on the right, the experimental-predicted graph is plotted for better comparison.

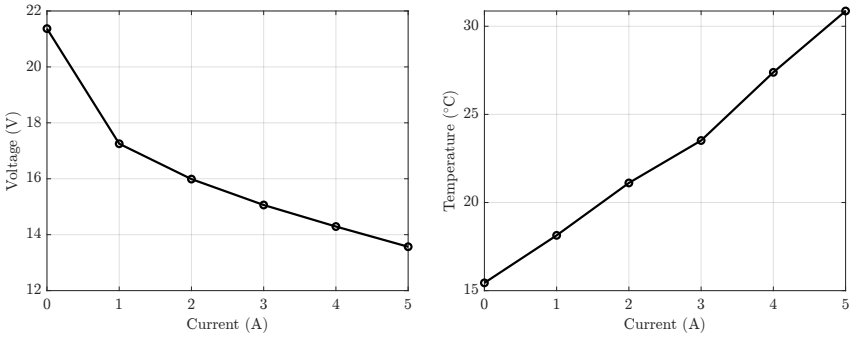
The results show the optimal correlation between model and experimental data: the polarization curve is well fitted by the model, as also confirmed by the experimental-predicted plot. To deepen the validation process, in Table III.3 the most relevant statistical parameters are calculated and collected.

Table III.3 *Model steady-state validation statistical analysis.*

Parameter description	**Value (Units)**
Root Mean Square Error (RMSE)	0.0802 (V)
Mean Absolute Percentage Error (MAPE)	0.4451 (%)
Correlation factor (R^2)	0.9998 (−)

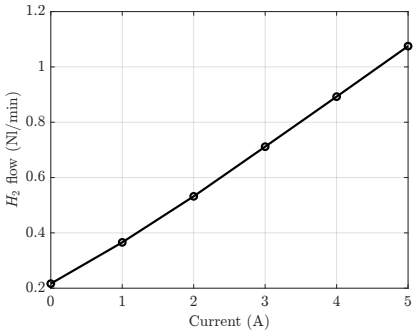
As it can be seen, every statistical parameter confirms the good performance of the model to reproduce experimental data. The RMSE is lower than 0.1 V, corresponding to around 0.5% of the average stack voltage: the modelled polarisation curve properly fits the experimental data-set, with low error on average. The Mean Absolute Percentage Error (MAPE) statistic is also lower than 1%: this shows the goodness of model results at both low and high values of voltage. Finally, the R^2 correlation factor shows optimal correlation between experimental and model data, as also confirmed by Figure III.11.

A deepen voltage analysis is shown in Figure III.12, in which the different

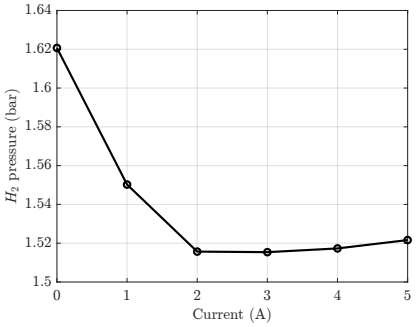


(a) *Voltage*

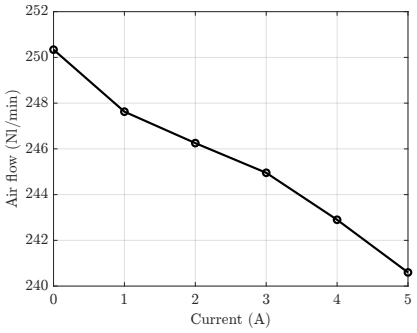
(b) *Temperature*



(c) *Hydrogen flow*

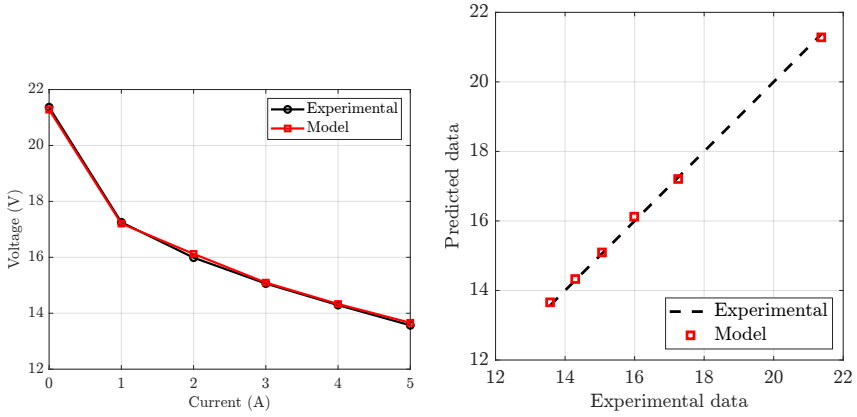


(d) *Hydrogen pressure*



(e) *Air flow*

Figure III.10 *Collection of steady-state data after filtering and integral average processes as function of current, acquired at the test bench.*



(a) *Polarisation curve comparison* **(b)** *Experimental-predicted squared plot*

Figure III.11 *Model steady-state validation with respect to experimental data.*

components of polarisation curve for the single cell, identified with a different colour, are depicted for every current value.

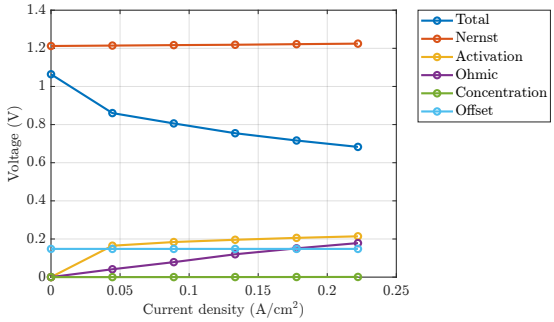


Figure III.12 *Single cell voltage analysis for every term of polarization curve: total (blue); Nernst potential (red); activation losses (yellow); Ohmic losses (purple); concentration losses (green); offset losses (cyan).*

The results analysis shows a little increase in the Nernst potential, correlated with the gradual temperature increase with the stack current. Ohmic losses are almost linear with current density, indicating that the Ohmic resistance does not change significantly. The concentration losses are negligible, since the current density does not reach limiting current density at all.

In Figure III.13, the values of water content for the membrane (black line with circles), the anode catalyst layer (red line with squares), and the cathode catalyst layer (blue line with triangles) are reported for every current step.

As it can be seen by the results, it is confirmed that this type of open-cathode stack is quite dry on average: the membrane water content does not get higher

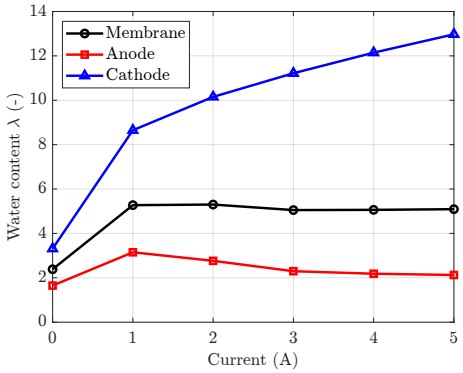
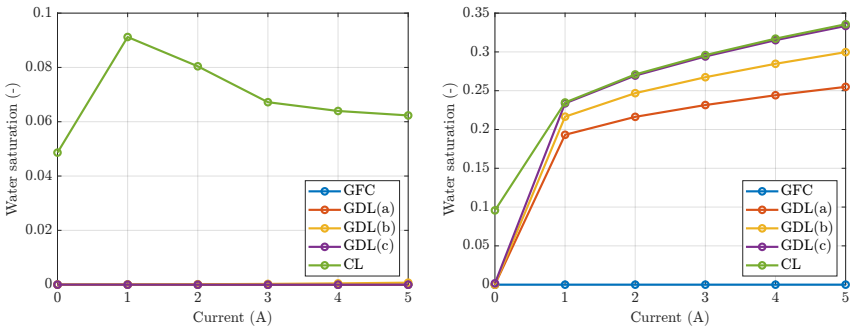


Figure III.13 *Water content values varying current for membrane (black, circle), anode (red, square), and cathode (blue, triangle).*

than 5, stabilising around this value at high current. The anode is dryer than the membrane, even if at low currents there is a slighter increase in water content thanks to diffusion effect; the cathode CL is sufficiently humidified, and the water content increases with current thanks to water generation. These trends are confirmed by looking at Figure III.14, in which the water saturation values for both anode (left) and cathode (right) are reported for every sub-volume with different line colours according to the legend.



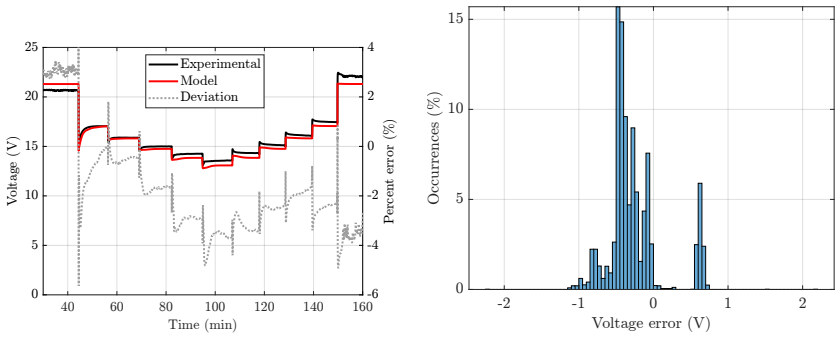
(a) *Anode volumes* **(b)** *Cathode volumes*

Figure III.14 *Water saturation values varying current for anode (left) and cathode (right) in the different sub-volumes: GFC (blue); GDL-a (red); GDL-b (yellow); GDL-c (purple); CL (green).*

The anode is confirmed to be dry from liquid water for every sub-volume except the catalyst layer. The cathode, on the other hand, exhibits liquid water in all volumes except GFC because of water expulsion outside the cell and higher water evaporation due to higher volume availability.

III.3.3 Dynamic validation and analyses

The dynamic validation of the model is addressed comparing both stack voltage and temperature between experimental dataset and model results. The model is run with only boundary conditions equal to experimental ones, estimating voltage and temperature. In Figure III.15, the comparison between experimental and modelled stack voltage is reported: on the left, the two time profiles are compared with black and red lines, respectively, while on the right the error distribution is shown.



(a) *Time profiles evolution* **(b)** *Error distribution histogram*

Figure III.15 *Voltage dynamic validation with respect to experimental data.*

It can be seen that the results obtained are satisfactory: the model is able to reproduce consistently the voltage all over the experimental campaign, capturing essential dynamics with low error on average. However, it can be observed that, even if almost 40% of the error occurrences is almost zero, some outliers are visible, especially in warm-up and zero current phases. This can be explained considering that the model considers the physical and chemical properties of the stack as nominal with no consequences on cells behaviour, especially in the first phases, when the stack should also be preliminary purged and humidified for better performance. Furthermore, the BoP is not taken into account, with no modelling of external manoeuvres. A deepen analysis is performed calculating the statistical Key Performance Indicator (KPI)s, reported in Table III.4: the outliers referred to error residuals higher than 20 V, corresponding to the first instants of stack warm-up, are excluded.

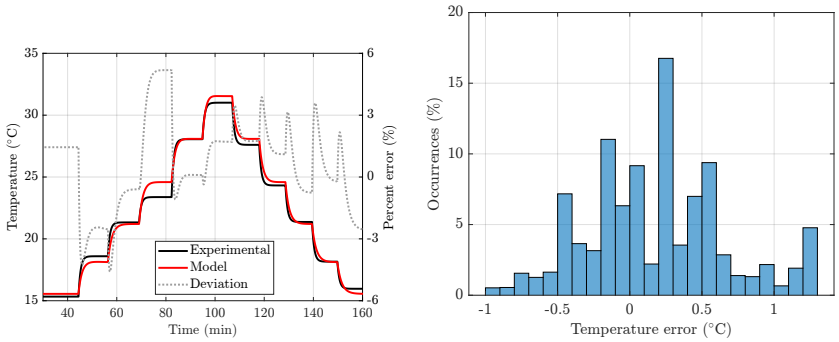
Every statistical parameter confirms the accuracy and robustness of the model: the results obtained in terms of stack voltage are adherent and coherent with the experimental data, with an average error of 2.5%

In Figure III.16, the comparison between the experimental and modelled stack temperature is reported: on the left, the two time profiles are compared with black and red lines, respectively, while on the right the error distribution

Table III.4 *Voltage model dynamic validation statistical analysis.*

Parameter description	Value (Units)
Root Mean Square Error (RMSE)	0.4851 (V)
Mean Absolute Error (MAE)	0.4385 (V)
Mean Absolute Percentage Error (MAPE)	2.5043 (%)
Standard Deviation of Residuals (SDR)	0.4713 (V)
Correlation factor (R^2)	0.9844 (−)

is shown.



(a) *Time profiles evolution* **(b)** *Error distribution histogram*

Figure III.16 *Temperature dynamic validation with respect to experimental data.*

The comparison between the two temperature profiles confirms the consistency of the model for the entirety of the experimental campaign: the majority of residuals is around 0.25°C, with 25% of the occurrences. However, some outliers can be observed: these can be neglected, since the original temperature measure is reconstructed due to a signal too noisy. For further analysis, The statistical KPIs of the temperature analysis is reported in Table III.5.

The statistical parameters are optimal also for the temperature estimation, with a low error both on punctual and average. The correlation between the two datasets is higher than 0.99, confirming the predictability of the proposed model.

A deepen voltage analysis is shown in Figure III.17, in which the different components of polarisation curve for the single cell, identified with a different colour, are depicted during experimental campaign.

Consistently with the steady-state analysis, the trends presented here are similar: the main voltage losses are activation and Ohmic ones, with a bias due to the offset losses. The concentration losses are still neglectable.

Table III.5 *Temperature model dynamic validation statistical analysis.*

Parameter description	**Value (Units)**
Root Mean Square Error (RMSE)	0.4696 (°C)
Mean Absolute Error (MAE)	0.3633 (°C)
Mean Absolute Percentage Error (MAPE)	1.7249 (%)
Standard Deviation of Residuals (SDR)	0.4334 (°C)
Correlation factor (R^2)	0.9942 (−)

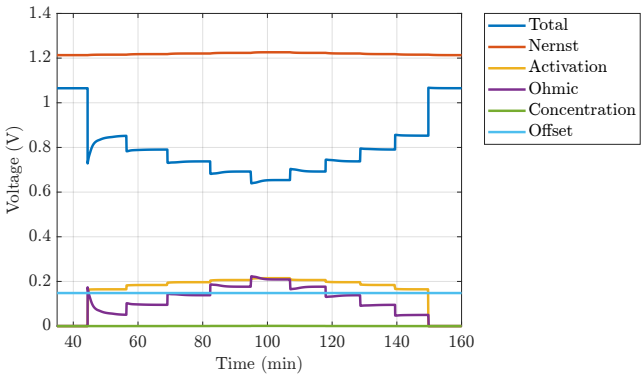


Figure III.17 *Single cell dynamic voltage analysis for every term of polarization curve: total (blue); Nernst potential (red); activation losses (yellow); Ohmic losses (purple); concentration losses (green); offset losses (cyan).*

In Figure III.18, the values of water content for the membrane (black line), the anode catalyst layer (red line), and the cathode catalyst layer (blue line) are reported.

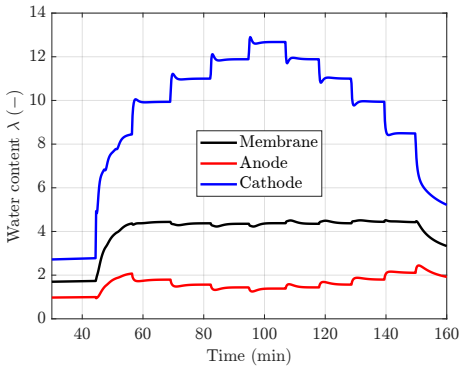
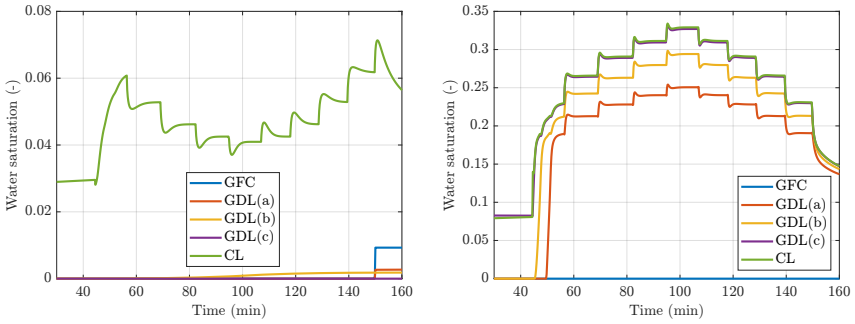


Figure III.18 *Water content values in time for membrane (black), anode (red), and cathode (blue).*

After a first stabilisation phase, it is interesting to observe that the membrane average water content is quite constant slightly higher than 4. The cathode catalyst layer shows the higher water content variation with current as expected, while on the anode side a drying process occurs related to current magnitude. Similar considerations can be made looking at water saturation values reported in Figure III.19, in which the water saturation for both anode (left) and cathode (right) is reported for every sub-volume with different line colours according to the legend.



(a) *Anode volumes* **(b)** *Cathode volumes*

Figure III.19 *Water saturation profiles in time for anode (left) and cathode (right) in the different sub-volumes: GFC (blue); GDL-a (red); GDL-b (yellow); GDL-c (purple); CL (green).*

The anode is critically dry, since no water is added with inlet hydrogen and

a general advection trend, except at the end of the simulation when there is no electro-osmotic drag and the diffusion mechanism can suddenly redistribute water also towards anode. The cathode is more humidified on average: there is liquid water in every volume, except for the GFC.

III.3.4 Computational performance

The presented model is tested on a 11th gen Intel Core i7-1165G7 @2.8 GHz machine. The model numerical solver is a stiff variable-step, variable-order scheme implemented in MATLAB/Simulink environment, with a total computational time of 170.57 seconds. Considering the experimental campaign duration of 9'633.88 seconds, the final computational speed is 56.48: the model is able to reproduce the real stack 56 times faster than real-time.

III.4 Conclusions

In this chapter, a mathematical model for PEMFC stack water management is presented. Based on literature, a mathematical model is developed to account all transport mechanisms inside the porous electrodes: furthermore, a dynamic analytical model for water membrane content is implemented to precisely define the water membrane content in transient and steady-state conditions; the water removal rate is approximated as a modified Bernoulli flow. The model validation is performed with experimental data available of a commercial PEMFC open-cathode stack of 100 W maximum power: the stack is tested with a current step-up ramp to analyse stack step response in terms of voltage and temperature. The model exhibits an average error of 0.5% in steady-state conditions for the polarisation curve, demonstrating the model consistency and correlation with experimental data. In transient conditions, the voltage error distribution is narrow around zero apart from a little portion of outliers, with an average error of 2.5%; the temperature error distribution is quite flat with 25% occurrences at 0.25°C and 1.7% average error. The model is 50 times faster than real time, confirming that it is suitable for real-time control and monitoring applications, in which the water membrane content should be estimated to proper diagnose and control the PEMFC stack to optimize its performances.

Future developments of this work include more detailed water removal models, implementing droplets behaviour to further characterise the water removal processes. In addition, the model as it is can also be integrated in a BoP system model, to complete the plant description reaching more agreement with experimental data.

Chapter IV
Hydrogen-fuelled hybrid vehicle modelling for optimal control strategy design and simulation

Hydrogen is a promising solution for vehicle hybridisation. For this scope, in this chapter, a mathematical model of a pure electric native vehicle with a hydrogen-powered range extender is developed and presented, from powertrain components to control strategies. This activity also represents the opportunity to carry out a downsizing design phase of the battery pack in favour of the use of hydrogen. In this way, energy analyses are carried out to consider the effect on the hybridisation of a real electric vehicle. This activity is part of the HySuM project (Hybrid Sustainable Mobility Platform), funded by the Italian Ministry of University and Research under the call PRIN 2020.

IV.1 Electrical vehicle modelling approach

Within the framework of the PRIN project, the electrical vehicle subjected to hydrogen hybridisation is called "Tritone", produced by OPV Mobility. Tritone is a lightweight electric vehicle, L6e class, powered by four in-wheel motors with a nominal power of 2 kW each, regenerative braking capability, 1:1 gear ratio with wheels, with a declared range of 100 km on 100% battery discharge tested on the World Motorcycle Test Cycle (WMTC) drive cycle. A picture of Tritone is reported in Figure

From the manufacturer website, in Table the available technical data sheet is reported (OPV Smart Urban Mobility 2023).

The four Electric Motor Generator (EMG)s are all AC machines; hence, inverters are needed to manage the DC/AC switch between battery and each motor. The four machines are connected in parallel, sharing the same fixed voltage of 48 V: because of this, a general DC/DC converter manages the voltage ensuring that every motor is fed with the nominal voltage of 48 V. A



Figure IV.1 *Tritone vehicle, by OPV Mobility.*

Table IV.1 *Tritone data sheet, adapted from manufacturer data (OPV Smart Urban Mobility 2023).*

Parameter description	**Value (Units)**
Vehicle payload without battery	425 (kg)
In-wheel motor rated power	2 (kW)
In-wheel motor nominal voltage	48 (V)
Battery nominal capacity	5.1 (kWh)
Battery nominal voltage	48 (V)

simple schematisation of the electrical powertrain is provided in Figure IV.2.

To pursue the model-based design modelling approach, it is possible to assume that every motor behaves identically: this hypothesis paves the way to summarise the modelling of the four motors as a unique equivalent EMG able to satisfy the entire power request by the driver. The equivalent EMG is represented with the efficiency map that also includes the inverter's conversion efficiency. In Figure IV.3, the final schematisation of vehicle components with energy flows is reported.

The model is developed with a backward approach: it is assumed that the vehicle speed is always instantaneously satisfied, so that the electrical power required is computed climbing up the efficiency chain from road to battery. This modelling approach is needed to develop optimal control strategies for hybrid configurations; however, the main drawback is that every dynamic behaviour of non-state variables is not accounted.

IV.1.1 Road load identification

The road load mechanical power is the first unknown of the energy chain: the vehicle longitudinal dynamics equation is implemented to address this computational step. The main forces acting on the vehicle, projected on motion

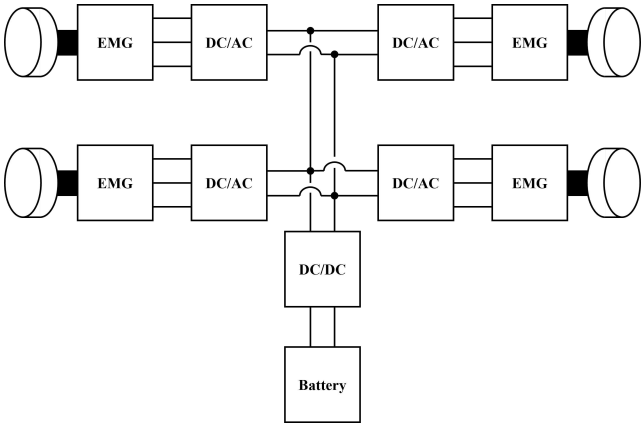


Figure IV.2 *Electrical powertrain scheme, with main components highlighted.*

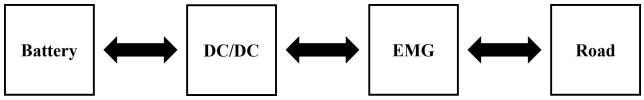


Figure IV.3 *Model schematisation of the original pure EV vehicle.*

longitudinal direction, are the following: (i) inertia; (ii) aerodynamic drag; (iii) rolling resistance; (iv) weight longitudinal projection; (v) driving/braking forces. The vehicle is considered as a point mass, with every force applied on vehicle's center of mass. The forces schematisation is shown in Figure IV.4.

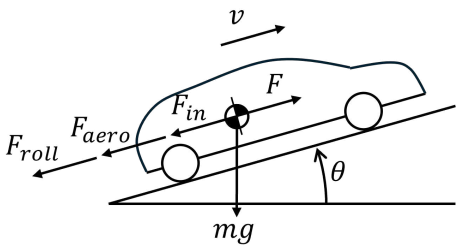


Figure IV.4 *Longitudinal vehicle dynamics model scheme, with main forces highlighted.*

The corresponding forces balance on the longitudinal direction is the following:

$$F = F_{in} + F_{aero} + F_{roll} + mg \sin\theta \tag{IV.1}$$

where F is the driving/braking force due to motors action, F_{in} is the inertial force, F_{aero} is the aerodynamic drag, F_{roll} is the rolling resistance, and $mg \sin\theta$

is the longitudinal projection of mg weight. The inertial force can be calculated considering the vehicle equivalent mass:

$$F_{in} = M_{eq}\frac{dv}{dt} \tag{IV.2}$$

where M_{eq} is the total equivalent mass, i.e., sum of weight and rotational inertias, while v is the vehicle speed. The aerodynamic drag is calculated from the drag coefficient, extrapolated from the work by Benzing (2004):

$$F_{aero} = \frac{1}{2}\rho_{amb}C_x A_f v^2 \tag{IV.3}$$

where ρ_{amb} is the ambient air density, C_x is the drag coefficient, and A_f is the frontal cross-sectional area of the vehicle. The rolling resistance is influenced by weight force normal projection through the rolling coefficient, extrapolated from the literature (Mahapatra et al. 2021):

$$F_{roll} = mgC_r\,(v)\cos\theta \tag{IV.4}$$

where $C_r\,(v)$ is the rolling resistance coefficient as a polynomial expression of vehicles speed. The final power road load can be computed as follows:

$$P_{load} = Fv \tag{IV.5}$$

Considering the aerodynamic drag, the rolling resistance and weight with different road slopes and zero acceleration, the mechanical power load is graphed in Figure IV.5.

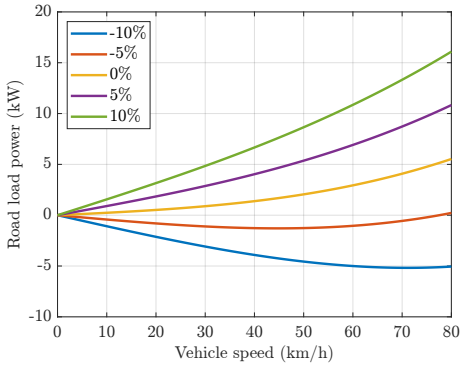


Figure IV.5 *Road load power requirement as function of speed, from -10% to 10% road slope.*

IV.1.2 In-wheel motor modelling approach

The available specifications of the EMGs are only the maximum power and the nominal voltage. Neglecting machine dynamics (it is assumed that the motors dynamics are orders of magnitude faster than the rest), a map-based approach is followed in order to determine the efficiency of the motors as function of torque and speed. To build the efficiency map without knowing any characteristic of the motors, the Willans lines approach is considered to scale down the efficiency map of another similar electrical machine (Guzzella and Sciarretta 2013); the reference electrical machine is the one presented in the work of Upadhayay et al. (2018). Following the Willans lines approach, the electrical machine power balance in traction mode can be written as follows:

$$T_m \omega_m = e P_{el} - P_{loss} \tag{IV.6}$$

where T_m is the traction torque, ω_m is the rotor speed, e is the indicated efficiency not accounting for friction, and P_{loss} are the mechanical losses. This power balance can be also written in terms of specific variables, i.e., mean pressures, to exclude geometrical effects:

$$p_{me} = e p_{ma} - p_{mf} \tag{IV.7}$$

where p_{me} is the effective mean pressure, p_{ma} is the available mean pressure, and p_{mf} is the friction mean pressure. The specific variables are calculated as follows:

$$p_{me} = \frac{T_m}{2V_r} \tag{IV.8}$$

$$p_{ma} = \frac{P_{el}}{2V_r \omega_m} \tag{IV.9}$$

$$p_{mf} = \frac{P_{loss}}{2V_r \omega_m} \tag{IV.10}$$

where V_r is the rotor volume. The indicated efficiency and friction pressure are tuned to minimise the effective mean pressure between eq. (IV.7) and the literature data (Upadhayay et al. 2018): the obtained tuned model shows a final correlation coefficient R^2 equal to 0.99973. The EMG efficiency in motor mode is defined as follows:

$$\eta_m = \frac{T_m \omega_m}{P_{el}} \tag{IV.11}$$

To calculate the EMG efficiency in generator mode, it is assumed that the power losses are equal between quadrants, picking the corresponding traction

efficiency as shown below:

$$\eta_g = 2 - \frac{1}{\eta_m\left(\omega_m, |T_m|\right)} \tag{IV.12}$$

The final efficiency map of the single EMG, considering also the maximum torque envelope curves and a regeneration factor equal to 0.7, is finally shown in Figure IV.6 as a contour map, with the main iso-efficiency lines highlighted, as function of rotor speed and torque.

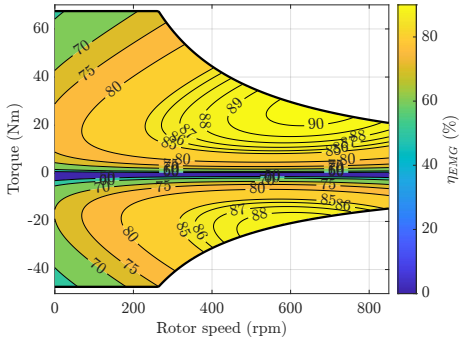


Figure IV.6 *EMG efficiency contour map in both traction and generation quadrants.*

Considering the equivalent machine assumption, from road load the electrical power requirement for the single EMG can be evaluated as follows:

$$P_m = \frac{P_{load}}{4} \tag{IV.13}$$

IV.1.3 DC/DC converter behavioural model

The DC/DC converter is an electronic circuit made of several switches and inductors: the frequency of switches' actions defines the ratio between source voltage and output voltage. The duty cycle timing is orders of magnitude lower than other characteristic times involving the powertrain; hence, for this modelling approach a behavioural model with an equivalent circuit is preferred to represent the main DC/DC converter, in order to avoid model stiffness. The equivalent circuital model is sketched in Figure IV.7.

The DC/DC converter is modelled as two separate circuits, with a fixed power absorption and an internal resistance. The left circuit, corresponding to

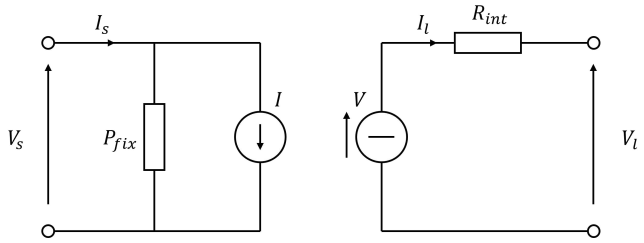


Figure IV.7 *Equivalent circuit model of the DC/DC converter.*

source side, can be described applying Kirchhoff law as follows:

$$I = I_s - \frac{P_{fix}}{I_s} \tag{IV.14}$$

where I_s is the source current, V_s is the source voltage, and P_{fix} is the fixed power absorption. On the right side, the following circuital balance is obtained:

$$V = V_l + R_{int} I_l \tag{IV.15}$$

where V_l is the load voltage, I_l is the load current, and R_{int} is the equivalent internal resistance. The two semi-circuits share electrical power:

$$V_s I = V I_l \tag{IV.16}$$

Combining the two equations (IV.14) and (IV.15) into eq. (IV.16), the following power balance is obtained:

$$P_s = P_{fix} + P_l + R_{int} \left(\frac{P_l}{V_l} \right)^2 \tag{IV.17}$$

For this application, the voltage load is set to 48 V, according to EMGs nominal voltage (Table IV.1). The fixed power absorption and the internal resistance are calibrated to ensure 90% efficiency at nominal voltage with maximum load power. The DC/DC converter efficiency in discharging operations, in which the energy flows from source to load, is easily defined:

$$\eta_{DC}^{s \to l} = \frac{P_l}{P_s} \ (P_l \geq 0) \tag{IV.18}$$

On the other hand, the converter efficiency in charging operations, when regenerative braking occurs, is defined as the inverse:

$$\eta_{DC}^{l \to s} = \frac{P_s}{P_l} \ (P_l < 0) \tag{IV.19}$$

In Figure IV.8, the efficiency curve as function of transmitted power is reported, with solid line for discharging mode and dashed line for charging mode. The transmitted power is intended both as load power, when energy flows from source side to load side, and source power, when energy flows from load side to source side.

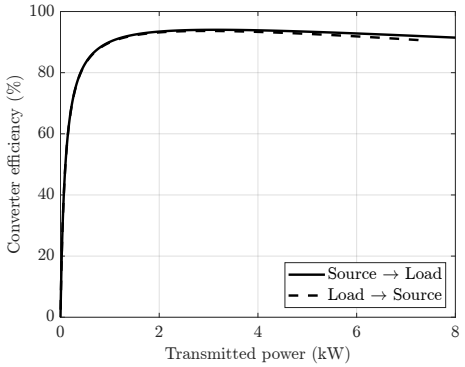


Figure IV.8 *DC/DC converter efficiency as function of transmitted power in discharging mode (solid line) and charging mode (dashed line), at 48 V.*

IV.1.4 Battery quasi-static model

The battery stack of the vehicle consists in four modules connected in parallel; each module is further composed by 112 single battery cells, arranged as 14 series and 8 parallel groups. It is assumed for similar cell characteristics that the vehicle battery cells have the same discharge curve as the LGMH1 18650 cell produced by GWL Group (2023). To model the entire stack, it is assumed that every cell behaves the same, with equal discharge curves and state-of-charge. The single battery cell can be modelled following a quasi-static approach with a simple equivalent circuit as shown in Figure IV.9, in which the cell voltage depends on open-circuit voltage and internal resistance, both functions of SoC.

The open-circuit voltage and the internal resistance of the single cell are identified from the literature data (GWL Group 2023) with polynomial interpolations with respect to battery SoC, minimising the error between model and reference cell voltage. The identification process leads to a final correlation factor R^2 equal to 0.98915.

Considering the battery stack arrangement, it is possible to model the battery stack with the same circuital representation of Figure IV.9 scaling the cell open circuit voltage and the cell internal resistance applying the Thevenin and Norton equivalent circuit laws. Following this process, the battery stack can be

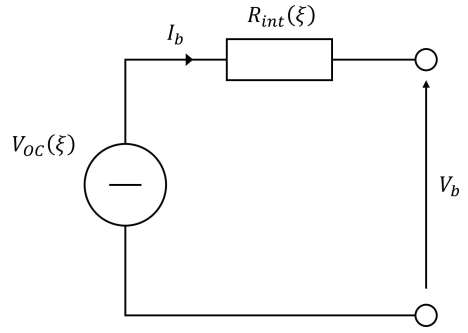
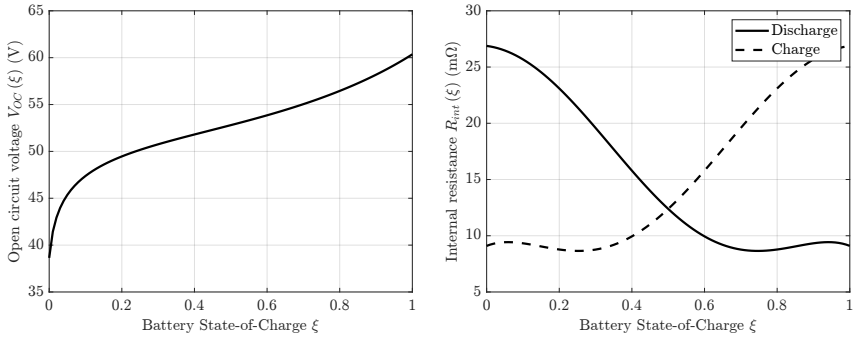


Figure IV.9 *Battery cell equivalent circuital model scheme.*

represented with the following equation:

$$V_b = V_{OC}\,(\xi) - R_{int}\,(\xi)\,I_b \tag{IV.20}$$

where ξ is the battery SoC, V_b is the battery voltage, I_b is the battery current, while V_{OC} and R_{int} are the equivalent open-circuit voltage and internal resistance of the stack. In Figure IV.10, the final values of open-circuit voltage (left) and internal resistance (right) of the battery stack are reported. The battery internal resistance is represented in both discharging and charging phases, with solid and dashed lines respectively: the charging internal resistance is assumed equal but reflected to the discharing internal resistance.



(a) *Open-circuit voltage* **(b)** *Internal resistance*

Figure IV.10 *Battery stack equivalent open-circuit voltage (left) and internal resistance (right) as function of battery SoC (Cervone, Sicilia, Romano, et al. 2023).*

The battery SoC ξ is a state variable that depends on battery current. From battery stack power, the current can be calculated inverting the Kirchhoff law

to the circuital model:

$$I_b = \frac{V_{OC}(\xi) - \sqrt{V_{OC}^2(\xi) - 4R_{int}(\xi) P_b}}{2R_{int}(\xi)} \tag{IV.21}$$

where P_b is the battery power. The battery state equation is derived assuming that the instantaneous SoC rate is directly proportional to the current as follows:

$$\frac{d\xi}{dt} = -\frac{I_b}{Q} \tag{IV.22}$$

where Q is the stack nominal capacity. The efficiency of the battery stack can be calculated as the ratio between the ideal power during discharging over the ideal power during charging as follows (Guzzella and Sciarretta 2013):

$$\eta_b = \frac{V_{OC}(\xi) - R_{int}^{dis} |I_b|}{V_{OC}(\xi) + R_{int}^{chg} |I_b|} \tag{IV.23}$$

For the battery stack of this application, the final efficiency map is reported in Figure IV.11 as function of battery SoC and C-rate between maximum charging current and maximum discharging current.

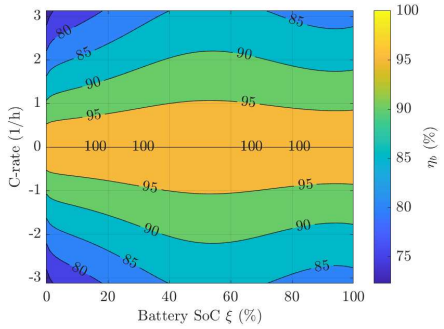


Figure IV.11 *Battery efficiency contour map as function of battery SoC and C-rate.*

IV.1.5 EV range assessment and validation

The range of the pure electric vehicle is assessed with reference to the WMTC-L6 driving cycle limited to a maximum speed of 50 km/h, represented in Figure IV.12: this cycle is looped until the desired discharge of the battery is obtained. This homologation cycle has no information on road slope, assuming

a flat road.

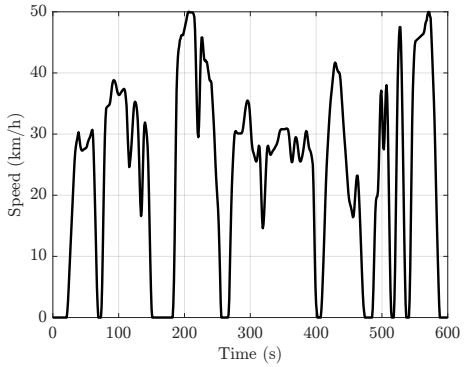


Figure IV.12 *WMTC-L6 standard drive cycle for model range assessment.*

This procedure is followed in accordance with manufacturer declaration, in order to reproduce the vehicle performance in the same conditions as the declared range ones. It is assumed to achieve a discharge of 70% of the battery, from 90% to 20%; the total vehicle range on 100% battery discharge is determined as extrapolation. The battery SoC during simulation with respect to vehicle distance is finally is reported in Figure IV.13.

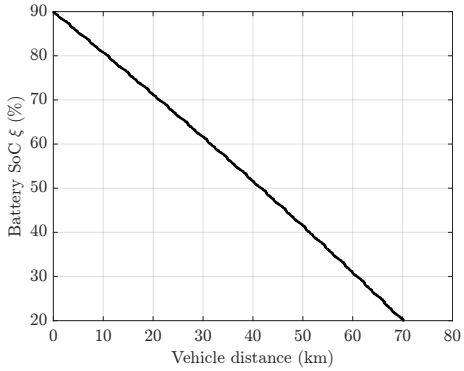


Figure IV.13 *Pure EV configuration model range validation, on WMTC-L6 drive cycle.*

As it can be seen, the modelled vehicle is able to cover 70.196 km on a 90-20% discharge cycle. The declared battery range from the manufacturer is 100 km on a 100% discharge cycle, with 1 %/km discharge rate on average. The proposed model exhibits an average discharge of 1.003 %/km, with a final error of 0.3% on discharge rate confirming the model accuracy on manufacturer data.

IV.2 Hydrogen-fuelled range extender hybridisation

The main objective of the activity is the hybridisation of the original electric vehicle with a hydrogen-based range extender powered with a PEMFC stack, keeping the zero tank-to-wheel emissions. The hybrid layout designed for this scope is a series layout: the vehicle keeps the electrical energy core, while the additional energy is provided by the range extender to improve the reachable distance thanks to the introduction of a DC link. Since the introduction of the Range Extender implies a weight increase, it is assumed to reduce the battery pack from four to three modules, reducing the original battery capacity of 1/4.

Given the original electrical powertrain layout, three hybrid configurations are proposed, based on the position of the DC link and the addition of another DC/DC converter for PEMFC stack.

T3 architecture

Within the T3 architecture, the DC link is inserted after the battery DC/DC converter. The PEMFC stack is connected to the DC link directly, sharing the voltage set by the battery DC/DC converter; to ensure proper working of the stack, an ideal switch is considered to turn off or on the stack based on the control strategy, while an ideal diode is added to avoid back currents. The T3 architecture for this application is shown in Figure IV.14.

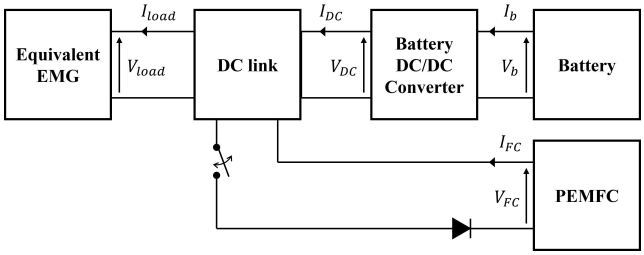


Figure IV.14 *T3 architecture for the proposed electric vehicle hydrogen hybridisation.*

At the DC link, the following voltage and current balances can be written:

$$V_{FC} = V_{DC} = V_{load} \tag{IV.24}$$

$$I_{FC} + I_{DC} = I_{load} \tag{IV.25}$$

The voltage balance confirms that the stack passively works at the voltage set by the battery DC/DC converter, equal to 48 V for this application; hence, the PEMFC stack must be choose with a polarisation curve compatible with

this working point.

T3-bis architecture

In the case of a simple variation of the T3 architecture, the DC link is inserted before the battery DC/DC converter. Similarly to the T3 architecture, there is no additional DC/DC converter: the PEMFC stack is connected directly to the battery, with no components in between. Also in this case, the ideal switch and the ideal diode are present The T3-bis architecture for this application is shown in Figure IV.15.

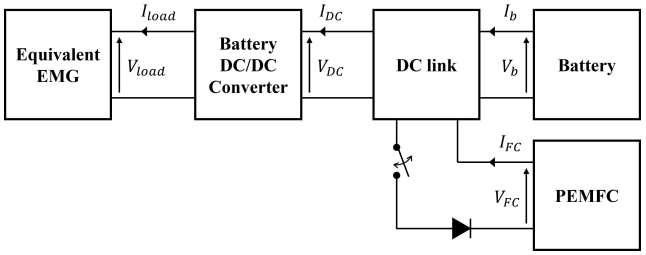


Figure IV.15 *T3-bis architecture for the proposed electric vehicle hydrogen hybridisation.*

At the DC link, the following voltage and current balances can be written:

$$V_{FC} = V_b = V_{DC} \tag{IV.26}$$

$$I_{FC} + I_b = I_{DC} \tag{IV.27}$$

Also in this configuration, the PEMFC works passively. The main difference is that the PEMFC stack follows the battery voltage that depends on battery SoC and power load; hence, the PEMFC voltage curve must be compatible with the battery voltage characteristics. However, differently from the T3 architecture, direct charging mode in which the PEMFC stack feeds the battery is energetically advantageous, since there are no passive elements between the battery and the stack.

T4 architecture

Considering the T4 architecture, the DC link is inserted after the battery DC/DC converter similarly as the T3 architecture. However, the PEMFC stack is connected to the DC link through a proper uni-directional DC/DC converter, freeing the stack from grid voltage. Only the ideal switch is needed to turn off the stack when the control strategy demands it. The T4 architecture for this application is shown in Figure IV.16.

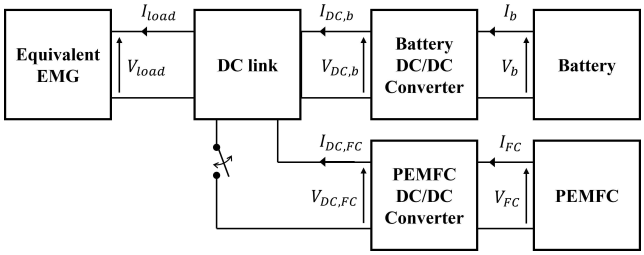


Figure IV.16 *T4 architecture for the proposed electric vehicle hydrogen hybridisation.*

The PEMFC stack voltage V_{FC} is set by the control strategy, thanks to the presence of the PEMFC DC/DC converter: there are no design requirements in this case, giving freedom in stack choice. In this configuration, however, the direct charging mode is the energetically worst between the three proposed architectures, since the electrical energy produced by the stack gets converted two times before feeding the battery.

IV.2.1 Tank sizing

Before detailing the Range Extender (REx), the hydrogen tank needed for fuelling is designed and chosen. The sizing of the hydrogen tank depends on the energy required by the range extender to complete a mission. Thus, a sizing of the hydrogen tank which allows the mileage double with respect to pure Electric Vehicle (EV) configuration with no range extender with full battery discharge. The amount of hydrogen required to cover the doubled distance is assumed equal to the total battery energy amount, corresponding to the nominal capacity, considering the lower heating value of hydrogen and REx average efficiency:

$$\dot{m}_{H_2}^{req} = \frac{Q}{LHV_{H_2}\eta_{REx}^{avg}} \tag{IV.28}$$

where LHV_{H_2} is the hydrogen lower heating value, while η_{REx}^{avg} is the average REx efficiency. Considering an average REx efficiency equal to 30% as the product between stack efficiency and eventual DC/DC converter as worst case scenario, a total amount of 0.51 kg of hydrogen is theoretically required. Hence, a 350 pressurized composite material vessel featured with a capacity of 28 dm^3, a weight of 17 kg and a total storable mass of about 0.6 kg of hydrogen is considered from Steelhead catalogue (Steelhead Composites 2023). A small excess in capacity is considered to ensure that the pressure of the hydrogen tank

does not fall down to the limit of minimum allowable pressure, here assumed as equal to 20 bar for safety. To compute the tank pressure, the filling-emptying model equation assuming an isothermal transformation of a real gas including the compressibility effect as follows:

$$\frac{dp_{H_2}}{dt} = \frac{R_{H_2} T_{tank} V_{tank}}{\left(V_{tank} - B_1 m_{H_2} R_{H_2}\right)^2} \frac{dm_{H_2}}{dt} \tag{IV.29}$$

where R_{H_2} is the hydrogen gas constant, T_{tank} and V_{tank} are temperature and volume of the tank, respectively, while m_{H_2} is the hydrogen amount inside the tank. The B_1 coefficient to introduce compressibility behaviour is equal to $1.9155 \cdot 10^{-6}$ K/Pa, derived from literature (Caponi et al. 2021).

IV.2.2 PEMFC stack modelling

The PEMFC stack chosen for this application is a commercial one produced by Horizon Technologies named "H3000": it is an open-cathode, self-humidified stack with 3 kW as maximum electrical output. This stack has been selected for good voltage compatibility with battery technical limitations and EMGs working voltage. The main technical data needed for modelling are collected in Table IV.2.

Table IV.2 *H-3000 PEMFC stack data sheet, adapted from manufacturer data (Horizon Technologies 2023b).*

Parameter description	**Value (Units)**
Number of cells	72 (−)
Rated power	3 (kW)
Rated voltage	43.2 (V)
Rated hydrogen consumption	39 (Nlpm)
Rated efficiency	40 (%)

For the purposes of this work, instead of working with the polarization curve it is more useful to introduce a black-box regression of fuel consumption in terms of electrical power, since the fuel consumption-electrical power is already available from the manufacturer. This approach is justified by looking at the modelling approach and setup: since all the calculations are based on power flow between powertrain components, it is useful to directly identify the fuel consumption as function of stack power, the main output of the control strategy, instead of identifying the polarisation curve's parameters. Knowing the fuel consumption and the electrical power, it is easy to define the PEMFC stack

voltage and current, needed for the electrical coupling with the powertrain. The fuel cell stack is modelled with a quasi-static approach; hence, no dynamic effects are accounted. This is due to the backward power flow computation required by the model itself, therefore including a dynamic effect on PEMFC delivered power would require modifications on hydrogen consumption including an additional quantity to boost up the delivered power depending on stack transient response time. This modelling approach is reasonable assuming that the medium- and low-level control for PEMFC optimal management is already satisfied in every working condition; hence, the stack is working as declared as the manufacturer. The proposed formulation for fuel consumption as function of electrical power in terms of normal variables is reported below:

$$\upsilon_f = \beta_1 \varphi_{el} + \beta_2 \varphi_{el}^2 + \beta_3 \frac{\varphi_{el}}{\varphi_{el}^{lim} - \varphi_{el}} \tag{IV.30}$$

where υ_f is the normalised fuel consumption, φ_{el} is the normalised electrical power, while β_1, β_2, β_3, and φ_{el}^{lim} are the model parameters. The normalised variables are defined with respect to the rated ones provided by the manufacturer:

$$\upsilon_f = \frac{\dot{m}_{H_2}}{\dot{m}_{H_2}^{rat}} \tag{IV.31}$$

$$\varphi_{el} = \frac{P_{FC}}{P_{FC}^{rat}} \tag{IV.32}$$

To tune model parameters, two nested error minimization algorithms are implemented: the internal cycle minimises the error function varying the three β parameters at a given φ_{el}^{lim} value, while the external iteration adjusts the φ_{el}^{lim} parameter to further reduce the global error. The proposed black-box formulation correctly reproduces the stack performances at any working condition, with a RMSE equal to about 0.0023; the correlation is also high, with R^2 equal to 0.99997. The final hydrogen consumption curve is graphed in Figure IV.17.

From stack power P_{FC} and hydrogen consumption $\dot{m}_{H_2}$, it is possible to characterise stack current and voltage. The stack current is calculated from the hydrogen reaction stoichiometry:

$$I_{FC} = \frac{2F}{M_{H_2} N_c} \dot{m}_{H_2} \tag{IV.33}$$

where N_c is the number of cells inside the stack. Together with current and

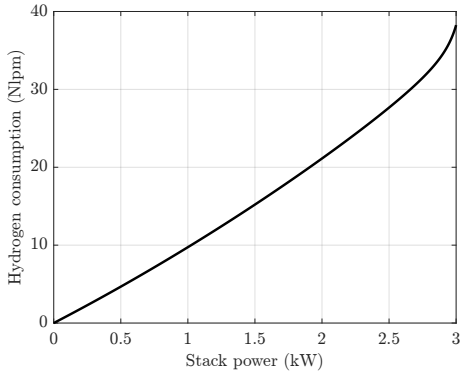


Figure IV.17 *H-3000 modelled fuel consumption with respect to electrical power.*

power, the stack voltage is easily calculable:

$$V_{FC} = \frac{P_{FC}}{I_{FC}} \tag{IV.34}$$

The PEMFC efficiency is defined as the ratio between the output power and the chemical energy consumption:

$$\eta_{FC} = \frac{P_{FC}}{\dot{m}_{H_2} HHV_{H_2}} \tag{IV.35}$$

In this case, the efficiency is referred to the higher heating value HHV_{H_2}, differently from the previous chapter: the higher heating value is chosen as reference in accordance to the manufacturer. The stack efficiency, considering auxiliary power absorption to power the stack fan, is defined as follows:

$$\eta_{stack} = \frac{P_{FC} - P_{aux}}{\dot{m}_{H_2} HHV_{H_2}} \tag{IV.36}$$

The PEMFC efficiency and the stack efficiency, considering 150 W fixed power absorption, are reported in Figure IV.18, with black dashed and solid lines respectively.

The DC/DC converter considered for this application is modelled with the same circuital representation proposed for the battery DC/DC converter, presented with Figure IV.7 and eq. (IV.17). The model parameters are tuned to ensure 90% efficiency at rated power of 3 kW. In Figure IV.19, the efficiency curve as function of stack source power is reported. This DC/DC converter is uni-directional; hence, only source to load energy flow direction is allowed.

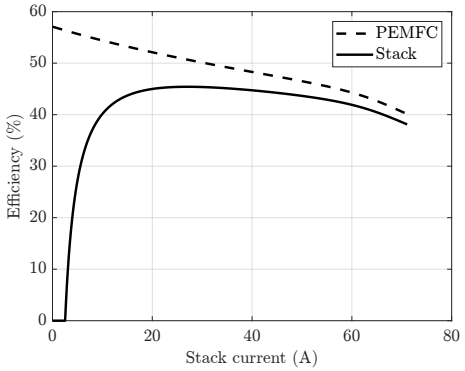


Figure IV.18 *H-3000 modelled efficiency, referred to PEMFC only (dashed line) and at system level (solid line), with respect to stack current.*

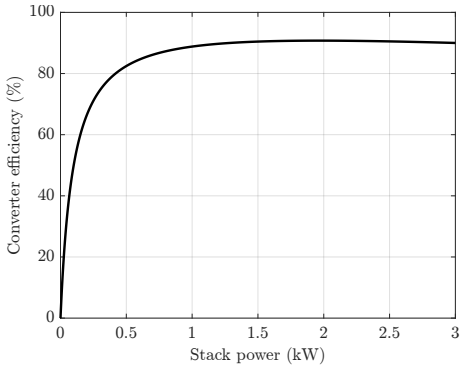


Figure IV.19 *DC/DC converter efficiency as function of transmitted power in discharging mode (solid line) and charging mode (dashed line), at 48 V.*

IV.2.3 Control strategies description

Once the powertrain is properly designed and modelled, a high-level control strategy is needed to manage energy share between the battery and the PEMFC stack. The following high-level control strategies are defined and tested for the proposed configurations, according to Table IV.3.

Table IV.3 *Configuration matrix of the control strategies with respect to powertrain layout.*

	T3	**T3-bis**	**T4**
RB	V	V	V
PI-RB	X	X	V
PMP	X	X	V
A-ECMS	X	X	V

ON-OFF rule-based control strategy (RB)

The ON-OFF Rule Based (RB) control strategy is the simplest charge-sustaining strategy implementable on-board: it is easy to define and suitable for on-board applications and for most powertrains. On the other side, it is a heuristic control strategy, hence there is no optimization of fuel consumption at all. The ON-OFF RB strategy is based on battery SoC and it is implemented acting on the ideal switch, normally open: when the battery SoC is below a certain threshold, the switch is closed letting the PEMFC to deliver electrical power. The switch is kept closed until the battery SoC reaches an upper threshold. For the T3 and T3-bis architectures, there is no control on the electrical power provided by the PEMFC stack, since the stack voltage is passively set by the electric grid; considering the T4 architecture, the PEMFC DC/DC converter sets the PEMFC voltage to obtain 2 kW of electrical power as a trade-off between enough power and acceptable efficiency. An example of ON-OFF RB strategy application is shown in Figure IV.20.

PI-based rule-based control strategy (PI-RB)

The Proportional Integral-Rule Based (PI-RB) control strategy is applicable only for the T4 architecture, in which the PEMFC stack is actively controlled acting on the DC/DC converter. This EMS is similar to the simple ON-OFF RB, but in this case the REx power required is defined to sustain the battery SoC around a certain value. This strategy is SoC-following: a separate Proportional

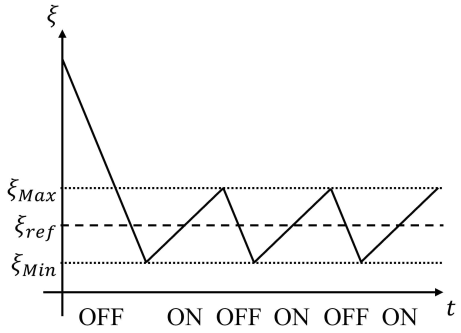


Figure IV.20 *Example of ON-OFF Rule-Based control strategy application on battery SoC.*

Integral (PI) controller sets the requested stack power to be followed based on battery SoC deviation from a reference value. This type of solution is suitable for both full and plug-in HEV, being more versatile than pure ON-OFF switching solution provided by simple RB. The PI controller establish the amount of power required to the REx to follow the SoC reference as follows:

$$P_{FC}^{req}(t) = k_p\left(\xi_{ref} - \xi(t)\right) + k_i \int_0^t \left(\xi_{ref} - \xi(\tau)\right) d\tau \tag{IV.37}$$

where k_p and k_i are the proportional and integral gains, respectively, while ξ_{ref} is the battery SoC target. Similar to the simpler ON-OFF RB, the control strategy closes the ideal switch when the battery SoC reaches a lower threshold value.

Pontryagin's Minimum Principle (PMP)

The PMP is based on the minimisation of an instantaneous cost function, i.e., Hamiltonian, directly derived from the cost function of the optimal problem statement with the introduction of a co-state variable to keep the ending SoC constraint for every time step (Donatantonio et al. 2022). The main disadvantage of PMP is the global non-optimality of the solution, even if it is typically relatively close to the global optimum; instead, differently from other optimal algorithms the computational burden is drastically lower. The Hamiltonian cost function is shown in the following:

$$H\left(\xi(t), \lambda_{co}(t), P_b(t)\right) = \dot{m}_f\left(t, P_b(t)\right) + \lambda_{co}(t)\,\dot{\xi}\left(\xi(t), P_b(t)\right) \tag{IV.38}$$

where H is the Hamiltonian function to be minimised, ξ is the battery SoC as state variable, λ is the co-state variable, while P_b is the battery power

chosen as control variable. The co-state can be determined integrating the Euler-Lagrange equation:

$$\dot{\lambda}_{co} = -\lambda_{co} \frac{\partial \dot{\xi}}{\partial \xi} \tag{IV.39}$$

The partial derivative term $\frac{\partial \dot{\xi}}{\partial \xi}$ can be computed either numerically or analytically; for this application, since the analytical expression of $\dot{\xi}$ with respect to ξ is available, the analytical derivative is implemented for better accuracy and performances (Cervone, Sicilia, Pandolfi, et al. 2024). The initial condition for the co-state variable must be identified ensuring the respect of the final constraint of the battery SoC: this can be performed with iterative algorithms, such as shooting method or bi-section method. The Hamiltonian minimisation is pursued parametrising the control variable P_b on a moving grid, based on battery and PEMFC constraints, in order to achieve faster convergence and solution feasibility.

Adaptive Equivalent Consumption Minimisation Strategy (A-ECMS)

The A-ECMS can be seen as a direct derivation of the PMP algorithm, in which the co-state variable is defined with an arbitrary rule, convenient for the application of interest (Serrao, Onori, and Rizzoni 2009). In this context, a SoC-following co-state rule is applied with a PI-based closed loop algorithm:

$$\lambda_{co}(t) = \lambda_{co,0} + K_p \left(\xi(t) - \xi_{ref}(t)\right) + K_i \int_0^t \left(\xi(\tau) - \xi_{ref}(\tau)\right) d\tau \tag{IV.40}$$

where λ_0 is the initial co-state value, equal to the one obtained from the PMP algorithm, while K_p and K_i are the proportional and integral gains, respectively. The reference battery SoC $\xi_{ref}(t)$ is assumed equal to a linear discharging profile from initial value ξ_0 and ending value ξ_{end} over L distance as follows:

$$\xi_{ref}(t) = \xi_0 + \frac{\xi_{end} - \xi_0}{L} \int_0^t v(\tau)\, d\tau \tag{IV.41}$$

The Hamiltonian minimisation is still accomplished every time instant, with the main difference of on-board implementation capability of this class of control strategies.

IV.3 Simulation results and discussion

The proposed hybrid configurations are tested on the WMTC-L6e standard drive cycle, shown before in Figure IV.12: for every simulation, a total range of 140 km is achieved on 90-20% battery discharge, doubling the original pure EV mileage of 70 km on the same discharge amount.

IV.3.1 T3 architecture

Within the T3 architecture, only the RB control strategy can be applied, as stated in the previous paragraphs. The results in terms of battery SoC with respect to travelled distance is reported in Figure IV.21.

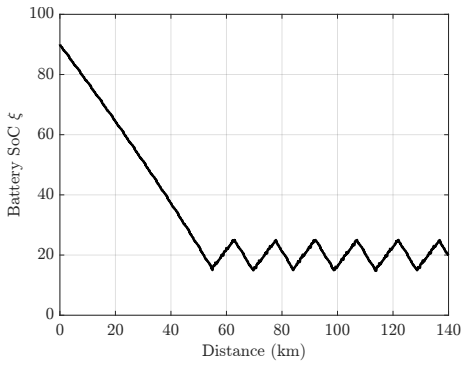
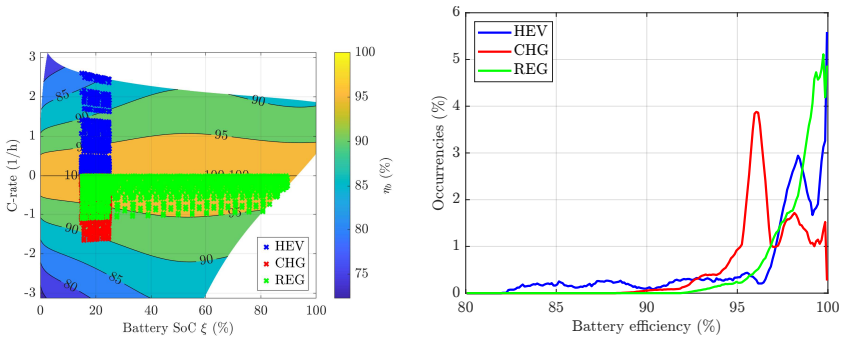


Figure IV.21 *Simulation results for battery State-of-Charge over mileage, T3 architecture.*

The first EV phase lasts around 55 km: this is due to both the reduction of battery capacity and the increase in vehicle weight due to the PEMFC stack system and the hydrogen tank. The stack is turned on six times, with a duty cycle roughly equal to eight km ON over 10 km OFF. The 140 km mileage target is successfully achieved. In Figure IV.22, a deepen analysis on battery performance is reported: on the left, the battery efficiency contour map is reported, with different working modes reported with coloured stars according to the legend; on the right, the efficiency values distributions with respect to working modes are shown.

Analysing the results, it can be seen that the HEV working points are distributed along a wide range of efficiency values down to 80%; the charging efficiency points are concentrated around 95% of battery efficiency. Both HEV and CHG phases do not take advantage of higher efficiency points.

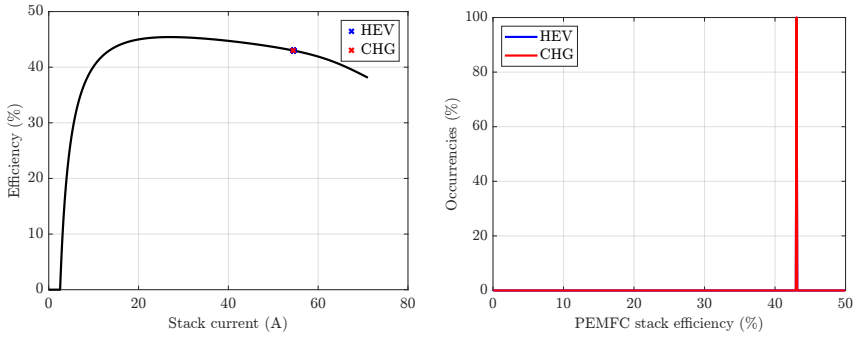
About the PEMFC stack, in Figure IV.23 the efficiency values are reported:



(a) *Efficiency map* **(b)** *Occurrences distribution*

Figure IV.22 *Battery efficiency contour map (left) and efficiency distributions (right), with working points highlighted with respect to operating mode: hybrid (blue); charging (red); regenerative braking (green). T3 architecture.*

on the left side, the efficiency curve with respect to stack current is shown with the working points highlighted; within the right graph, the efficiency values distributions for HEV and CHG working modes are reported.



(a) *Efficiency map* **(b)** *Occurrences distribution*

Figure IV.23 *PEMFC stack efficiency profile (left) and efficiency distributions (right), with working points highlighted with respect to operating mode: hybrid (blue); charging (red). T3 architecture.*

As it can be seen, the PEMFC stack works in fixed-point conditions, as expected, due to the fixed 48 V set by the battery DC/DC converter. In this configuration, the stack is able to provide around 2.5 kW of electrical power, with a steady-state efficiency around 43%. As already explained before, choosing the T3 architecture requires a good compatibility between the PEMFC stack and the voltage requirements by the electric motors: for this application, the stack operates at high power, roughly 80% of the maximum value, still preserving a good efficiency.

To better understand the energy performance of the proposed powertrain, the energetic analysis is shown in Figure IV.24: every energy form is reported from available to dissipations to usage, with colours based on the legend reported on the figure. The energy share is relative to the initial total amount of energy available on board: considering 0.6 kg of hydrogen with 120 MJ/kg as lower heating value together with roughly 3.44 kWh of battery initial energy (equal to 90% of three quarters of 5), a value of 23.44 kWh is obtained.

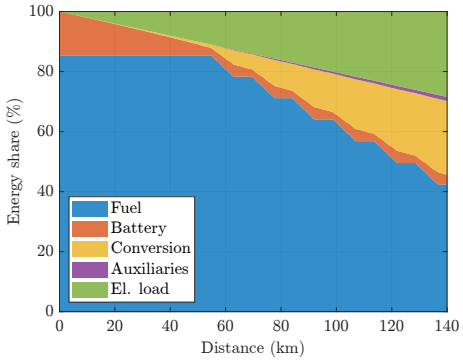


Figure IV.24 *Energy share results during simulation, T3 architecture: hydrogen chemical energy (blue); battery residual energy (red); conversion losses (yellow); auxiliary absorption (purple); load (green).*

Thanks to the energy conservation law, the initial amount of energy is always conserved:

$$E_{fuel}(0) + E_{batt}(0) = E_{fuel}(t) + E_{batt}(t) + E_{conv}(t) + E_{aux}(t) + E_{load}(t) \tag{IV.42}$$

It can be noted how more than 40% of fuel energy is depleted during the simulation. At the end of 140 km, 30% of the initial energy amount is used to fulfil the electrical load request, while auxiliaries and conversion losses sum up to 20%.

IV.3.2 T3-bis architecture

Also for this hybrid layout, the RB control strategy is the only suitable control strategy, acting on the ideal switch. The results in terms of battery SoC with respect to travelled distance is reported in Figure IV.25.

The stack is turned on five times: differently from the T3 architecture, the stack is turned on one time less to still cover the final mileage of 140 km. In Figure IV.26, a deepen analysis on battery performance is reported: on the left,

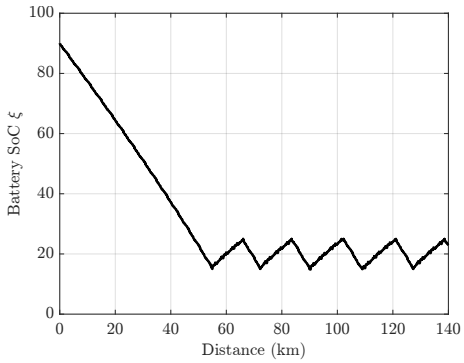
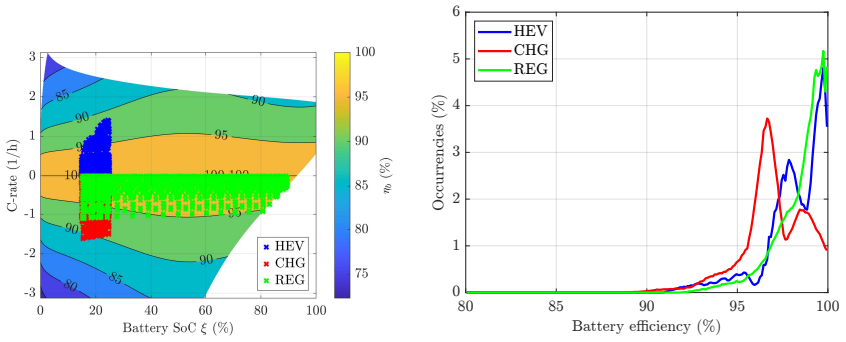


Figure IV.25 *Simulation results for battery State-of-Charge over mileage, T3-bis architecture.*

the battery efficiency contour map is reported, with different working modes reported with coloured stars according to the legend; on the right, the efficiency values distributions with respect to working modes are shown.

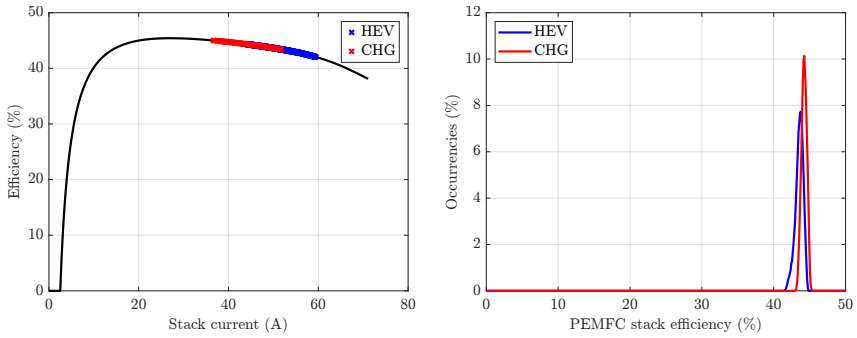


(a) *Efficiency map* **(b)** *Occurrences distribution*

Figure IV.26 *Battery efficiency contour map (left) and efficiency distributions (right), with working points highlighted with respect to operating mode: hybrid (blue); charging (red); regenerative braking (green). T3-bis architecture.*

It can be noted that the HEV working points are better focused at lower currents differently from the T3 architecture results, taking advantage of higher efficiency values. The charging efficiency points are still concentrated around 95% of battery efficiency.

About the PEMFC stack, in Figure IV.27 the efficiency values are reported: on the left side, the efficiency curve with respect to stack current is shown with the working points highlighted; within the right graph, the efficiency values distributions for HEV and CHG working modes are reported.



(a) *Efficiency map* **(b)** *Occurrences distribution*

Figure IV.27 *PEMFC stack efficiency profile (left) and efficiency distributions (right), with working points highlighted with respect to operating mode: hybrid (blue); charging (red). T3-bis architecture.*

In this configuration, the stack operates in a current range from 37 to 60 A, with an efficiency span from 45% down to 42%. There is no control on efficiency, even if the charging points have an average efficiency higher than the HEV ones. This PEMFC stack has a compatible polarisation curve with the battery: this compatibility enhances the electrical coupling between the two components, ensuring good performances of the stack in a narrow band.

The energetic analysis for this powertrain is shown in Figure IV.28: every energy form is reported from available to dissipations to usage, with colours based on the legend reported on the figure.

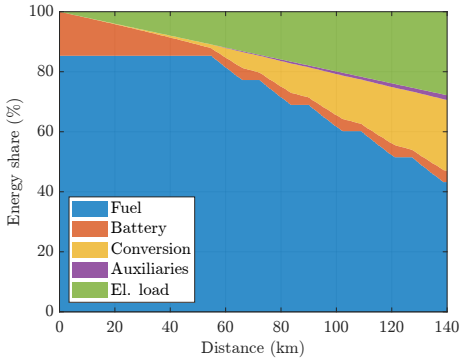


Figure IV.28 *Energy share results during simulation, T3-bis architecture: hydrogen chemical energy (blue); battery residual energy (red); conversion losses (yellow); auxiliary absorption (purple); load (green).*

There is a slight improvement in energy usage with respect to the T3 architecture, with a higher energy residual amount at the end of the simulation.

This can be explained looking at the T3-bis architecture, focusing on elements disposition: the PEMFC stack is directly linked to the battery with no dissipation along the energetical path, meaning that the charging phases in which the energy flows from the PEMFC stack to the battery is energetically advantageous. However, it has to be kept in mind that no dynamic effects are modelled within this application: the PEMFC stack, even if is electrically compatible with the battery, could not be able to follow the battery faster dynamics, leading to power mismatch and higher degradation rates.

IV.3.3 T4 architecture

Within this layout, each control strategy from heuristic to optimal is applicable. The main target is still the final mileage of 140 km. The results in terms of battery SoC with respect to travelled distance is reported in Figure IV.29, with every colour corresponding to a different control strategy based on the legend.

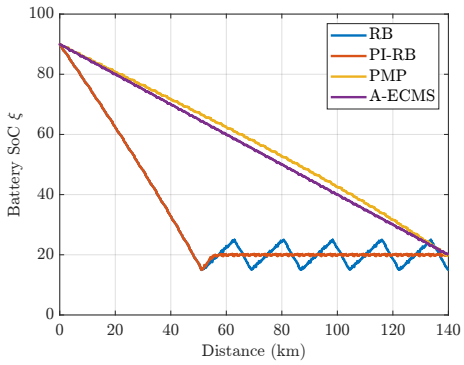
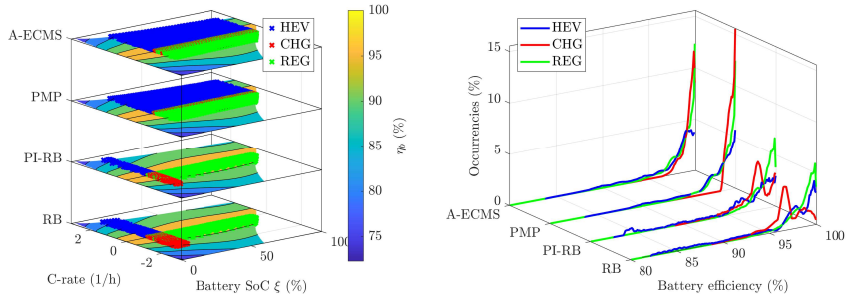


Figure IV.29 *Simulation results for battery State-of-Charge over mileage, T4 architecture: RB (blue); PI-RB (red); PMP (yellow); A-ECMS (purple).*

Looking at the heuristic control strategies, it can be noted that the stack is turned on five times, similarly to the T3-bis architecture; however, the battery charging is faster on average. The PI-RB strategy is able to preserve the average battery SoC around 20% when the switch is closed, as expected. About the optimal control strategies, it can be observed that the PMP control strategy application results in a quite linear battery SoC profile over distance, with the highest deviation at around half target mileage: this shows how the optimal solution found with the PMP, differently from the A-ECMS strategy, is not necessarily linear, taking advantage of battery and stack best efficiencies. In Figure IV.30, a deepen analysis on battery performance is reported: on the left, the battery efficiency contour map is reported, with different working modes

reported with coloured stars according to the legend and different control strategies along the z-axis; on the right, the efficiency values distributions with respect to working modes are shown, with different control strategies along the y-axis.



(a) *Efficiency map* **(b)** *Occurrences distribution*

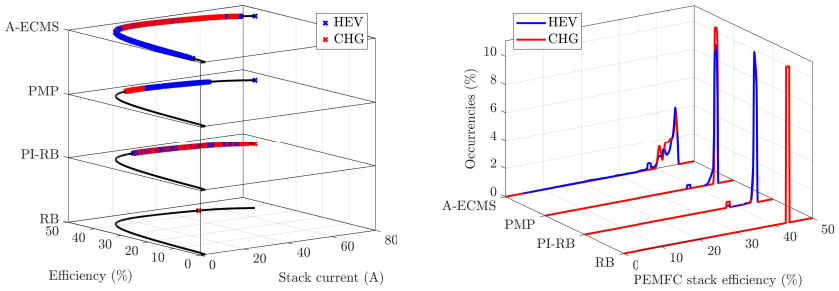
Figure IV.30 *Battery efficiency contour map (left) and efficiency distributions (right), with working points highlighted with respect to control strategies and operating mode: hybrid (blue); charging (red); regenerative braking (green). T4 architecture.*

In this configuration, the RB and the PI-RB control strategies exhibits a similar behaviour as T3 and T3-bis architectures; however, the RB control strategy is critical, since the efficiency distribution in all phases is the worst. The PMP control strategy is able to exploit the best charging efficiency points among all the strategies and the architectures; the A-ECMS performs similarly.

About the PEMFC stack, in Figure IV.31 the efficiency values are reported: on the left side, the efficiency curve with respect to stack current is shown with the working points highlighted, with different control strategies along the z-axis; within the right graph, the efficiency values distributions for HEV and CHG working modes are reported, with different control strategies along the y-axis.

The PEMFC stack works in a fixed operating point as expected within the RB control strategy, while looking at PI-RB results both HEV and CHG efficiency distributions are centred along 45%. The best results are obtained with the PMP control strategy as expected: the CHG points are focused around the efficiency curve peak, maximising the battery charging. The A-ECMS shows several working points, particularly in HEV mode, at low currents: this condition can be critical in terms of auxiliaries absorption.

The energetic analysis for this powertrain is shown in Figure IV.32: every energy form is reported from available to dissipations to usage, with colours based on the legend reported on the figure, with a different control strategy along the z-axis.



(a) *Efficiency map* **(b)** *Occurrences distribution*

Figure IV.31 *PEMFC stack efficiency profile (left) and efficiency distributions (right), with working points highlighted with respect to control strategies operating mode: hybrid (blue); charging (red). T4 architecture.*

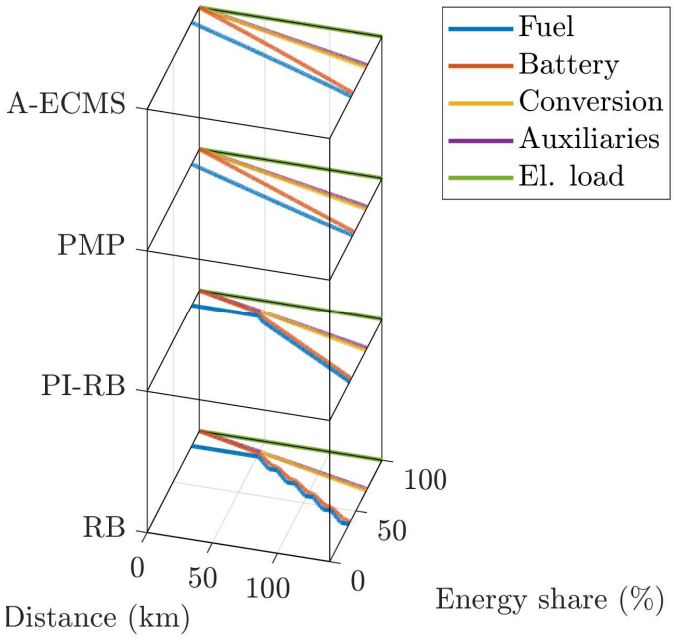


Figure IV.32 *Energy share results during simulation for every control strategy, T4 architecture: hydrogen chemical energy (blue); battery residual energy (red); conversion losses (yellow); auxiliary absorption (purple); load (green).*

Thanks to the energy shares, it is easy to observe that the RB control strategy for this architecture is the worst solution in terms of energetical efficiency: less than 50% of initial energy is preserved at the end of the simulation considering both battery and residual hydrogen; the PI-RB is able to obtain better results. The PMP strategy results confirm the optimality of the solution, since the equivalent fuel consumption is optimised at each time step; the A-ECMS control strategy is able to replicate similar results.

IV.3.4 Macro parameters comparison

To compare all the proposed architectures and relative control strategies performance, three synthetical parameters are calculated for each simulation. The first parameter is the average fuel consumption, defined as the total hydrogen consumed for 100 km on average:

$$FC = \frac{\int_0^T \dot{m}_{H_2}(t)\,dt}{\int_0^T v(t)\,dt} \cdot 100 \text{ km} \tag{IV.43}$$

The average fuel consumption for every simulation is then reported in Figure IV.33, with every colour corresponding to a different control strategy according to the legend.

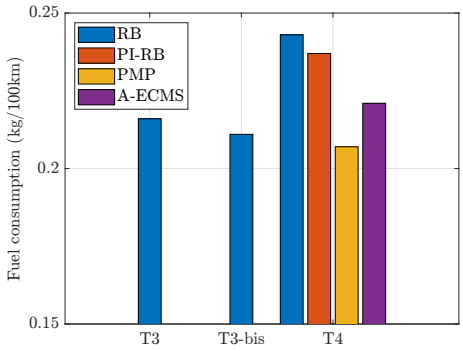


Figure IV.33 *Average fuel consumption results for every simulation.*

Regarding the RB control strategy, it is interesting to note that the T3-bis architecture is the least fuel demanding configuration on average: this further confirms the energetically advantageous nature of this layout, in which the PEMFC stack can charge the battery directly with no dissipation. The T3 architecture is able to obtain a similar average fuel consumption; in addition, this architecture is the most suitable for fixed point operations, in which the PEMFC stack is able to perform better with no dynamics involved. The T4 architecture

is the worst solution with heuristic control strategies: this powertrain layout accounts for the highest number of energy transformations, worsening the fuel consumption up to 15%. Similar considerations can be made for the PI-RB control strategy, with a little benefit due to the narrow battery SoC range when the stack is activated. As expected, the PMP control strategy is able to optimise the final fuel consumption, making it the best choice for this architecture. Even though the results are worse than those of simpler architectures, the A-ECMS control strategy is still able to optimise fuel consumption with respect to heuristic strategies.

The second parameter is the average equivalent fuel consumption, accounting also for battery usage:

$$EFC = \left(\int_0^T \dot{m}_{H_2}(t)\, dt + \frac{1}{LHV_{H_2} \eta_{REx}^{avg}} \int_0^T E_{nom} \dot{\xi}(t)\, dt \right) \cdot \frac{100 \text{ km}}{\int_0^T v(t)\, dt} \tag{IV.44}$$

It is noteworthy to remark that the average REx efficiency η_{REx}^{avg} is scaled to the lower heating value, since the manufacturer considers the efficiency with respect to the higher heating value. The average equivalent fuel consumption for every simulation is then reported in Figure IV.34, with every colour corresponding to a different control strategy according to the legend.

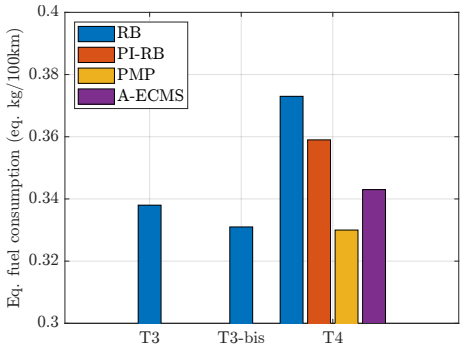


Figure IV.34 *Average equivalent fuel consumption results for every simulation.*

The effects on battery utilisation are further empathised: the T3-bis architecture is the least demanding configuration on average, with T4 architecture obtaining a slightly better result only with the PMP algorithm. The T3 architecture reaffirms to be a feasible solution, with average energetical performance and technical compatibility with PEMFC slow dynamics.

The third and final parameter is the average Powertrain Efficiency Index

(PEI), defined as the ratio between total energy absorption by load and auxiliaries over final energy stored by battery and residual hydrogen

$$PEI = \frac{E_{load}(T) + E_{aux}(T)}{E_{batt}(T) + E_{H_2}(T)} \tag{IV.45}$$

The average PEI for every simulation is then reported in Figure IV.35, with every colour corresponding to a different control strategy according to the legend.

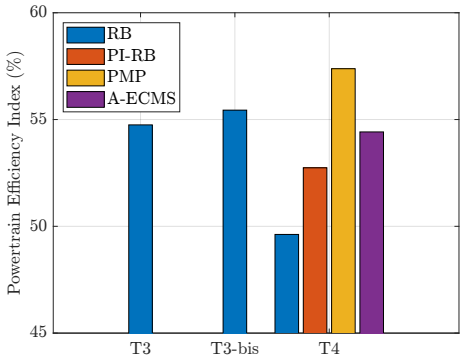


Figure IV.35 *Average Powertrain Efficiency Index results for every simulation.*

It can be noted that with T3 and T3-bis architecture the final powertrain efficiency is around 55%, with the T3-bis one slightly better than the T3: this confirms how the T3 architecture can be the preferred solution with low requirements on control side and slow PEMFC stacks. The T4 architecture performs best with the PMP algorithm, reaching up to 57% efficiency; the RB control strategy is the worst condition, with a PEI lower than 50%.

A final comparison between architectures and control strategies can be performed analysing how the instantaneous PEI changes with power split, defined as the ratio between battery power and stack power. The trends are reported in Figure IV.36: every architecture with RB control strategy is identified with a solid line and a different colour, while the other control strategies for the T4 architecture are also identified with a different marker.

The trends of the instantaneous PEI reaffirms the considerations previously discussed. In the charging region, in which the power split is negative, the T3 and T3-bis architectures show the best instantaneous PEI since the electrical power delivered by the stack is provided to the battery with one electrical conversion or none at all. The T4 architecture performs worst in charging, since two different DC/DC converters are present along the energy path. However, in HEV conditions when the power split is higher than zero, the main advantages

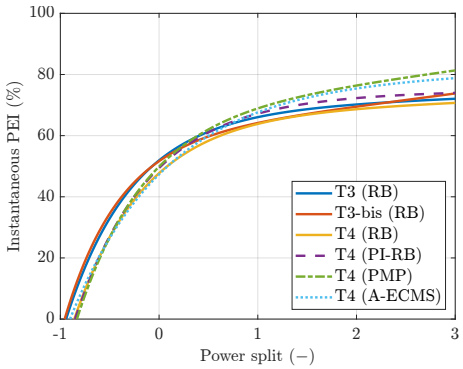


Figure IV.36 *Instantaneous PEI for every architecture (solid lines) and every control strategies (different markers) as function of power split.*

of the PMP and A-ECMS control strategies are more evident as the power split increases. The T4 architecture can be the worst in any conditions if not optimised; hence, it can be considered only with optimal control strategies to benefit from powertrain flexibility.

IV.4 Conclusions

In this chapter, an energetic simulation model for a electric hybrid lightweight vehicle design is presented. The original vehicle is a pure electric vehicle, with 100 km as declared mileage on a 100% battery discharge rate: the model is firstly validated on this target, reaching 70 km on 90-20% battery discharge. The vehicle is then hybridised adding a PEMFC stack with 3 kW of maximum power and a properly designed hydrogen tank, able to double the vehicle original distance. Three different electrical architectures are proposed, ranging in complexity and number of additional components: T3, T3-bis, and T4. Every architecture is characterised by the disposal order of components, with differences along the energy paths. Finally, two heuristic control strategies and two optimal algorithms are considered and implemented: T3 and T3-bis architectures can be controlled only with a simple RB control strategy, while the T4 architecture is suitable for optimal control strategies being the most flexible powertrain layout. Every configuration is tested for 140 km on 90-20% battery discharge. The results show that the T3 architecture can be a desired solution that couples good efficiency around 55% and technical feasibility, with the stack working in a fixed condition with no dynamics at all. The T3-bis architecture is the solution with less energetic dissipations; however, the stack must be electrically compatible with the battery and it must accomplish fast dynamics, following load request. The T4 architecture is the worst solution from a pure

energetic point of view, with a final efficiency lower than 50% if not optimised; however, when optimal control strategies like PMP and A-ECMS are considered, this powertrain layout can be the best solution with a final efficiency up to 57%. The high complexity of this powertrain layout is balanced with the high flexibility.

Future developments of this work include a different modelling approach. As stated before, in order to introduce the optimal algorithms, the model is developed with a backward, computing the requested power from vehicle desired speed; however, this modelling description is not able to account any dynamic effect. This can be particularly critical for PEMFC stack, in which the dynamics can be significantly slower than both battery and load variations: if the stack is not able to follow the requested power profile in time, corrective actions have to be included to cover the power gap potentially left by the stack.

Conclusions

The research work presented in this thesis addressed the critical challenge of enhancing the efficiency and durability of PEMFC systems for automotive applications through advanced modelling and optimal control. Hydrogen emerges as a versatile energy carrier, capable of being employed in advanced electrochemical devices such as fuel cells, offering superior efficiency and zero emission operation, particularly when integrated into hybrid architectures. Such hybridisation enables optimized powertrain performance, minimising hydrogen consumption while ensuring pollutant-free mobility.

The first contribution of this thesis is the development of a control-oriented lumped model for the stack, with a specific focus on membrane water management. By applying a mathematical linearization of the governing PDEs through the integral method, it is possible to capture the complex internal dynamics while maintaining a low computational burden. This represents a significant step forward compared to traditional black-box models or computationally expensive 3D CFD simulations, making the proposed approach suitable for real-time on-board monitoring and prognostics. The experimental validation, conducted using data from a 100 W open-cathode PEMFC stack, shows the high accuracy and generalisability of the model. In particular, the polarization curve fitting achieved a coefficient of determination R^2 of 0.9996 in steady-state conditions, while the dynamic tests show the model's capability to track voltage and temperature transients with an average absolute error below 5%. These results confirm that the proposed lumped architecture effectively bridges the gap between physical fidelity and execution speed, with a computational time faster more than 50 times real-time.

The second contribution is the model-based design of a hybrid powertrain architecture, specifically for an L6e quadricycle, with a PEMFC-based REx capable of doubling the mileage of the original vehicle. The proposed modelling approach allows for the evaluation of different EMSs, analysing pros and cons of every solution while comparing the final fuel consumptions. The comparative analysis showed that optimal and semi-optimal strategies, such as the PMP and the A-ECMS, can lead to a reduction in hydrogen consumption of approximately 7% compared to standard rule-based approaches, while simultaneously

improving the stack's operating conditions and potentially its lifespan.

This research activity paves the way for a transition toward a unified modelling framework that integrates Model-Based Design and Model-Based Control methodologies. The multi-scale approach adopted in this dissertation balances model fidelity with computational constraints across different system hierarchy levels. At the component level (Chapters II–III), high-fidelity dynamic modeling is required for monitoring, degradation tracking, and micro-second diagnostic tasks. At the vehicle level (Chapter IV), a backward quasi-static framework is selected to benchmark multi-objective EMS over full driving cycles without incurring excessive computational overhead. While the current vehicle-level simulation assumes dynamic stack response to be instantaneous relative to cycle-scale power splits, integrating the full dynamic PEMFC model into a forward vehicle simulator constitutes an immediate future outlook to quantify power-tracking errors during rapid transients. Furthermore, regarding hardware scalability, while the experimental validation was conducted on a 100 W open-cathode stack, the underlying dimensionless formulation of the membrane water transport equations ensures physical scalability to larger, pressurised automotive-grade FC stacks, provided that auxiliary dynamics (e.g., compressor delay, active humidification) are properly described. Future efforts will be directed toward the development of a complete and integrated simulation platform, where the advanced PEMFC models developed here can serve as the core of a digital twin for the entire hybrid powertrain. This modelling approach at different levels allows the simultaneous optimisation of component sizing and energy management strategies. The integrated environment is crucial for accelerating the development cycle of fuel cell vehicles, allowing for extensive virtual testing, and reducing the reliance on costly physical prototypes. Furthermore, the modularity and low computational burden of the proposed models make them suitable for implementation in Software-in-the-Loop (SiL) and Hardware-in-the-Loop (HiL) environments. This will provide a robust tool for the testing and validation of next-generation control units under diverse and realistic operating scenarios, ultimately fostering the large-scale deployment of efficient and sustainable hybrid mobility solutions.

In conclusion, hydrogen technologies, and especially PEMFC-based solutions, represent a promising pathway toward sustainable mobility. The integration of advanced modelling tools, hybrid architectures, and intelligent control strategies will be essential to fully unlock their potential, ensuring both environmental benefits and technological feasibility in real-world transport applications.

References

Aimikhe, Victor Joseph and OE Eyankware (2023). "Recent advances in white hydrogen exploration and production: a mini review". In: *Journal of energy research and reviews* 13.4, pp. 64–79.

Amatruda, Ferdinando (2014). "Sviluppo e validazione di un modello dinamico a parametri concentrati per la simulazione del trasporto bifasico non isotermo all'interno di una cella a combustibile PEM". Master's thesis. University of Salerno.

Amin, Ashraf M, Eric Croiset, and William Epling (2011). "Review of methane catalytic cracking for hydrogen production". In: *International Journal of Hydrogen Energy* 36.4, pp. 2904–2935.

Arshad, Adeel et al. (2019). "Energy and exergy analysis of fuel cells: A review". In: *Thermal Science and Engineering Progress* 9, pp. 308–321.

Axsen, Jonn and Kenneth S Kurani (2013). "Hybrid, plug-in hybrid, or electric—What do car buyers want?" In: *Energy policy* 61, pp. 532–543.

Aziz, Muhammad et al. (2015). "Utilization of electric vehicles and their used batteries for peak-load shifting". In: *Energies* 8.5, pp. 3720–3738.

Banvait, Harpreetsingh, Sohel Anwar, and Yaobin Chen (2009). "A rule-based energy management strategy for plug-in hybrid electric vehicle (PHEV)". In: *2009 American control conference*. IEEE, pp. 3938–3943.

Barbir, Frano (2013). *PEM Fuel Cells: Theory and Practice*. 2nd. Academic Press. ISBN: 978-0-12-387710-9. DOI: 10.1016/C2011-0-06706-6.

Bauer, Christian et al. (2022). "On the climate impacts of blue hydrogen production". In: *Sustainable Energy & Fuels* 6.1, pp. 66–75.

Benchouia, Nedjmeddine et al. (2013). "Modeling and validation of fuel cell PEMFC". In: *Revue des Energies Renouvelables* 16.2, pp. 365–377.

Benzing, Enrico (2004). *Dall'aerodinamica alla potenza in Formula 1: mezzo secolo di motori in analisi*. Nada Editore.

Bhandari, Ramchandra, Clemens A Trudewind, and Petra Zapp (2014). "Life cycle assessment of hydrogen production via electrolysis–a review". In: *Journal of cleaner production* 85, pp. 151–163.

Böhme, Thomas J and Benjamin Frank (2017). "Hybrid systems, optimal control and hybrid vehicles". In: *Cham, CH: Springer International*, pp. 401–428.

Buck Research Instruments L.L.C (1996). *Buck Research CR-1A User's Manual, Appendix 1*.

Caponi, Roberta et al. (2021). "Thermodynamic modeling of hydrogen refueling for heavy-duty fuel cell buses and comparison with aggregated real data". In: *International Journal of Hydrogen Energy* 46.35, pp. 18630–18643. DOI: 10.1016/j.ijhydene.2021.02.224.

Cervone, Davide, Massimo Sicilia, Alfonso Pandolfi, et al. (2024). "Machine Learning Based Design of Optimal Energy Management Strategy for Hydrogen-Fueled Hybrid Vehicle Powertrain". In: *Conference on Sustainable Mobility*. SAE International. DOI: 10.4271/2024-24-0001.

Cervone, Davide, Massimo Sicilia, Marco Romano, et al. (2023). "Modelling of a Hybrid Quadricycle (L6e vehicle) Equipped with Hydrogen Fueled ICE Range Extender and Performance Analysis on Stochastic Drive Cycles Generated from RDE Profile". In: *SAE International Journal of Advances and Current Practices in Mobility* 6.2023-24-0149, pp. 2087–2101.

Chen, Fengxiang, Liming Zhang, and Jieran Jiao (2021). "Modelling of humidity dynamics for open-cathode proton exchange membrane fuel cell". In: *World Electric Vehicle Journal* 12.3, p. 106.

Dash, Santanu Kumar, Suprava Chakraborty, and Devaraj Elangovan (2023). "A brief review of hydrogen production methods and their challenges". In: *Energies* 16.3, p. 1141.

Domenico, Alfonso Di (2007). "A Dynamic model of automotive PEM Fuel Cell System for powertrain Design, Control and hierarchical model identification within Hardware in the Loop Fuel Cell Hybrid Testing". Ph.D. thesis. University of Salerno.

Donatantonio, Fabrizio et al. (2022). "Novel Approaches for Energy Management Strategies of Hybrid Electric Vehicles and Comparison with Conventional Solutions". In: *Energies* 15.6, p. 1972. DOI: 10.3390/en15061972.

Dulian, Monika and Gregor Erbach (2025). *Renewable and low-carbon hydrogen: State of play and outlook*. Briefing PE 767.227. Accessed: 2025-05-22. European Parliamentary Research Service (EPRS). URL: https://www.europarl.europa.eu/RegData/etudes/BRIE/2025/767227/EPRS_BRI(2025)767227_EN.pdf.

Esposito, Angelo, Cesare Pianese, and Yann G. Guezennec (2010). "Coupled modeling of water transport and air-droplet interaction in the electrode of a proton exchange membrane fuel cell". In: *Journal of Power Sources* 195.13, pp. 4149–4159. DOI: 10.1016/j.jpowsour.2010.01.020.

Ferrara, Alessandro, Pierpaolo Polverino, and Cesare Pianese (2018). "Analytical calculation of electrolyte water content of a Proton Exchange Mem-

brane Fuel Cell for on-board modelling applications". In: *Journal of Power Sources* 390, pp. 197–207. DOI: 10.1016/j.jpowsour.2018.04.005.

Gao, Yimin, Mehrdad Ehsani, and John M Miller (2005). "Hybrid electric vehicle: Overview and state of the art". In: *Proceedings of the IEEE International Symposium on Industrial Electronics, 2005. ISIE 2005.* Vol. 1. IEEE, pp. 307–316.

Giorgi, Leonardo and Fabio Leccese (2013). "Fuel cells: Technologies and applications". In: *The Open Fuel Cells Journal* 6.1, pp. 1–20.

Govardhan, Ojas M (2017). "Fundamentals and classification of hybrid electric vehicles". In: *International Journal of Engineering and Techniques* 3.5, pp. 194–198.

Guo, Xiaokai and Gaocheng An (2025). "A hierarchical optimization energy management strategy based on AECMS-MPC for heavy-duty fuel cell hybrid vehicles". In: *Energy*, p. 137591.

Guzzella, Lino and Antonio Sciarretta (2013). *Vehicle Propulsion Systems: Introduction to Modeling and Optimization*. 3rd. Springer Berlin, Heidelberg. ISBN: 978-3-642-35913-2. DOI: 10.1007/978-3-642-35913-2.

GWL Group (2023). *LGMH1 18650 Battery Cell Data*.

Haji, Shaker (2011). "Analytical modeling of PEM fuel cell i–V curve". In: *Renewable Energy* 36.2, pp. 451–458.

Hermann, Allen, Tapas Chaudhuri, and Priscila Spagnol (2005). "Bipolar plates for PEM fuel cells: A review". In: *International journal of hydrogen Energy* 30.12, pp. 1297–1302.

Horizon Technologies (2023a). *H-100 Fuel Cell Stack - User Manual*.

— (2023b). *H-3000 Fuel Cell Stack - User Manual*.

Hu, Donghai et al. (2024). "Comprehensive review of hydrogen leakage in relation to fuel cell vehicles and hydrogen refueling stations: status, challenges, and future prospects". In: *Energy & Fuels* 38.6, pp. 4803–4835.

Husar, Attila, Stephan Strahl, and Jordi Riera (2012). "Experimental characterization methodology for the identification of voltage losses of PEMFC: Applied to an open cathode stack". In: *International journal of hydrogen energy* 37.8, pp. 7309–7315.

Ijaodola, OS et al. (2019). "Energy efficiency improvements by investigating the water flooding management on proton exchange membrane fuel cell (PEMFC)". In: *Energy* 179, pp. 246–267.

Incer-Valverde, Jimena et al. (2023). ""Colors" of hydrogen: Definitions and carbon intensity". In: *Energy conversion and management* 291, p. 117294.

Ji, Mengbo and Zidong Wei (2009). "A review of water management in polymer electrolyte membrane fuel cells". In: *Energies* 2.4, pp. 1057–1106.

Jiao, Kui and Xianguo Li (2011). "Water transport in polymer electrolyte membrane fuel cells". In: *Progress in energy and combustion Science* 37.3, pp. 221–291.

Kannah, R Yukesh et al. (2021). "Techno-economic assessment of various hydrogen production methods–A review". In: *Bioresource technology* 319, p. 124175.

Keçebaş, Ali and Muhammet Kayfeci (2019). "Hydrogen properties". In: *Solar hydrogen production*. Elsevier, pp. 3–29.

Kestin, Joseph, Mordechai Sokolov, and William A. Wakeham (1978). "Viscosity of liquid water in the range -8 °C to 150 °C". In: *Journal of Physical and Chemical Reference Data* 7.3, p. 941. DOI: 10.1063/1.555581.

Kim, Mansu et al. (2014). "Effects of anode flooding on the performance degradation of polymer electrolyte membrane fuel cells". In: *Journal of Power Sources* 266, pp. 332–340.

Krithika, V and C Subramani (2018). "A comprehensive review on choice of hybrid vehicles and power converters, control strategies for hybrid electric vehicles". In: *International journal of energy research* 42.5, pp. 1789–1812.

Kumbur, E.C., K.V. Sharp, and M.M. Mench (2007). "On the effectiveness of Leverett approach for describing the water transport in fuel cell diffusion media". In: *Journal of Power Sources* 168.2, pp. 356–368. DOI: https://doi.org/10.1016/j.jpowsour.2007.02.054.

Kweku, Darkwah Williams et al. (2018). "Greenhouse effect: greenhouse gases and their impact on global warming". In: *Journal of Scientific research and reports* 17.6, pp. 1–9.

Larminie, James and Andrew Dicks (2003). *Fuel Cell Systems Explained*. 2nd. John Wiley & Sons Ltd. ISBN: 0-470-84857-X.

Le Canut, Jean-Marc, Rami M Abouatallah, and David A Harrington (2006). "Detection of membrane drying, fuel cell flooding, and anode catalyst poisoning on PEMFC stacks by electrochemical impedance spectroscopy". In: *Journal of The Electrochemical Society* 153.5, A857.

Lipartiti, Andrea (2022). "Experimental investigation of operating conditions effect on PEMFC performance". Master's thesis. University of Salerno.

Liu, Wei (2013). *Introduction to hybrid vehicle system modeling and control*. John Wiley & Sons.

Lü, Xueqin et al. (2018). "A comprehensive review on hybrid power system for PEMFC-HEV: Issues and strategies". In: *Energy conversion and Management* 171, pp. 1273–1291.

Maggio, G, V Recupero, and L Pino (2001). "Modeling polymer electrolyte fuel cells: an innovative approach". In: *Journal of Power Sources* 101.2, pp. 275–286. DOI: 10.1016/S0378-7753(01)00758-3.

Maghfiroh, Hari, Oyas Wahyunggoro, and Adha Imam Cahyadi (2024). "Energy management in hybrid electric and hybrid energy storage system vehicles: A fuzzy logic controller review". In: *IEEE access* 12, pp. 56097–56109.

Mahapatra, Prateek et al. (May 2021). “Design, Analysis, and Fabrication of an Electric Dune Buggy”. In: *International Journal of Engineering and Technical Research* 10, p. 567.

Mazumder, Sandip (July 2005). “A Generalized Phenomenological Model and Database for the Transport of Water and Current in Polymer Electrolyte Membranes”. In: *Journal of The Electrochemical Society* 152, A1633. DOI: 10.1149/1.1940747.

Mulholland, Eamonn et al. (2022). “The role of NOx emission reductions in Euro 7/VII vehicle emission standards to reduce adverse health impacts in the EU27 through 2050”. In: *Transportation Engineering* 9, p. 100133.

Munsi, Md Shahin and Hicham Chaoui (2024). “Energy management systems for electric vehicles: A comprehensive review of technologies and trends”. In: *IEEE access* 12, pp. 60385–60403.

Murugan, Arul and Andrew S Brown (2015). “Review of purity analysis methods for performing quality assurance of fuel cell hydrogen”. In: *International Journal of Hydrogen Energy* 40.11, pp. 4219–4233.

Nandjou, Fredy et al. (2016). “Impact of heat and water management on proton exchange membrane fuel cells degradation in automotive application”. In: *Journal of Power Sources* 326, pp. 182–192.

Okonkwo, Paul C and Clement Otor (2021). “A review of gas diffusion layer properties and water management in proton exchange membrane fuel cell system”. In: *International Journal of Energy Research* 45.3, pp. 3780–3800.

Oliveira, Alexandra M, Rebecca R Beswick, and Yushan Yan (2021). “A green hydrogen economy for a renewable energy society”. In: *Current Opinion in Chemical Engineering* 33, p. 100701.

OPV Smart Urban Mobility (2023). *Booklet Tritone*.

Osman, Ahmed I et al. (2022). “Hydrogen production, storage, utilisation and environmental impacts: a review”. In: *Environmental Chemistry Letters* 20.1, pp. 153–188.

Overington, Shane and Sumedha Rajakaruna (2012). “Review of PHEV and HEV operation and control research for future direction”. In: *2012 3rd IEEE International symposium on power electronics for distributed generation systems (PEDG)*. IEEE, pp. 385–392.

Pan, Mingzhang et al. (2021). “A review of membranes in proton exchange membrane fuel cells: Transport phenomena, performance and durability”. In: *Renewable and Sustainable Energy Reviews* 141, p. 110771.

Pant, Lalit M., Sushanta K. Mitra, and Marc Secanell (2012). “Absolute permeability and Knudsen diffusivity measurements in PEMFC gas diffusion layers and micro porous layers”. In: *Journal of Power Sources* 206, pp. 153–160. DOI: 10.1016/j.jpowsour.2012.01.099.

Peighambardoust, S Jamai, Soosan Rowshanzamir, and Mehdi Amjadi (2010). "Review of the proton exchange membranes for fuel cell applications". In: *International journal of hydrogen energy* 35.17, pp. 9349–9384.

Peng, Ruoqing et al. (2024). "Investigating the factors influencing the electric vehicle market share: A comparative study of the European Union and United States". In: *Applied Energy* 355, p. 122327.

Pinsky, Roxanne et al. (2020). "Comparative review of hydrogen production technologies for nuclear hybrid energy systems". In: *Progress in Nuclear Energy* 123, p. 103317.

Polverino, Pierpaolo, Ivan Arsie, and Cesare Pianese (2021). "Optimal energy management for hybrid electric vehicles based on dynamic programming and receding horizon". In: *Energies* 14.12, p. 3502.

Polverino, Pierpaolo, Angelo Esposito, and Cesare Pianese (2013). "Experimental validation of a lumped model of single droplet deformation, oscillation and detachment on the GDL surface of a PEM fuel cell". In: *International journal of hydrogen energy* 38.21, pp. 8934–8953.

Pourrahmani, Hossein, Mahdi Moghimi, and Majid Siavashi (2019). "Thermal management in PEMFCs: the respective effects of porous media in the gas flow channel". In: *International Journal of Hydrogen Energy* 44.5, pp. 3121–3137.

Pramuanjaroenkij, Anchasa and Sadık Kakaç (2023). "The fuel cell electric vehicles: The highlight review". In: *International Journal of Hydrogen Energy* 48.25, pp. 9401–9425.

Pukrushpan, Jay T, Huei Peng, and Anna G Stefanopoulou (2004). "Control-oriented modeling and analysis for automotive fuel cell systems". In: *J. Dyn. Sys., Meas., Control* 126.1, pp. 14–25.

Rezaei, Amir and Jeffrey B Burl (2015). "Effects of time horizon on model predictive control for hybrid electric vehicles". In: *IFAC-PapersOnLine* 48.15, pp. 252–256.

Riley, Jarrett et al. (2021). "Technoeconomic analysis for hydrogen and carbon Co-Production via catalytic pyrolysis of methane". In: *International Journal of Hydrogen Energy* 46.39, pp. 20338–20358.

Ritchie, Hannah (2020). "Cars, planes, trains: where do CO_2 emissions from transport come from?" In: *Our World in Data*. URL: https://archive.ourworldindata.org/20251125-173858/co2-emissions-from-transport.html.

Ritchie, Hannah, Pablo Rosado, and Max Roser (2020). "Breakdown of carbon dioxide, methane, and nitrous oxide emissions by sector". In: *Our World in Data*. URL: https://archive.ourworldindata.org/20251204-144539/emissions-by-sector.html.

— (2023). "CO_2 and Greenhouse Gas Emissions". In: *Our World in Data*. URL: https://ourworldindata.org/co2-and-greenhouse-gas-emissions.

Saha, Priyanka et al. (2024). "Grey, blue, and green hydrogen: A comprehensive review of production methods and prospects for zero-emission energy". In: *International Journal of Green Energy* 21.6, pp. 1383–1397.

Sazali, Norazlianie (2020). "Emerging technologies by hydrogen: A review". In: *International Journal of Hydrogen Energy* 45.38, pp. 18753–18771.

Sciarretta, Antonio and Lino Guzzella (2007). "Control of hybrid electric vehicles". In: *IEEE control systems magazine* 27.2, pp. 60–70.

Sengers, J. V. and B. Kamgar-Parsi (1984). "Representative Equations for the Viscosity of Water Substance". In: *Journal of Physical and Chemical Reference Data* 13.1, pp. 185–205. DOI: 10.1063/1.555708.

Serrao, Lorenzo, Simona Onori, and Giorgio Rizzoni (2009). "ECMS as a realization of Pontryagin's minimum principle for HEV control". In: *2009 American Control Conference*, pp. 3964–3969. DOI: 10.1109/ACC.2009.5160628.

Sharaf, Omar Z and Mehmet F Orhan (2014). "An overview of fuel cell technology: Fundamentals and applications". In: *Renewable and sustainable energy reviews* 32, pp. 810–853.

Singh, Krishna Veer, Hari Om Bansal, and Dheerendra Singh (2019). "A comprehensive review on hybrid electric vehicles: architectures and components". In: *Journal of Modern Transportation* 27.2, pp. 77–107.

Singh, Prashant et al. (2025). "Rule-Based Energy and Thermal Management Strategy for Hybrid Fuel cell-Battery System Powered Heavy Duty Vehicle". In: *2025 IEEE Texas Power and Energy Conference (TPEC)*. IEEE, pp. 1–6.

Singla, Manish Kumar, Parag Nijhawan, and Amandeep Singh Oberoi (2021). "Hydrogen fuel and fuel cell technology for cleaner future: a review". In: *Environmental Science and Pollution Research* 28.13, pp. 15607–15626.

Sorlei, Ioan-Sorin et al. (2021). "Fuel cell electric vehicles—A brief review of current topologies and energy management strategies". In: *Energies* 14.1, p. 252.

Springer, T. E., T. A. Zawodzinski, and S. Gottesfeld (1991). "Polymer Electrolyte Fuel Cell Model". In: *Journal of The Electrochemical Society* 138.8, p. 2334. DOI: 10.1149/1.2085971.

Steelhead Composites (2023). *Composite Pressure Vessels*.

Strahl, Stephan et al. (2014). "Performance improvement by temperature control of an open-cathode PEM fuel cell system". In: *Fuel Cells* 14.3, pp. 466–478.

Upadhayay, Pranshu et al. (2018). "Evaluation of Energy Cost Index for an Electric Vehicle Motor Over a Particular Drive Cycle with Recycled Magnet

Concept". In: *2018 XIII International Conference on Electrical Machines (ICEM)*, pp. 738–744. DOI: 10.1109/ICELMACH.2018.8506906.

Valenzuela, Edgar et al. (2009). "Proton charge transport in nafion nanochannels". In: *Journal of Nano Research*. Vol. 5. Trans Tech Publ, pp. 31–36.

Van Dao, Dung et al. (2019). "Triple phase boundary and power density enhancement in PEMFCs of a Pt/C electrode with double catalyst layers". In: *RSC advances* 9.27, pp. 15635–15641.

Wang, Rui and Srdjan M Lukic (2012). "Dynamic programming technique in hybrid electric vehicle optimization". In: *2012 IEEE international electric vehicle conference*. IEEE, pp. 1–8.

Wang, Yeqin et al. (2018). "Research on energy optimization control strategy of the hybrid electric vehicle based on Pontryagin's minimum principle". In: *Computers & Electrical Engineering* 72, pp. 203–213.

Wee, Jung-Ho (2007). "Applications of proton exchange membrane fuel cell systems". In: *Renewable and sustainable energy reviews* 11.8, pp. 1720–1738.

Xun, Qian, Yujing Liu, and Elna Holmberg (2018). "A comparative study of fuel cell electric vehicles hybridization with battery or supercapacitor". In: *2018 International Symposium on Power Electronics, Electrical Drives, Automation and Motion (SPEEDAM)*. IEEE, pp. 389–394.

Zawodzinski, Thomas A. Jr. et al. (1991). "Determination of water diffusion coefficients in perfluorosulfonate ionomeric membranes". In: *The Journal of Physical Chemistry* 95.15, pp. 6040–6044. DOI: 10.1021/j100168a060.

Zgonnik, Viacheslav (2020). "The occurrence and geoscience of natural hydrogen: A comprehensive review". In: *Earth-Science Reviews* 203, p. 103140.

List of Acronyms

A-ECMS Adaptive Equivalent Consumption Minimisation Strategy. 21, 22, 117, 123, 124, 126, 127, 129–131

BoP Balance of Plant. 5, 92, 96

CL Catalyst Layer. 8, 11, 62, 67, 80, 91

DP Dynamic Programming. 18–20, 22

ECMS Equivalent Consumption Minimisation Strategy. 20, 21

ECU Electronic Control Unit. 16

EMG Electric Motor Generator. 97, 98, 101–103, 111

EMS Energy Management Strategy. 12, 17, 22, 115, 131, 132

EV Electric Vehicle. 110, 118

GDL Gas Diffusion Layer. 8, 11, 62

GFC Gas Flow Channel. 8, 62, 64, 91, 96

GHG Greenhouse Gas. XVII–XIX

HEV Hybrid Electric Vehicle. 15, 18, 116

KPI Key Performance Indicator. 92, 93

MAPE Mean Absolute Percentage Error. 88

MPL Micro-Porous Layer. 11

ODE Ordinary Differential Equation. 23, 38, 49, 58, 59

PDE Partial Differential Equation. 23, 24, 27, 28, 34, 36, 37, 41, 46, 48, 49, 56, 59, 131

PEI Powertrain Efficiency Index. 127, 128

PEM Polymer Electrolyte Membrane. 23, 75, 81, XXII

PEMFC Proton Exchange Membrane Fuel Cell. 6–8, 11–13, 15–17, 22, 61, 84, 85, 88, 96, 108–113, 115, 117–119, 121–124, 126–132, XVII, XXI–XXIII

PI Proportional Integral. 115–117

PI-RB Proportional Integral-Rule Based. 115, 123, 124, 126, 127

PMP Pontryagin's Minimum Principle. 19–21, 116, 117, 123, 124, 126–131

RB Rule Based. 115, 116, 118, 120, 124, 126, 128, 129

REx Range Extender. 110, 115, 116, 127, 131

RMSE Root Mean Square Error. 40, 47, 54, 87, 88

SoC State of Charge. 17–20, 22, 104–107, 109, 115–118, 120, 123, 127

TPB Triple Phase Boundary. 8

WMTC World Motorcycle Test Cycle. 97, 106, 118

List of Symbols

Greek Letters

α	Charge transfer coefficient	–
β	Swelling factor	–
δ	Membrane thickness fractional change	–
ε	Porosity	–
η	Efficiency	–
Γ	Water-dependant non-dimensional function	–
γ	Isentropic expansion coefficient	–
λ	Membrane water content	–
λ_{co}	Co-state variable	kg
$\dot{\lambda}_{co}$	Co-state variable rate	$\mathrm{kg \cdot s^{-1}}$
λ^{int}	Membrane water content intersection y-coordinate	–
μ	Dynamic viscosity	$\mathrm{Pa \cdot s}$
ω_m	Rotor speed	$\mathrm{rad \cdot s^{-1}}$
ϕ	Penalty function	kg
φ_{el}	Normalised stack power	–
ρ	Density	$\mathrm{kg \cdot m^{-3}}$
σ	Membrane Ohmic lineal conductivity	$\Omega^{-1}\mathrm{\cdot m^{-1}}$
τ_{cond}	Condensation time constant	s
τ_d	Non-dimensional characteristic time delay	–

τ_{evap}	Evaporation time constant	s
τ_n	Non-dimensional n-th characteristic time	–
υ_f	Normalised hydrogen consumption	–
ξ	Battery State-of-Charge	–
$\dot{\xi}$	Battery State-of-Charge rate	s^{-1}
ξ^{int}	Membrane water content intersection x-coordinate	–

Roman Letters

a_i	i-reactant activity	–
Q	Nominal capacity	$A \cdot s$
J_{cost}	Optimisation cost function	kg
A	CrosS-sectional area	m^2
I	Current	A
i	Current density	$A \cdot m^{-2}$
f^{Darken}	Darken factor	–
D	Diffusion coefficient	$m^2 \cdot s^{-1}$
D_a^{chem}	Water chemical diffusion coefficient	$m^2 \cdot s^{-1}$
C_d	Drag coefficient	–
V_{eff}	Effective available volume	m^3
V_{geom}	Geometrical volume	m^3
n_d	Electro-osmotic drag coefficient	–
$\dot{H}$	Enthalpy flow	W
M_{eq}	Equivalent vehicle mass	kg
s_0	Equivalence factor	kg
F	Force	N
R	Gas constant	$J \cdot kg^{-1} \cdot K^{-1}$
v_{gas}	Bulk gas velocity	$m \cdot s^{-1}$

$\bar{g}$	Molar Gibbs free energy	$\mathrm{J \cdot mol^{-1}}$
H	Hamiltonian cost function	$\mathrm{kg \cdot s^{-1}}$
HHV	Higher Heating Value	$\mathrm{J \cdot kg^{-1}}$
e	Indicated efficiency	–
k_n	Integration constant	–
k_i	Integral gain	$\mathrm{W \cdot s^{-1}}$
K_i	Integral gain	$\mathrm{kg \cdot s^{-1}}$
K_p	Proportional gain	kg
k_p	Proportional gain	W
L	Length	m
LHV	Lower Heating Value	$\mathrm{J \cdot kg^{-1}}$
m	Mass	kg
$\dot{m}$	Mass flow	$\mathrm{kg \cdot s^{-1}}$
y_a^i	Mass fraction of a specie in i volume	–
c	Molar concentration	$\mathrm{mol \cdot m^{-3}}$
J	Molar flux	$\mathrm{mol \cdot s^{-1} \cdot m^{-2}}$
x_a^i	Molar fraction of a specie in i volume	–
M	Molar mass	$\mathrm{kg \cdot mol^{-1}}$
N_{cells}	Number of cells included in a stack	–
a	Normalised water content	–
R_{int}	Internal Ohmic resistance	Ω
c_{over}	Overvoltage coefficient	V
Pe	Peclet number	–
k_w	Water permeability	$\mathrm{m^2}$
r_p	Mean pore radius	m
E	Theoretical electrical potential	V

P	Power	W
p	Pressure	Pa
p_a^i	Pressure of a specie in i volume	Pa
C_r	Rolling coefficient	–
X_n	Spatial eigenfunction	–
c_{stack}	Stack specific heat capacity	$J \cdot kg^{-1} \cdot K^{-1}$
c_p	Specific heat capacity at constant pressure	$J \cdot kg^{-1} \cdot K^{-1}$
r	Area specific Ohmic resistance	$\Omega \cdot m^2$
u	Characteristic speed	$m \cdot s^{-1}$
v	Vehicle speed	$m \cdot s^{-1}$
a_{Tafel}	Tafel slope	V
T_n	Temporal eigenfunction	–
T	Temperature	K
t	Time	s
t_d	Characteristic time delay	s
T_m	Torque	$N \cdot m$
A_f	Vehicle frontal area	m^2
C_x	Vehicle drag coefficient	–
$\dot{V}$	Volume flow	$m^3 \cdot s^{-1}$
V	Voltage	V
s	Water saturation	–

Subscripts

a/b	Generic a/b specie
act	Activation
$aero$	Aerodynamic
amb	Ambient

a	Anode
b	Battery
cap	Capillarity
c	Cathode
CL	Catalyst Layer
$conc$	Concentration
$cond$	Condensation
$conv$	Convection
DC	DC
$diff$	Diffusion
eff	Effective
el	Electric
end	Ending
EOD	Electro-Osmotic Drag
$evap$	Evaporation
f	Fuel
fix	Fixed
FC	Fuel cell
gas	Gas
GDL	Gas Diffusion Layer
H_2	Hydrogen
in	Inlet
in	Inertia
int	Internal
lim	Limiting
liq	Liquid

$load$	Load
$loss$	Losses
m	Motor
mem	Membrane
$Nernst$	Nernst
N_2	Nitrogen
OC	Open Circuit
off	Offset
Ohm	Ohmic
out	Outlet
O_2	Oxygen
Pt	Platinum
red	Reduced
REx	Range Extender
$roll$	Rolling
sat	Saturation
$stack$	Stack
s	Steady-state
$tank$	Tank
T	Thermal/Temperature
u	Unsteady
vap	Vapour
H_2O	Water
w	Water
0	Reference/Initial

Superscripts

An	Anode
$*$	Fixed/Approximation
avg	Average
Ca	Cathode
chg	Charge
CL	Catalyst Layer
dis	Discharge
DM	Discharge Manifold
dry	Dry
$Fick$	Fick's law
$GDL(a)$	Gas Diffusion Layer, portion (a)
$GDL(b)$	Gas Diffusion Layer, portion (b)
$GDL(c)$	Gas Diffusion Layer, portion (c)
GFC	Gas Flow Channel
i/j	Generic i/j volume
lim	Limiting
$l \rightarrow s$	From load to source
mem	Membrane
rat	Rated
req	Request
$s \rightarrow l$	From source to load
SM	Supply Manifold
st	Stoichiometric

Acknowledgements

The research presented in this dissertation is part of the project HySuM (Hybrid Sustainable Mobility Platform), funded by the Italian Ministry of University and Research under the call PRIN 2020. The Doctoral fellowship of Massimo Sicilia is funded by the project HySuM-PRIN 2020.